

**Boston University**

**OpenBU**

**<http://open.bu.edu>**

---

Theses & Dissertations

Boston University Theses & Dissertations

---

2020

# Transillumination techniques in ophthalmic imaging

---

<https://hdl.handle.net/2144/41025>

*Boston University*

BOSTON UNIVERSITY  
COLLEGE OF ENGINEERING

Dissertation

**TRANSILLUMINATION TECHNIQUES IN OPHTHALMIC  
IMAGING**

by

**TIMOTHY D. WEBER**

B.S., Columbia University, 2014

M.S., Boston University, 2017

Submitted in partial fulfillment of the  
requirements for the degree of  
Doctor of Philosophy

2020

© 2020 by  
TIMOTHY D. WEBER  
All rights reserved

Approved by

First Reader

---

Jerome Mertz, Ph.D.  
Professor of Biomedical Engineering  
Professor of Electrical Engineering  
Professor of Physics

Second Reader

---

David A. Boas, Ph.D.  
Professor of Biomedical Engineering  
Professor of Electrical and Computer Engineering

Third Reader

---

Thomas G. Bifano, Ph.D.  
Professor of Mechanical Engineering  
Professor of Materials Science and Engineering  
Professor of Biomedical Engineering

Fourth Reader

---

Ji Yi, Ph.D.  
Assistant Professor of Medicine  
Assistant Professor of Biomedical Engineering

Fifth Reader

---

Charles P. Lin, Ph.D.  
Associate Professor of Dermatology  
Harvard Medical School

## Acknowledgments

I am indebted to several people who have, in one way or another, contributed to the successful completion of this thesis.

Years ago during my undergraduate studies, I was fortunate enough to be introduced to optical microscopy research by Elizabeth Hillman and Matthew Bouchard, two of the most inventive and talented minds in the field. I credit them with unleashing my idea as to what a microscope could be. Another early research mentor that I wish to thank is Gregory Faris. In my mind, Greg is the epitome of genuine scientific curiosity and is one of the most generous mentors I have ever encountered.

At BU, several members of my graduate cohort should be singled out for their exceptional companionship. R.J. Seager, Andrew Acevedo, Dustin Clark, and Raeeef Istfan have no doubt made my time here more satisfying.

While much of the work in this thesis was done independently (ophthalmic imaging is a new area for the lab), I am grateful for the support of various lab members. In particular, I wish to thank my longtime office mate, Amaury Badon for sharing with me his optical expertise and the occasional French cultural tip.

I must also thank my thesis advisor, Jerome Mertz for granting me unusually broad autonomy to pursue ophthalmic imaging projects. I am grateful to have had the opportunity to closely observe his emulable teaching style and I hope, by proximity, to have absorbed some of his legendary understanding of microscopy.

And finally, I would like to acknowledge my biggest supporter, Emma Yee, whose blood and tears quite literally went into this thesis (retinal blood vessels and tear film, that is). Her steadfast confidence in me is my foundation.

# TRANSILLUMINATION TECHNIQUES IN OPHTHALMIC IMAGING

TIMOTHY D. WEBER

Boston University, College of Engineering, 2020

Major Professor: Jerome Mertz, Ph.D.

Professor of Biomedical Engineering

Professor of Electrical Engineering

Professor of Physics

## ABSTRACT

*In vivo* imaging of the human cornea and retina is typically performed in a reflection geometry. Images are formed from light that has backscattered off corneal microstructures or backreflected from the retina. In this configuration, artifacts caused by superficial surface reflections are often encountered. These unwanted reflections can either globally overwhelm the signal or cause local glare, complicating reliable image quantification. This thesis describes a pair of alternative ophthalmic imaging techniques based instead on transmitted light, which inherently avoids these artifacts.

For retinal (i.e. fundus) imaging, we describe a mesoscopic transmission imaging method, which we call transcranial fundus imaging. The method uses deeply penetrating near-infrared light delivered transcranially from the side of the head, and exploits multiple scattering to redirect a portion of the light towards the posterior eye. This unique transmission geometry simplifies absorption measurements and enables flash-free, non-mydratic imaging as deep as the choroid. We use multispectral image sets taken with this new transillumination approach to estimate oxygen saturation in retinal blood vessels.

In the cornea, we describe a new technique for non-contact phase-contrast microscopic imaging. It is based on fundus retro-reflection and back-illumination of the crystalline lens and cornea. To enhance phase-gradient contrast, we apply asymmetric illumination by illuminating one side of the fundus. The technique produces micron-scale lateral resolution across a 1-mm diagonal field of view. We show representative images of the epithelium, the subbasal nerve plexus, large stromal nerves, dendritic immune cells, endothelial nuclei, and the anterior crystalline lens, demonstrating the potential of this instrument for clinical applications.

# Contents

<b>1</b>	<b>Introduction</b>	<b>1</b>
1.1	Why transmission imaging? . . . . .	1
1.2	Engineering design and physiology of the retina . . . . .	2
1.3	Corneal anatomy . . . . .	7
<b>2</b>	<b>Transcranial Fundus Imaging</b>	<b>10</b>
2.1	Introduction . . . . .	10
2.1.1	Existing fundus imaging methods . . . . .	11
2.1.2	Fundus endogenous contrast and spectroscopy . . . . .	12
2.1.3	Imaging spectroscopy artifacts . . . . .	13
2.1.4	Transmission imaging in thick tissue . . . . .	14
2.2	Transcranial illumination fundus imaging system . . . . .	19
2.2.1	Transcranial illumination . . . . .	20
2.2.2	Fundus camera and CCD sensor detection subsystem . . . . .	22
2.2.3	Custom GUI and LED toggle . . . . .	24
2.2.4	Transcranial retinal exposure and spectral transmission . . . . .	24
2.3	Subjects and imaging sessions . . . . .	25
2.4	Image processing . . . . .	26
2.4.1	Image registration and averaging . . . . .	27
2.4.2	Relative absorbance calculation . . . . .	28
2.5	Results . . . . .	29
2.5.1	Multispectral imaging and chromophore unmixing . . . . .	32



2.5.2	Retinal oximetry . . . . .	35
2.6	Discussion . . . . .	37
2.6.1	Retinal vessel oximetry . . . . .	37
2.6.2	Potential sources of error . . . . .	39
2.6.3	Comparison with reflection imaging . . . . .	41
2.6.4	Potential improvements . . . . .	42
2.6.5	Future applications . . . . .	43
2.7	Conclusion . . . . .	43
<b>3</b>	<b>Comparison of Transcranial and Reflection Fundus Imaging</b>	<b>45</b>
3.1	Background . . . . .	45
3.2	Methods . . . . .	47
3.2.1	Fundus camera modifications . . . . .	47
3.2.2	Vessel fitting . . . . .	48
3.3	Results . . . . .	48
3.3.1	Simultaneous transmission and reflection fundus imaging . . . . .	48
3.3.2	Vessel fitting . . . . .	50
3.4	Discussion . . . . .	52
<b>4</b>	<b>Retroillumination Microscopy</b>	<b>53</b>
4.1	Introduction . . . . .	53
4.1.1	Significance . . . . .	53
4.1.2	Evolution of existing clinical methods . . . . .	54
4.1.3	OCT-based corneal microscopy . . . . .	60
4.1.4	Fundus retroillumination . . . . .	61
4.2	Device description . . . . .	62
4.2.1	Hardware . . . . .	62
4.2.2	Resolution and field of view . . . . .	67

4.2.3	Light levels and safety . . . . .	68
4.3	Image processing . . . . .	68
4.4	Example images . . . . .	69
4.4.1	Subjects . . . . .	69
4.4.2	Epithelium . . . . .	70
4.4.3	Stroma . . . . .	73
4.4.4	Endothelium . . . . .	74
4.4.5	Crystalline lens . . . . .	74
4.5	Subbasal nerve plexus density . . . . .	76
4.6	Endothelium through-focus . . . . .	77
4.7	Discussion . . . . .	78
4.7.1	Transmission vs. reflection imaging . . . . .	78
4.7.2	Comparison to slit lamp technique . . . . .	79
4.7.3	Single versus dual image . . . . .	80
4.7.4	Limitations . . . . .	80
4.7.5	Corneal subbasal nerve density . . . . .	81
4.7.6	Defocused contrast . . . . .	84
4.7.7	Future applications . . . . .	85
<b>A Three-dimensional Image Formation Model for Retroillumination</b>		
	<b>Microscopy</b>	<b>86</b>
A.1	Introduction . . . . .	86
A.2	Propagation of partially coherent light . . . . .	86
A.3	Propagation of 3D intensity . . . . .	89
A.4	Born approximation . . . . .	91
A.5	3D image formation . . . . .	92
A.6	Evaluation of the 3D OTF and PSF . . . . .	96

<b>B</b>	<b>Code for three-dimensional image formation model</b>	<b>101</b>
B.1	Outline . . . . .	101
B.2	Code . . . . .	101
B.2.1	Utilities . . . . .	104
	<b>References</b>	<b>110</b>
	<b>Curriculum Vitae</b>	<b>125</b>

# List of Tables

2.1	LED choices, associated ANSI maximum permissible exposures (MPEs) for skin and retina, and measured or estimated irradiance. . . . .	23
2.2	Quantified retinal oximetry results in regional quadrants and across the whole fundus shown in Figure 2-14. . . . .	37
4.1	Recent studies reporting central cornea subbasal nerve density in healthy populations. . . . .	82

# List of Figures

1·1	Reflection (left) and transmission (right) are sensitive to different spatial frequencies ( $k_x$ and $k_z$ ) of sample refractive index, $n$ . . . . .	3
1·2	Eye and retinal anatomy. . . . .	4
1·3	Detailed schematic of the retina near the central field of view, an area called the fovea. . . . .	6
1·4	Illustration showing the cornea and cross section diagram of the main cell layers. . . . .	8
1·5	Depiction of corneal nerves innervating the anterior cornea. . . . .	9
2·1	Light paths for fundus imaging in reflection (left), and transmission (right) illumination geometries overlayed on a histological section. . .	13
2·2	Strong reflection from center of retinal blood vessel and evidence of nerve fiber bundle specular reflection artifact. . . . .	15
2·3	Spectral-domain OCT (SD-OCT) cross-sectional (B-mode) scan through a healthy retina. . . . .	16
2·4	Concept of oblique back-illumination microscopy (OBM). . . . .	17
2·5	Density map from a Monte Carlo simulation of diffuse light transport. . . . .	18
2·6	Proposed transcranial back-illumination technique shown with human head transverse section through orbits. . . . .	20
2·7	Simplified schematic for fundus transcranial illumination and imaging with sample image and illumination spectra. . . . .	21

2·8	3D CAD rendering of a custom 4-channel (left) or 6-channel (right) LED-to-fiber bundle combiner. . . . .	22
2·9	Registration and averaging improve SNR for intrinsically low contrast NIR retinal vasculature imaging. . . . .	28
2·10	Demonstration of local maximum filtering and relative absorbance images from left eye of a healthy 59-year-old subject. . . . .	30
2·11	Transcranial back-illumination proof of concept test. . . . .	31
2·12	Relative absorbance images for several indicated NIR wavelengths in the retina near the optic disc. . . . .	33
2·13	Linear spectral absorbance unmixing of contributions from dominant chromophores in the fundus. . . . .	35
2·14	Chromophore background correction and widefield retinal oximetry map in fundus of the left eye of a normal volunteer. . . . .	38
3·1	Hypothetical light paths for transmission and reflection imaging in the vicinity of a vessel (oriented perpendicular to the page). . . . .	46
3·2	Quasi-simultaneous transmission and reflection fundus imaging results at 850 nm. . . . .	49
3·3	Quasi-simultaneous transmission and reflection imaging of retinal vessels.	50
3·4	Fitting the 2D model of a retinal vessel to straightened segments extracted from image data. . . . .	51
3·5	Vessel model fitting results across extended lengths of retinal vessels.	51
4·1	Specular microscopy concept and sample images. . . . .	55
4·2	Koester's scanning mirror microscope. . . . .	57
4·3	IVCM diagram and sample images. . . . .	59
4·4	Asymmetric fundus retroillumination concept. . . . .	62
4·5	Retroillumination prototype system optical diagram. . . . .	63

4·6	Illumination in cross-section at the pupil/cornea (left) and at the fundus (right). . . . .	64
4·7	Photograph of the actual prototype retroillumination microscope and location of planes conjugate to planes depicted in Figure 4·6. . . . .	65
4·8	SNR enhancement after frame averaging at the endothelial cell layer, one of the lowest contrast layers examined. . . . .	69
4·9	Subbasal nerve plexus of a 28-year-old male near the corneal apex visualized with retroillumination microscopy. . . . .	71
4·10	Other periepithelial structures visualized with retroillumination microscopy. . . . .	72
4·11	Large stromal nerves in a 28-year-old male. . . . .	73
4·12	Wide field of view of the endothelium in a 26-year-old female. . . . .	75
4·13	Cropped view of endothelium near the corneal apex of a 26-year old female. . . . .	75
4·14	Crystalline lens (A) epithelium and (B) anterior fibers just below the epithelium. . . . .	76
4·15	Results of semi-automated nerve tracing on widefield SBP image shown in Figure 4·9. . . . .	77
4·16	Inversion of contrast in endothelium seen in video corresponding to Figure 4·12. . . . .	78
4·17	Subbasal nerve plexus contrast varies considerable depending on the acquisition method. . . . .	83
A·1	Phase OTFs for symmetric and asymmetric illumination configurations with varying coherence $\gamma$ . . . . .	98
A·2	Phase PSF axial sweep for both symmetric and asymmetric illumination configurations at various levels of coherence. . . . .	99

A.3	Simulation of imaging a single endothelial cell nucleus with asymmetric illumination and varying degrees of coherence, $\gamma$ . . . . .	100
-----	---	-----



## List of Abbreviations

A-V	.....	Arteriovenous
AI	.....	Artificial intelligence
AMD	.....	Age-related macular degeneration
AOSLO	.....	Adaptive optics scanning laser ophthalmoscopy
BM	.....	Brunch's membrane
CCD	.....	Charge-coupled device
CMOS	.....	Complementary metal-oxide-semiconductor
CO	.....	Coupling optics
cSLO	.....	Confocal scanning laser ophthalmoscopy
BEP	.....	Basal epithelial (nerve) plexus
DIC	.....	Differential interference contrast
DR	.....	Diabetic retinopathy
FB	.....	Fiber bundle
FC	.....	Fundus camera
FF-OCT	.....	Full-field time-domain optical coherence tomography
fNIRS	.....	Functional near-infrared spectroscopy
FOV	.....	Field of view
FWHM	.....	Full width at half maximum
GUI	.....	Graphical user interface
Hb	.....	Deoxyhemoglobin
HbO <sub>2</sub>	.....	Oxyhemoglobin
HRT	.....	Heidelberg retinal tomographer
ILM	.....	Inner limiting membrane
IPL	.....	Inner plexiform layer
IVCM	.....	<i>In vivo</i> confocal microscopy
LED	.....	Light-emitting diode
LSCM	.....	Laser scanning confocal microscopy
mfp	.....	Mean free path
ML	.....	Machine learning
MPE	.....	Maximum permissible exposure
<i>n</i>	.....	Refractive index

NA	.....	Numerical aperture
NFL	.....	Nerve fiber layer
NIR	.....	Near-infrared
OBM	.....	Oblique back-illumination microscopy
OCT	.....	Optical coherence tomography
OCTA	.....	Optical coherence tomography angiography
OPL	.....	Outer plexiform layer
OTF	.....	Optical transfer function
PBS	.....	Polarizing beam splitter
PCB	.....	Printed circuit board
PRL	.....	Photoreceptor layer
PRNU	.....	Photo response non-uniformity
PSF	.....	Point spread function
QE	.....	Quantum efficiency
RCM	.....	Rostock cornea module
RIM	.....	Retroillumination microscopy
rms	.....	Root mean square
RPE	.....	Retinal pigment epithelium
SBP	.....	Subbasal (nerve) plexus
SD	.....	Standard deviation
SEP	.....	Subepithelial (nerve) plexus
SLO	.....	Scanning laser ophthalmoscopy
SM	.....	Specular microscopy
SNR	.....	Signal-to-noise ratio
SO <sub>2</sub>	.....	Percent oxygen saturation
SSCM	.....	Slit scanning confocal microscopy
TSCM	.....	Tandem scanning confocal microscopy
vis-OCT	.....	Visible light optical coherence tomography

## Chapter 1

# Introduction

### 1.1 Why transmission imaging?

Ophthalmic imaging is typically performed in a reflection geometry. Light is directed towards the tissue of interest (cornea, retina, etc.) and backscattered light is collected to form an image. If the tissue of interest happens to be the fundus (the back inner surface of the eye, which includes the retina) the optics of the eye are additionally involved in the imaging process. For many applications, this configuration provides suitable contrast—so then why would one consider transmission imaging? The answer will depend on the imaging length scale and tissue of interest.

Fundus imaging is typically performed over a large field of view, on the scale of a centimeter. Because the sub-optimal optical quality of the eye limits the maximum useful numerical aperture (NA) (Artal, 2014), resolution is modest (about 10-20  $\mu\text{m}$ ). We call this the mesoscopic imaging scale because it is between typical microscopy and macroscopic imaging (i.e. photography). At this scale, reflection imaging is susceptible to artifacts caused by superficial surface reflections. These are caused by abrupt changes in refractive index at the interface of different retinal layers or by blood vessel walls. The unwanted reflections can either globally overwhelm the signal or cause local glare, complicating reliable image quantification. Transmission imaging would hypothetically avoid such spurious reflections because it is a single-pass technique. In Chapter 2, we introduce transcranial fundus imaging, a novel transmission imaging technique for fundus imaging.

Corneal imaging may also be performed at the mesoscopic scale. The common instrument for this purpose is the slit lamp biomicroscope. However, access to the cornea is not so limited, and a high-NA microscope objective can be used to obtain micron-scale images. In this case, superficial reflections may occur, for instance at the air-cornea interface, however techniques such as confocal microscopy and optical coherence tomography (OCT) have been developed to reject such reflections (see Section 4.1.2 for a discussion). Transmission imaging would presumably also avoid this reflection.

There is also a more subtle reason to use transmission microscopy, related to the obtainable image contrast. As depicted in Figure 1-1, in order to generate any backscattered signal, the sample must present an abrupt difference in refractive index along the direction of the incident light. However, there is no such restriction for transmission, which collects only forward-scattered. Equivalently, in terms of refractive index spatial frequencies  $(k_x, k_z)$ , reflection imaging supports only those spatial frequencies with a large axial offset. Transmission imaging supports spatial frequencies closer to the origin. Hence, transmission imaging opens up an entirely new unexplored region of the spatial frequency domain which may provide enhanced contrast of certain cellular features. In Chapter 4 we introduce a new technique, which we term retroillumination microscopy (RIM). The new technique permits high-resolution transmission microscopic imaging of the human cornea.

## 1.2 Engineering design and physiology of the retina

From an engineering perspective, the eye is a technical marvel: it is the highest dynamic range light sensor ever made and runs on just a tiny fraction of the power required to run the world's most efficient cameras. To help motivate and inform the discussion of ocular diseases and imaging challenges, the eye's technical design will

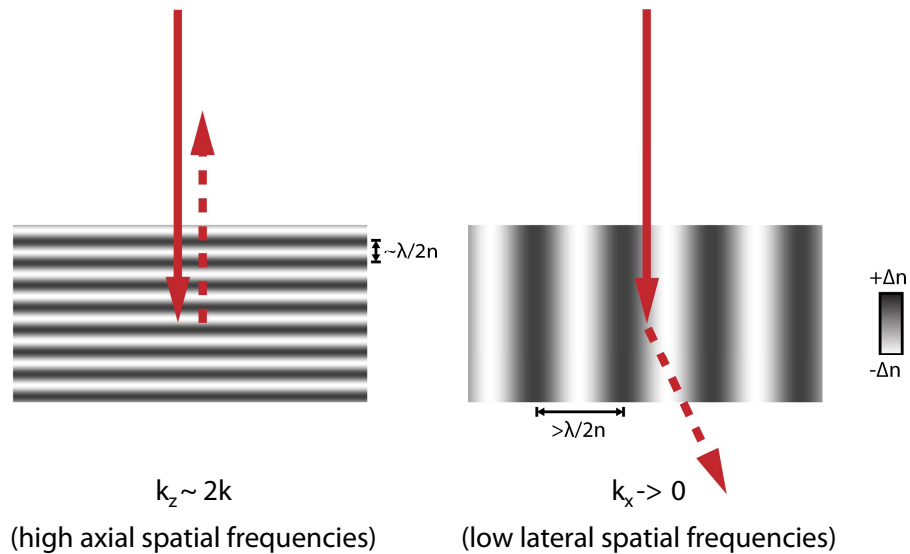


**Figure 1.1:** Reflection (left) and transmission (right) are sensitive to different spatial frequencies ( $k_x$  and  $k_z$ ) of sample refractive index,  $n$ . The wavenumber is  $k$  is the inverse of wavelength times the average refractive index.

be quickly reviewed.

Optical elements at the entrance to the eye (cornea, iris, and lens in Fig. 1.2, left) transform the incident light field and project an image representing the surrounds onto the back of the inner eye. A specialized organ, called the retina, converts optical intensities in this image into electrical signals and these signals are relayed to the brain (Hecht, 2001).

In the human retina, about 130 million photosensitive cells called photoreceptors (rods and cones in Fig. 1.2, right), spatially sample the two-dimensional optical intensity distribution of the retinal image (Osterberg, 1935). Photoreceptors are routinely sensitive to light intensities over eight orders of magnitude. However, large intensity changes require adaptation, a relatively slow process by which the effective gain of the cell is adjusted according to the average detected light power (Tessier-Lavigne, 2000). The actual instantaneous dynamic range of a single photoreceptor is consid-

erably less, only about 10 distinguishable levels (3.3 bits), limited by the quantal release of synaptic vesicles (Choi et al., 2005). Nevertheless, considering the average photoreceptor's response rate of 14 Hz (Tessier-Lavigne, 2000), the retina's raw data rate is an astonishing 750 MB/s!

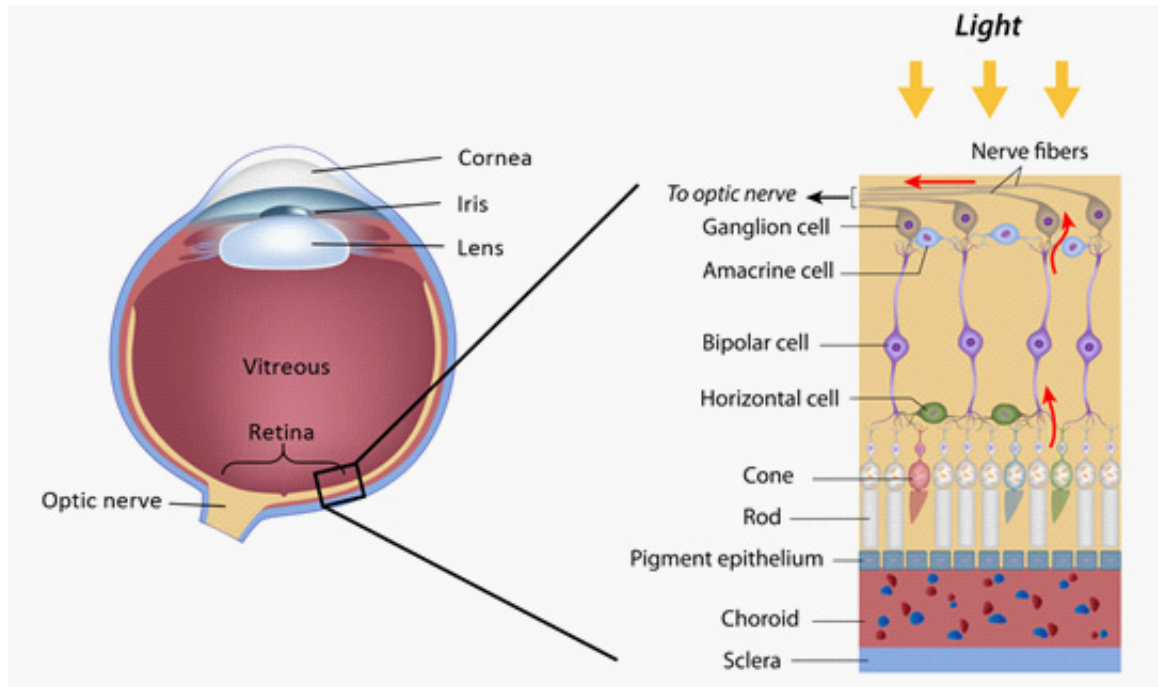


**Figure 1.2:** Eye and retinal anatomy. Left: cross section of the eye showing the imaging elements: the cornea, iris, and lens, and the location of the retina and optic nerve. Right: cartoon schematic of showing the major retinal cell types along with the pigmented epithelium and choroid, which are necessary to maintain sustained metabolism in the photoreceptors (rods and cones).

Fortunately, the brain does not need to process this entire deluge of raw information. Bipolar cells (Fig. 1.2, right) consolidate signals from multiple photoreceptors. Horizontal and amacrine cells help extract features of interest (i.e. edges, sudden movements, etc.). Ganglia cells collect the processed signals and send the information down axons into the optic nerve. It is estimated that the human optic nerve transfers about 1 MB/s (Koch et al., 2006). Thus, the retina's circuitry has com-

pressed the raw signal 750-fold.

The remarkable amount of data acquisition and compression performed in the retina would not be possible without external energy coupling. Light detection and amplification is an active process. In particular, the photosensitive “outer” segments of the photoreceptors (adjacent the pigmented epithelium) are extremely metabolically active (Buttery et al., 1991). Their activity is due to the concentration gradients and ion pumps that must be maintained in order amplify weak detected signals, along with their rapid turnover—the functional contents are completely regenerated about once per week (Tessier-Lavigne, 2000). It is unsurprising then, that by mass, the retina is the most energetically demanding tissue in the entire body (Saari, 1987).

To meet such a demand, while minimizing potential image degradation, evolution has designed the retina in an “inside-out” fashion with essentially two separate vascular systems, a configuration that has bewildered scientists and students for ages (Tessier-Lavigne, 2000). As shown in Figure 1·2 and 1·3, the photoreceptor layer is tucked underneath other cells of the retina. Light must traverse several cell layers before it may be detected. This turns out to be less of a penalty as one might expect, since these cell layers are relatively transparent. Also, the space above the fovea, the area of the retina responsible for high-acuity central vision, is mostly devoid of these other non-photosensitive cells. The cells responsible for transmitting signals from fovea photoreceptors are shifted towards the periphery

The advantage to this configuration is that a very dense vascular network, being necessary to support high metabolic activity, may be located without interruption, in close proximity to the photoreceptor layer (choroid and choriocapillaris in Fig. 1·3) (Linsenmeier and Padnick-Silver, 2000). Because the vasculature contains hemoglobin, which strongly absorbs visible light, it could not be located between the incident light and the photoreceptors without severely reducing detection efficiency,

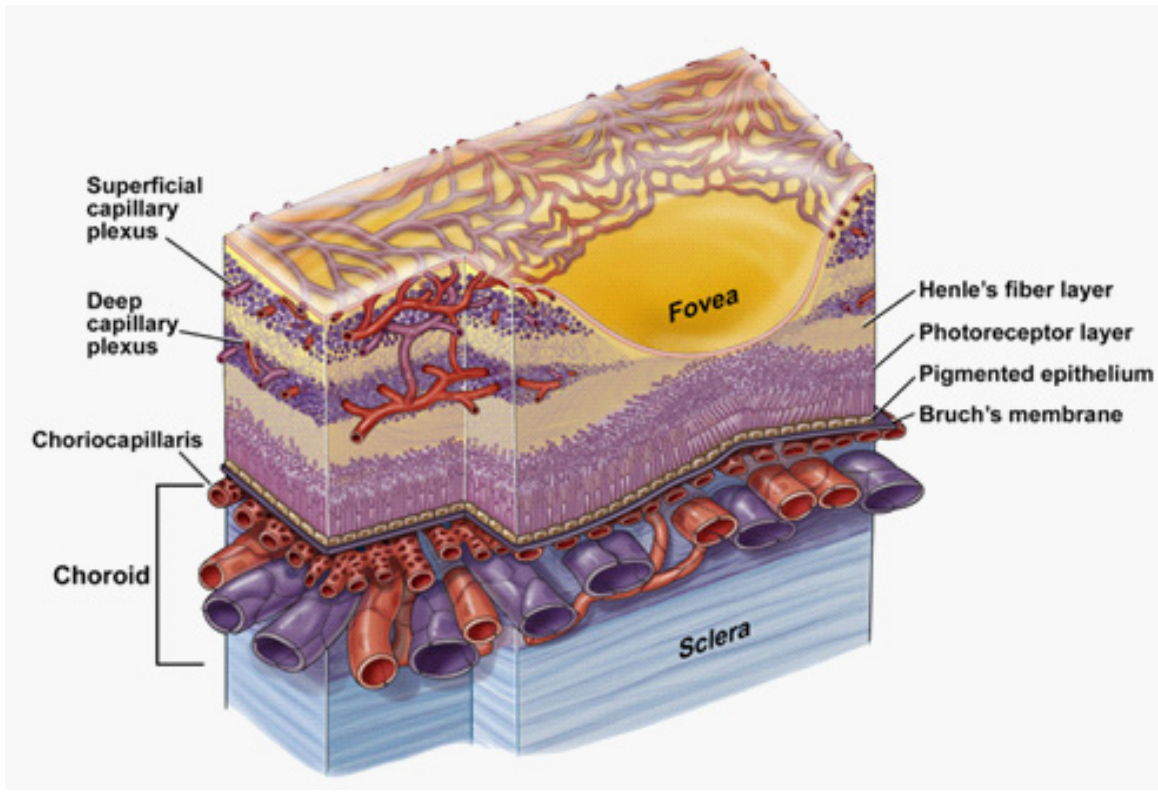


**Figure 1-3:** Detailed schematic of the retina near the central field of view, an area called the fovea. Note the thickness and density of the choroidal vessels, which supply oxygen and nutrients to the photoreceptors, relative to the superficial and deep capillary plexus vessels, which service other retina cells. Reproduced from (Anand-Apte and Hollyfield, 2010).

nor could it be located within the photoreceptor layer without comprising spatial resolution and/or detection fill factor. Another complimentary vascular system runs over the top of the retina (superficial and deep capillary plexus in Fig. 1-3). The metabolic demand for this system is relatively less and a much more sparse network is evidently adequate. The sub-photoreceptor vasculature system is known as the choroid, while the system above the photoreceptors is simply called the retinal vasculature. Despite the name, the choroid accounts for the majority of ocular blood flow (Cioffi et al., 1987), consistent with metabolic observations.



### 1.3 Corneal anatomy

The cornea is the outermost part of the eye—a window between the neurosensory retina and the outside world. It has dual roles: 1. maintenance of optical transparency for clear vision, and 2. mechanical strength for consistent refraction and protection (Dawson et al., 2011). These roles are sometime at odds in other tissues of the body, bone for instance. The cornea is also in contact with the outside world, thus the cornea has a very important immunological roles.

A diagram of the cornea with its various layers is shown in Figure 1.4. The endothelium is the most posterior (bottom) layer of the cornea. It is a cellular monolayer responsible for pumping water out of the cornea in order to maintain a precise corneal osmolality. This is very important for optical transparency: disrupted pumping can lead to corneal edema and vision impairment (Bourne, 2003). Because the cornea is avascular, the endothelium must also facilitate transfer of nutrients from its underlying aqueous humor to the stromal volume of the cornea.

The stroma makes up the bulk of the cornea and its purpose is mainly to promote mechanical integrity. Keratocytes are the primary cell type of the stroma. They are fibrous and stacked very thinly along the axial extent of the cornea.

Finally the epithelium makes up the last cell layer of the cornea. It is about 4-6 cells deep. The posterior cell layer is called the basal epithelium, the middle are called wing cells, and the anterior-most layer is called superficial epithelium. The corneal epithelium, like the skin epithelium, is constantly turning over and shedding. It has the highest proliferative capacity among cells in the cornea, which in rare cases can lead to cancer (Dawson et al., 2011). The endothelium, has the lowest regenerative capability, while the stroma has a limited ability.

Although the cornea is mostly avascular, it is highly innervated. In terms of nerve terminal density it is the most innervated tissue in the body. Many of the nerve

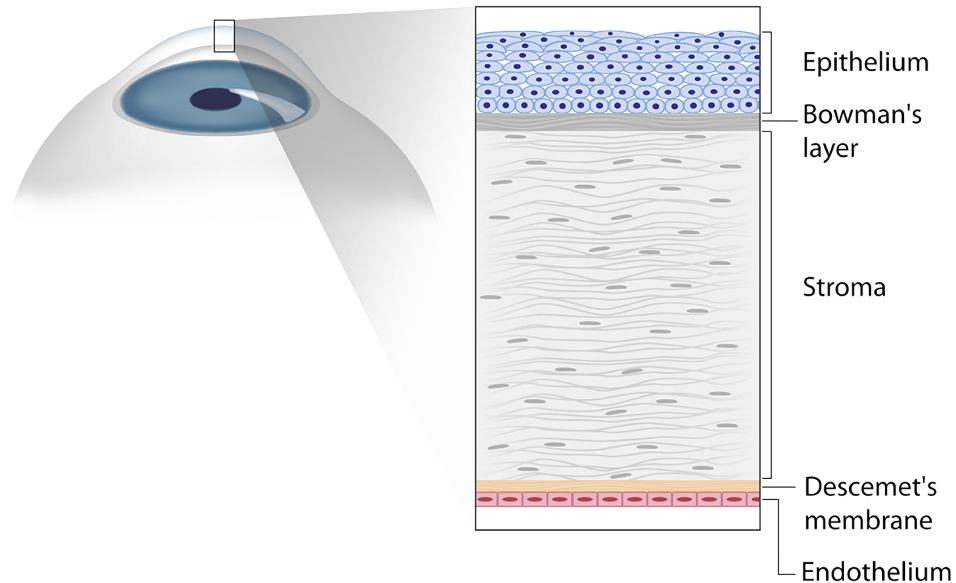


**Figure 1-4:** Illustration showing the cornea and cross section diagram of the main cell layers

terminals sense dryness and hence are crucial for tear film maintenance. They are also thought to help regulate immune response and epithelial cell proliferation by secretion of neurotrophins (Oliveira-Soto and Efron, 2001).

Corneal nerves originate from the trigeminal nerve (not the optic nerve) and enter the cornea radially from the periphery in the stroma. These stromal nerves are bundles of hundreds to thousands of axons. From the periphery, the bundles course towards the center bifurcating repeatedly to form the supepithelial plexus (SEP, shown in Fig. 1-5). Some branches of the SEP penetrate the Bowman's membrane and enter the epithelium where they branch further into the dense subbasal nerve plexus (SBP), also known as the simply the basal epithelial plexus (BEP). From the SBP, intraepithelial branches turn and rise towards the superficial epithelium where they terminate.

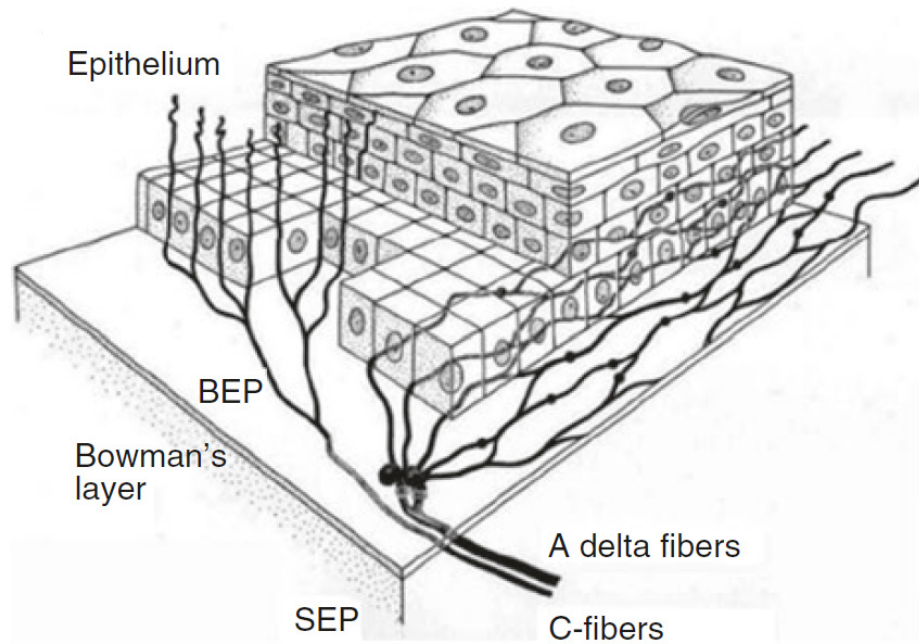


**Figure 1-5:** Depiction of corneal nerves innervating the anterior cornea. Reproduced from (Guthoff et al., 2005)

## Chapter 2

# Transcranial Fundus Imaging

### 2.1 Introduction

Ocular disease detection is challenging because many diseases do not present symptoms until irreversible damage has occurred (Levin and Albert, 2010). This is particularly true for disease of the posterior eye (i.e. the fundus). Typically, fundus screening involves direct retinal examination by an experienced ophthalmologist, and/or documentation with fundus photography (Jain et al., 2006). The latter has the advantages that it may be used repeatedly to track fundus appearance over time and may exploit digital contrast enhancement (Abràmoff et al., 2010). Fundus images may also be used in remote “tele-screening” programs, which have great potential to expand screening access, while improving clinic throughput (Li, 1999). In particular, when combined with machine learning (ML) or artificial intelligence approaches (AI), tele-screening has enormous potential for early disease diagnostics (Poplin et al., 2018; Ting et al., 2019).

A wealth of information is contained in the optical appearance of the posterior human eye, which includes the retina, macula, and fundus. Recently, the term *oculomics* has been used to describe the collection of possible ocular and systemic disease biomarkers present in high-quality retinal images (Wagner et al., 2020). The retina possesses a tightly regulated blood supply similar to that of the brain (Pournaras et al., 2008). Misregulation or damage to retinal circulation has been implicated in ocular diseases such as age-related macular degeneration (AMD) and systemic diseases

such diabetes and cardiovascular disease (Abràmoff et al., 2010). Recent work has suggested that possible biomarkers for neurodegenerative conditions, like Alzheimer’s disease, may also exist in the retinal vasculature (Olafsdottir et al., 2018; Lim et al., 2016). Thus, there is strong need for high-throughput, noninvasive methods to monitor retinal circulation.

### 2.1.1 Existing fundus imaging methods

Fundus imaging methods (i.e. fundoscopy or more commonly known as ophthalmoscopy) can be divided into widefield and scanning-based techniques. Scanning techniques raster a focused laser beam across the fundus while recording back-reflected light, and images are synthesized point-by-point in a technique known as scanning laser ophthalmoscopy (SLO) (Webb et al., 1980; Webb and Hughes, 1981). The use of confocal detection in confocal SLO (cSLO) (Webb et al., 1987) or coherence gating in optical coherence tomography (OCT) (Huang et al., 1991; Fercher, 1996) enables three-dimensional (3D) sectioning and very high contrast by rejecting multiple scattered light that otherwise contributes to background. Indeed, variations on scanning techniques, such as OCT angiography (OCTA) (de Carlo et al., 2015; Kashani et al., 2017) and adaptive optics scanning ophthalmoscopy (AOSLO) (Liang et al., 1997; Roorda et al., 2002), have produced detailed views of retinal capillary networks in vivo (Chui et al., 2012).

In contrast, ophthalmoscopy, a widefield technique, illuminates large areas of the fundus and records real images on film or digital sensor of the retina from light reflected back through the pupil. In the clinic, this is routinely performed with a fundus camera (FC) and depending on the wavelength choice (Delori et al., 1977), generally provides adequate contrast of large structures, such as the vasculature, optic disc, nerve fiber bundle, and macula. A significant disadvantage of widefield techniques is that they do not provide depth discrimination. Nevertheless, owing

to their simplicity and ubiquity in clinical practice, widefield techniques are more suitable for high-throughput disease screening.

### **2.1.2 Fundus endogenous contrast and spectroscopy**

Although exogenous vessel contrast agents, such as fluorescein (Novotny and Alvis, 1961), have been used for decades, in principle the natural spectral differences between endogenous absorbers should reveal the relative distributions of chromophores in the eye (Berendschot et al., 2003). Specifically, the quantification of oxygen saturation in retinal vessels is known as retinal vessel oximetry (Harris et al., 2003; MacKenzie and Harvey, 2018). It has repeatedly been shown that in major ocular diseases, retinal vessel oxygen saturation abnormalities precede clinically detectable morphological changes (Linsenmeier and Zhang, 2017).

The challenge with all spectroscopic techniques in the eye is that multiple reflection paths from stratified fundus layers contribute to the observed reflectance image (Smith et al., 2000) and that the relative contribution from each of these reflections is highly sensitive to the degree of fundus pigmentation (Delori and Pflibsen, 1989; Smith et al., 2001). Figure 2.1 depicts typical light paths in a reflection and a hypothetical transmission geometry. Models for the interpretation of the reflected light have characterized the return of light according to wavelength (Van Norren and Tiemeijer, 1986; Delori and Pflibsen, 1989; Schweitzer et al., 1999), refractive index differences between retinal layers (Hammer et al., 2001), and even image system modulation transfer efficiency (van der Putten et al., 2017), but research is still needed to fully characterize the light remitted from other ocular fundus structures.

Alternatively, oximetry can be performed without a full optical path model. Scanning techniques with depth discrimination, such as visible light-OCT (vis-OCT) (Yi et al., 2013; Shu et al., 2017), are able to isolate just the light paths traversing retinal vessels and provide oximetric data. Widefield approaches based on modified fundus

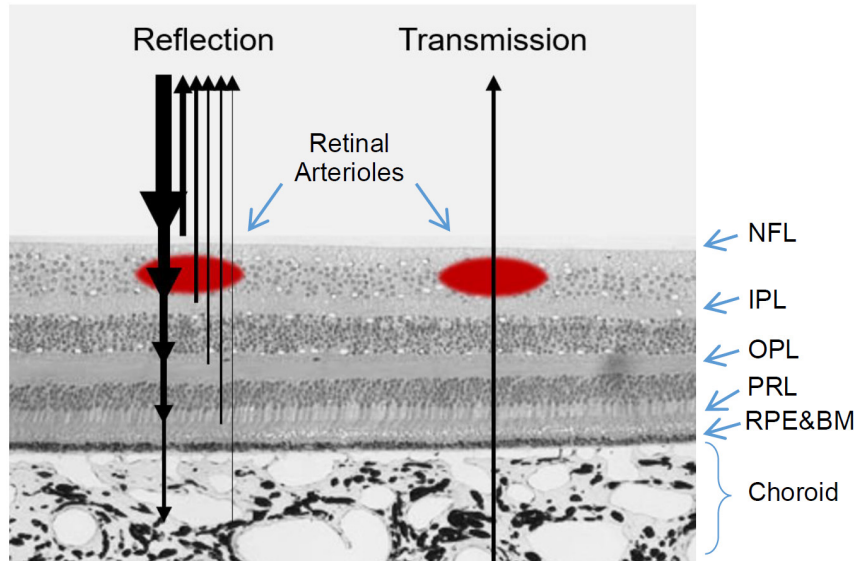


**Figure 2-1:** Light paths for fundus imaging in reflection (left), and transmission (right) illumination geometries overlaid on a histological section. Arrow line thickness represents relative light intensity, while adjacent arrows indicate multiple possible paths. In reflection geometry, reflections from several retinal layers sum to dominate potential contrast obtainable from deep layers. Additionally, absorption pathlength is uncertain because there are several possible paths. Hypothetical transmission retinal imaging does not suffer from either of these drawbacks. Red arterioles are exaggerated for clarity. NFL: nerve fiber layers, IPL: inner plexiform layer, OPL: outer plexiform layer, PRL: photoreceptor layer, RPE & BM: retinal pigment epithelium and Bruch's membrane. Histological image adapted from (Leung and Snodderly, 2001).

cameras (Hickam et al., 1963; Beach et al., 1999; Hardarson et al., 2006; Hammer et al., 2008) also provide oximetric data with the aid of a calibration. Recently ML has also been employed to help estimate retinal oxygen saturation (DePaoli et al., 2019).

### 2.1.3 Imaging spectroscopy artifacts

Widefield retinal oximetry is crucially dependent on calibration and is susceptible to artifacts related to specular back reflections (reflex). These artifacts obscure the spec-

tral signatures used to detect chromophores. A well-known artifact is central vessel reflex (Fig. 2.2) which appears as bright glints near the center of otherwise absorbing vessels (Delori et al., 1977; Narasimha-Iyer et al., 2008). The reflex is more intense for large arteries, and may appear and disappear repeatedly along the length of the vessel, leading to the so-called “rattlesnake” artifact in oximetric maps (MacKenzie and Harvey, 2018). The inner limiting membrane (ILM) and superficial nerve fiber layer (NFL) of the retina also cause a smoothly varying glare across the fundus, particularly for young eyes. One can appreciate the presence of myriad sources of reflection simply by observing a typical OCT B-scan, shown in Figure 2.3. Horizontally aligned retinal components, like layers of axons or limiting membranes, appear bright. Thus, the nerve fiber layer (NFL), inner and outer plexiform layers (IPL/OPL), photoreceptor layer (PRL), and retinal pigment epithelium (RPE) contribute to the observed reflectance fundus images (Toth et al., 1997). Researchers have gone to extreme lengths to avoid these confounding reflections, even so far as puncturing the eye (of swine) to illuminate the retina from highly oblique angles (Salyer et al., 2006).

#### **2.1.4 Transmission imaging in thick tissue**

In theory, unwanted reflections could be avoided by adopting a transmission imaging geometry. The key difference is that in a reflection geometry, anterior reflection artifacts are first order in strength, whereas in a transmission geometry they are third order: at least two extraneous reflections are required to cause an artifact in the transmission direction. However, it is not immediately obvious how to achieve such a geometry without resorting to unacceptably invasive methods.

To tackle this challenge, we have taken inspiration from another light microscopy technique pioneered in the Biomicroscopy Lab, namely oblique back-illumination microscopy (OBM) (Ford et al., 2012). OBM is an imaging technique used to obtain absorption and phase contrast in arbitrarily thick samples. It may be implemented



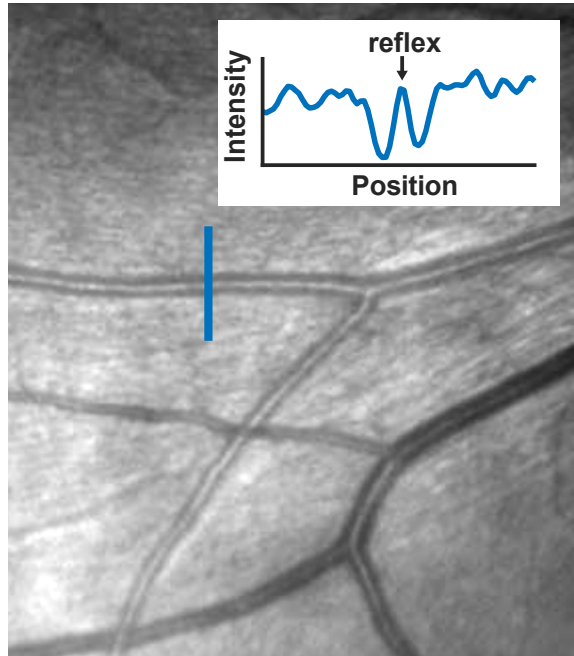


**Figure 2-2:** Strong reflection from center of retinal blood vessel and evidence of nerve fiber bundle specular reflection artifact. Adapted from (Narasimha-Iyer et al., 2008).

as a simple add-on to any brightfield microscope, as long as two illumination fibers may be fixed in place on either side of the microscope objective, as shown in Figure 2-4. One LED is turned on at a time for each camera capture. Though it may not appear so at first glance, OBM is actually a transmission-based technique. Light is transmitted through the sample structure at the focal plane before it is detected. The effect of the thick tissue below the focal plane is simply to turn the light around, by multiple scattering events, so that the light can be detected on the same side of the sample as the illumination (this is one of the few microscopy techniques where scattering actually plays a constructive role).

Most of the microscopes in the lab that we have outfitted with OBM have utilized visible illumination wavelengths. There is of course some loss due to visible light absorption over the photon's circuitous route towards the focal plane. The potential loss has been minimized because we ordinarily have the freedom to place the illu-

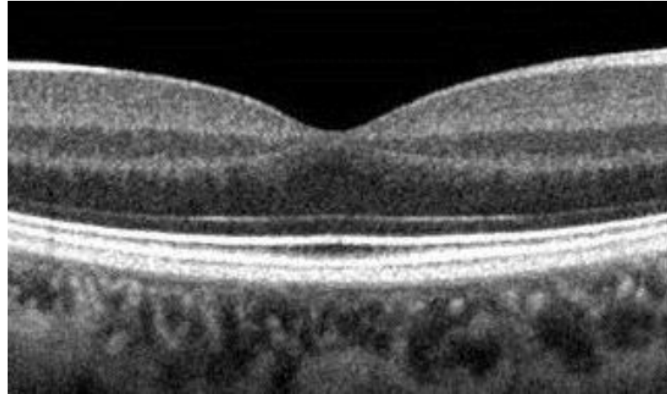


**Figure 2-3:** Spectral-domain OCT (SD-OCT) cross-sectional (B-mode) scan through a healthy retina. The dip is the location of the fovea. Adapted from (Vien, 2014).

mination fibers fairly close ( $< 2$  mm) from the center of the objective. However, if we are to apply this scattering-based illumination technique to fundus imaging, we would not have the luxury to place illumination just next to the fundus; instead, the possible pathlengths would involve a few centimeters. At these length scales, in order to sufficiently illuminate the retina, exceedingly high powers of visible light would need to be delivered to the head, which would likely exceed safe limits.

Although visible light would have a challenge reaching the fundus, near-infrared (NIR) light, due to its reduced scattering and lower absorption, routinely achieves remarkable penetration depths in biological tissue (Jacques, 2013). At such depths, NIR light has scattered so many times that it may be regarded as “diffuse”. That is, after many scattering events, the light’s original direction is completely lost, and its future path must be described stochastically as a random walk (Wang and Wu, 2007). Figure 2-5 depicts this transition to light diffusion. Thus beyond one transport mean-free-path (mfp’), the concentration of light intensity (fluence) in a homogenous sample approaches that of the analytical solution to a diffusive virtual point source. For instance, with the biologically-representative optical parameters used to generate Figure 2-5 ( $\mu_a = 0.1 \text{ cm}^{-1}$ ,  $\mu_s' = 10 \text{ cm}^{-1}$ ), mfp’ is about 1 mm. If we deliver 500 mW

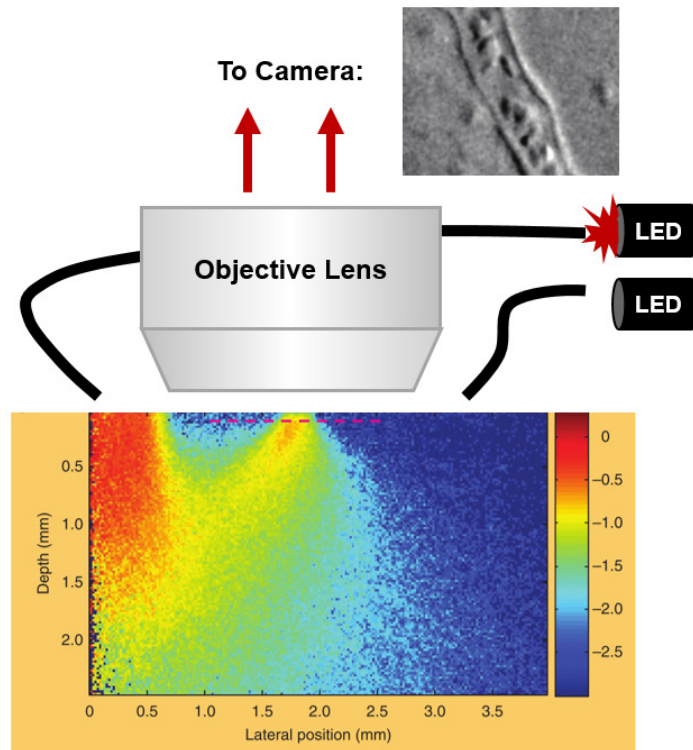


**Figure 2·4:** Concept of oblique back-illumination microscopy (OBM). OBM is a transmission-mode microscope in disguise: light delivered from fiber on the periphery of the objective scatters multiple times. A subset of the original photons traverse the focal plane (dotted). For clarity only the path of those photons are shown in the Monte Carlo simulation heatmap results. Images are obtained for each LED at a time. The difference of the two frames reveals phase gradient contrast, similar to differential interference contrast (DIC). Image of blood cells in a capillary is given as example (top right). Adapted from (Ford et al., 2012).

(about the maximum allowed for a half-inch diameter fiber bundle) to a point on the temple, and the retina is about 4-5 cm away from the temple, from diffusion theory we can roughly estimate that about  $100 \mu\text{W}/\text{cm}^2$  of light will irradiate the retina, which should be more than enough for imaging.

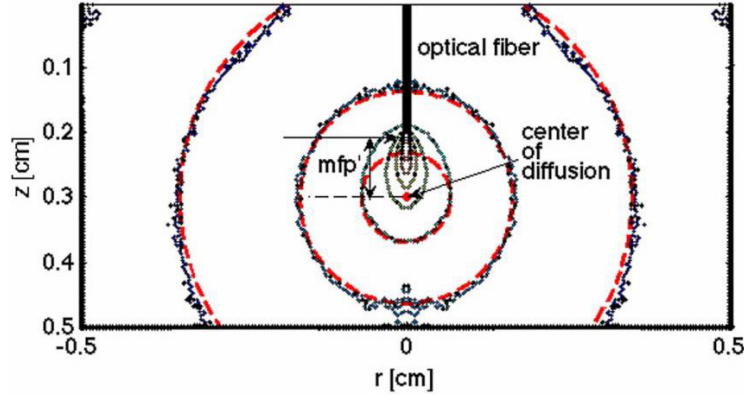


**Figure 2-5:** Density map from a Monte Carlo simulation of diffuse light transport. Lines represent contours of equal light concentration. Results from simulation (black/navy dots) compared to analytical solution for virtual diffusive point source (red). Beyond one transport-mean-free-path (mfp'), the original direction of light is scrambled due to scattering. Light paths undergo a random walk, leading to a diffusion-like light concentration gradient. Reproduced from (Jacques and Pogue, 2008).

However, we might still be wary that enough light is able to penetrate bone. A compelling argument in favor of the feasibility is the success of a similar technology called functional near-infrared spectroscopy (fNIRS) (Boas et al., 2001; Strangman et al., 2002). fNIRS illuminates the scalp with arrays of near-infrared lights. Some of the light penetrates as deep as the brain cortex before diffusing out the skull to various detectors. The spectroscopic technique quantifies changes in blood oxygen saturation to infer cortical activity.

Specifically, in this chapter, we propose an alternative widefield fundus imaging strategy based on light delivered transcranially through the subject's temple. The

light diffuses through the bone and illuminates the retina not from the front, as in standard techniques, but rather mostly from the back. As such, images are formed from light *transmitted* through the retina rather than *reflected* from the retina. To appreciate anatomic scale, in Figure 2·6 we have overlaid a sketch of our solution onto a transverse cross section of the human head. Light from NIR LED light sources is coupled into the proximal end of a large area fiber bundle (coupling not shown). The distal end of the bundle is held to the subject's temple, gently compressing fat and muscle, while bringing the light source closer to the posterior eye. After entering tissue, the light quickly enters the diffusive regime. A minor portion of the light diffuses towards the eye and back-illuminates the fundus. Light transmitted through the retina is collected by the ocular lens and refocused by fundus camera (FC) optics onto a digital camera sensor. Optionally, the subject's head can be positioned such that the posterior eye is rotated in its orbit towards the temple, thus reducing the total pathlength diffuse light must traverse in order to reach the retina.

In this way, the image formation is conceptually similar to that of OBM (Ford et al., 2012), which is capable of transmission-like phase-gradient and absorption contrast microscopic imaging in thick tissue. The use of NIR light also permits imaging without mydriatics or uncomfortable flash exposures.

The contents of this chapter is based on a previous paper (Weber and Mertz, 2018a) and first presented in a conference proceeding (Weber and Mertz, 2018b).

## 2.2 Transcranial illumination fundus imaging system

The system consists of illumination and detection subsystems shown together in Figure 2·7(A) and detailed separately below. An example raw transcranial fundus image is provided in Figure 2·7(B).

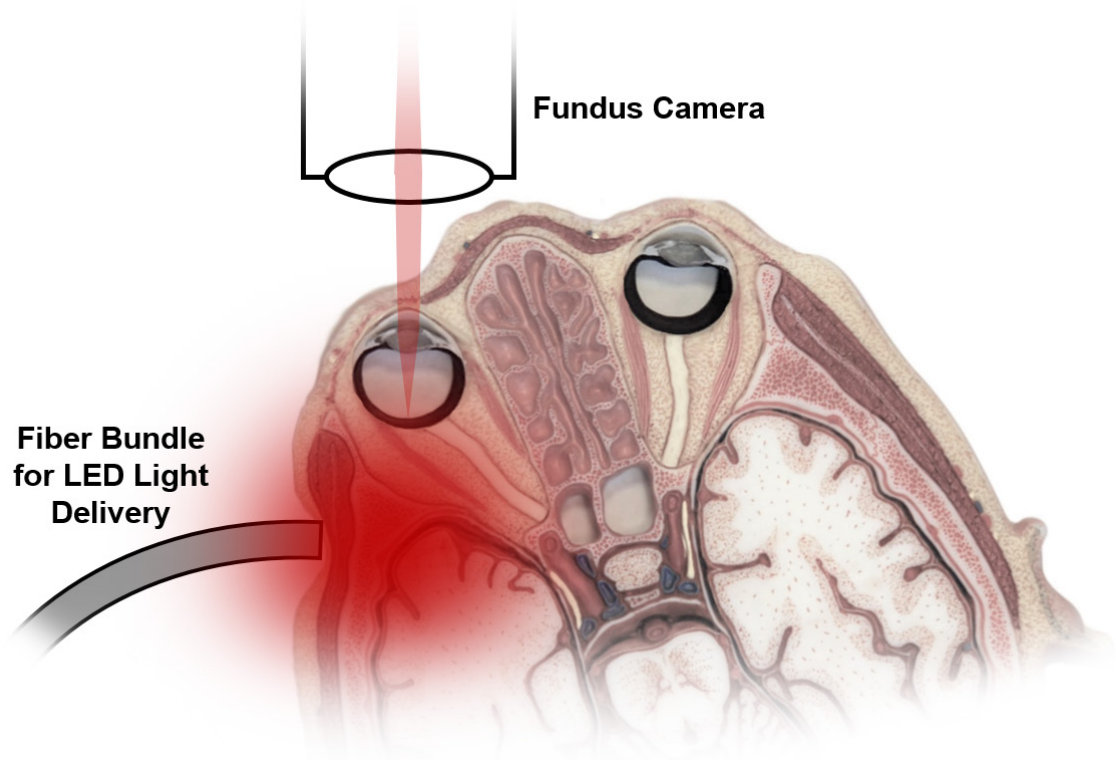


**Figure 2-6:** Proposed transcranial back-illumination technique shown with human head transverse section through orbits. NIR light (red) is delivered at the temple (compressed slightly). The subject's gaze is rotated medially. Light diffuses through skin, bone, and muscle, and a portion of the original power illuminates back of the eye. A regular fundus camera (with its built-in illumination disabled) captures images with transmitted light.

### 2.2.1 Transcranial illumination

According to the theory of diffuse light transport (Jacques and Pogue, 2008), only a small fraction of the total light available is expected to penetrate centimeters through the head and illuminate the posterior eye. Light-emitting diodes (LEDs) represent a cost-effective and scalable means of obtaining the necessary light power at several wavelengths in the NIR spectrum. Five high-power LEDs ranging in center wavelength from 660 to 940 nm were used to provide transcranial illumination (detailed in Table 1). When active, an LED driver (Thorlabs, LEDD1B) applied the maxi-

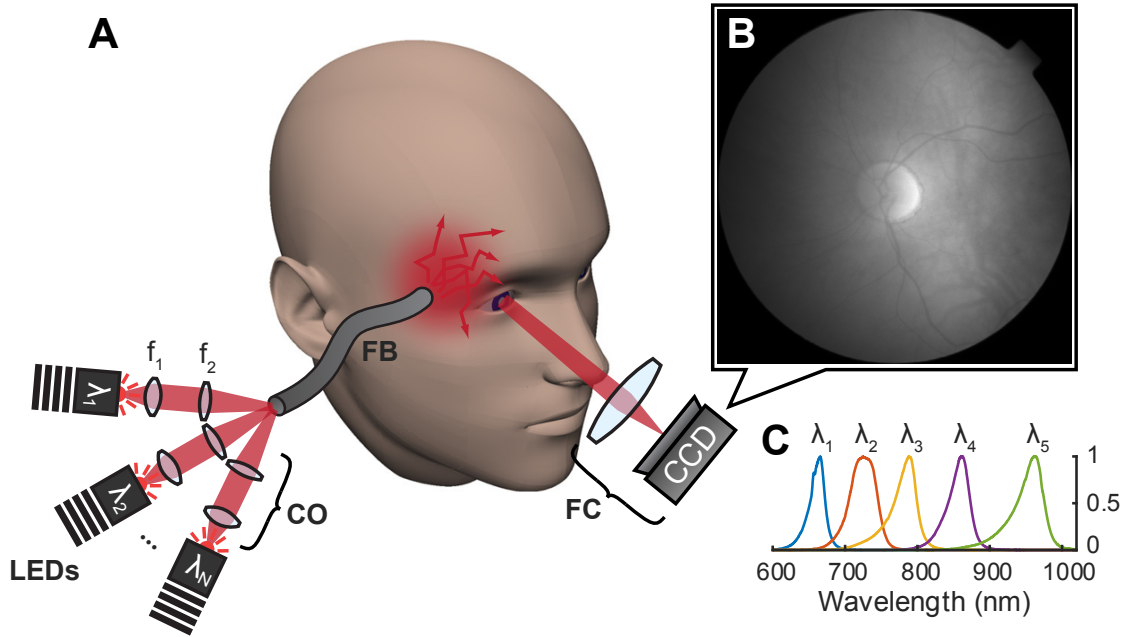


**Figure 2-7:** Simplified schematic for fundus transcranial illumination and imaging with sample image and illumination spectra. A: Graphical description. LEDs at several central wavelengths ( $\lambda_N$ ) are imaged via coupling optics (CO), comprised of lenses  $f_1$  and  $f_2$ , onto the proximal end of a flexible fiber bundle (FB). A commercial fundus camera (FC) images the transilluminated fundus onto a camera (CCD). B: Example raw image recorded on the CCD. C: Normalized measured spectra of available high-power deep red and NIR LEDs.

num specified current to the particular LED. Resulting spectra are shown in Figure 2-7(C). To avoid possible subject discomfort resulting from direct contact with hot LED printed circuit boards (PCBs), the light was delivered remotely through a 13 mm-diameter flexible fiber bundle. Each LED was imaged onto the proximal end of the fiber bundle ( $f_1 = 16$  mm, Thorlabs ACL25416U-B;  $f_2 = 60$  mm, Thorlabs LA11340-B). The distal end of the bundle was gently pressed onto the skin near the subject's temple. With careful (three-dimensional) alignment, either four or six LEDs could be coupled into the bundle. We 3D printed a custom mount (mixed with conventional optomechanical parts) to maintain LED alignment, shown in Figure 2-8.

Each LED beam path shared a portion of the fiber bundle’s distal end acceptance cone. In this way, different combinations of LEDs (or several at the same wavelength) could be simultaneously active, however this feature was not used in the present study.

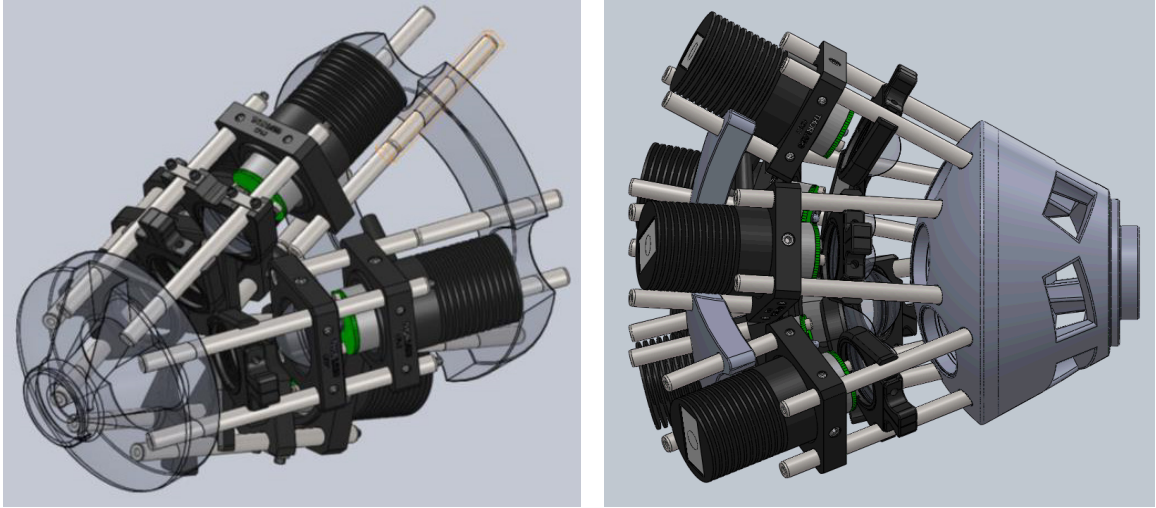


**Figure 2.8:** 3D CAD rendering of a custom 4-channel (left) or 6-channel (right) LED-to-fiber bundle combiner. Different wavelength LEDs can be inserted into each channel. Transparent gray parts are 3D printed.

After convergence and transmission through the fiber bundle, a power meter was used to measure irradiance to compare with the ANSI Z136.1 safety standard (ANSI, 2014). The measured irradiance at each wavelength was equal to or below the standard’s maximum permissible exposure (MPE) for skin (see Table 2.1). Continuous exposure (i.e. >10 sec) was assumed. The spectral full width at half maximum (FWHM) for each LED was small enough that only the LED center wavelength was considered. Retinal exposure is discussed in a later subsection.

### 2.2.2 Fundus camera and CCD sensor detection subsystem

A modified Topcon TRC-NW5S non-mydratic fundus camera was used to image the transilluminated fundus. In the present study, the 45° angle of view setting was used exclusively. This angle of view corresponds to a 13-mm arc along the retinal surface.



The fundus camera’s built-in illumination system was disabled and a dichroic mirror that normally splits the observation (NIR) and photography (visible flash) beam paths was removed so that all wavelengths collected by the fundus camera were directed to the camera port. The original color camera was replaced with a newer monochrome CCD camera (PCO Pixelfly USB: 1392x1040 pixels, 68 dB dynamic range, 16 ke<sup>-</sup> well capacity). The camera was operated in “IR boost” mode, which enhances the quantum efficiency (QE, ranging from 47% at 660 nm to 6% at 940 nm).

To make use of the new sensor’s larger format, the total magnification was adjusted by axially displacing the final relay lens and moving the camera to the new focal plane. Final magnification was about 0.5x and camera pixels corresponded to 13  $\mu\text{m}$  on the retina. With additional magnification, pixel size could be further reduced, however, ultimately the numerical aperture (NA), and thus resolution, is limited by the internal stop of the fundus camera itself. For the non-mydratic fundus camera used in this study, the NA is about 0.038, which in the ideal case yields a diffraction-limited spot size on the retina of about 11  $\mu\text{m}$  for 850 nm light.

To compensate for an intensity gradient from the temporal to nasal side, a gradient

**Table 2.1:** LED choices, associated ANSI maximum permissible exposures (MPEs) for skin and retina, and measured or estimated irradiance. Retinal MPE is converted from ANSI ocular exposure MPE. Estimation is based on received light power on the camera (see text for details). Part numbers are from the Thorlabs catalog.

Center wavelength /FWHM (part #) (nm)	Skin exposure		Retina exposure	
	MPE (mW/cm <sup>2</sup> )	Measured (mW/cm <sup>2</sup> )	MPE (mW/cm <sup>2</sup> )	Estimated ( $\mu\text{W}/\text{cm}^2$ )
660/25 (M660L3)	200	200	290	62
730/37 (M730D2)	230	200	670	120
780/30 (M780D3)	290	120	840	60
850/30 (M850D2)	400	270	1200	170
940/37 (M940D2)	600	200	1800	55

neutral density filter (Thorlabs, NDL-25C-2) was inserted near an intermediate image plane and defocused slightly. With higher dynamic range cameras (e.g. sCMOS), this filter is unnecessary. The light transmission of the system was measured using a HeNe laser, co-aligned with the system’s optical axis. Roughly 60% of the beam was transmitted.

### **2.2.3 Custom GUI and LED toggle**

A custom graphical user interface (GUI) was written in MATLAB to coordinate and synchronize the illumination and detection subsystems, by way of an Arduino, which was programmed to act as a reconfigurable digital toggle triggered by the camera’s exposure-out signal. Thus, the different LED channels were turned on sequentially in synchrony with the camera exposure.

### **2.2.4 Transcranial retinal exposure and spectral transmission**

The ANSI Z136.1 standard (ANSI, 2014) assumes hazardous beams will enter the eye through the pupil. Therefore, the standard specifies ocular MPE in terms of corneal irradiance, which is not directly applicable to transcranial transmission imaging where light primarily exposes the retina from behind. Assuming an “extended source”, the corneal MPEs were converted to equivalent retinal MPEs as described previously (Delori et al., 2007), and listed in Table 1.

While a direct measurement of the actual in vivo retinal exposure is impossible, with knowledge of several parameters, we may estimate a quantitative relationship between recorded pixel value and retinal exposure. These parameters are camera pixel area ( $41.6 \mu\text{m}^2$ ), QE, exposure time, magnification, system transmittance, ocular media transmittance (Geeraets et al., 1960), entrance pupil diameter (about 1 mm, set by fundus camera), and eye focal length (17 mm). Additionally, we assume the light at the retina has a Lambertian angular distribution. To account for attenuation due

to the retinal pigment epithelium (RPE), we assume the light exiting the retina has also traversed a 20  $\mu\text{m}$ -thick absorbing layer with a wavelength-dependent absorption coefficient (Jacques, 1998). The estimated exposures are all orders of magnitude below the MPE values, which should allay concerns about the absolute accuracy of this estimate.

Since LEDs have moderate spectral bandwidth (see Table 1), transmission through skin, bone, and brain is expected to only moderately impact the shape of the spectrum incident on the back of the fundus. This was verified separately by temporarily replacing the camera in our system with a fiber-coupled spectrometer (Thorlabs CCS175 with 1 mm-diameter fiber patch cable). The empirical transmission results were combined with the QE and the resultant transmission-responsivity curve was used to correct the weighted average absorption coefficient for each chromophore (oxy- and deoxyhemoglobin,  $\text{HbO}_2$  and  $\text{Hb}$ ) at each LED channel. The weighted average absorption coefficients in the intermediate wavelength range (730, 780, and 850 nm LEDs) were found to be less sensitive to the correction ( $< 2\%$  change). However, at 660 nm the weighted average absorption coefficients of  $\text{HbO}_2$  and  $\text{Hb}$  were each reduced by 8%. This is primarily due to strong absorption on the shorter wavelength end of the LED spectrum. The light spectrum incident on the retina is red-shifted, and hence the absorption coefficients are reduced since the spectra are both decreasing around 660 nm. Additionally the weighted average absorption coefficient of deoxyhemoglobin was increased by 26% at 940 nm. In this case the dramatic change is mostly due to the dwindling QE around 940 nm, which effectively blue-shifts the detectable spectrum.

### 2.3 Subjects and imaging sessions

Four asymptomatic eyes from four normal subjects (23-59 years of age, mean age 46, one female and three males) were imaged. The subjects presented a wide range

of choroidal pigmentation, with corresponding (usually correlated) iris colors ranging from blue to brown. For each subject, informed consent was obtained prior to imaging. The research was approved by the Boston University Institutional Review Board.

For each imaging session, the subject fixated on an external target such that the optic disc was centered in the image. Although the system has the capability to temporally interleave LEDs for quasi-simultaneous multispectral imaging, the camera's maximum frame rate limited this capability. For instance, enabling three color channels reduced the multispectral frame rate to 4 Hz. Because light from the 660 and 730 nm could be weakly perceived, while the others LEDs generally could not, temporal multiplexing of the LEDs effectively caused 4 Hz blinking across the whole field of vision, which was irritating to the subject. Instead, a long series of frames from the same LED were acquired. A 256-frame series was completed in about 26 sec. For one subject (59-year-old white male, moderate pigmentation), a complete multispectral dataset was acquired by repeating this process for all five LEDs. This dataset was chosen for more detailed analysis and displayed throughout this article.

To ensure that the ANSI-equivalent retinal MPE was not exceeded, the MPE-equivalent maximum allowable pixel value (for a given exposure time) was calculated a priori. The LED current was carefully increased and pixel values were continually monitored to confirm permissible exposure. None of the light conditions used in this study came close to exceeding equivalent retinal MPEs.

## 2.4 Image processing

Although the use of NIR light permits deep tissue penetration, its major disadvantage is significantly reduced intrinsic absorption contrast, particularly for hemoglobin, which drops precipitously past 600 nm (Prahl, 1999). For example, consider a 30  $\mu\text{m}$ -diameter arteriolar vessel (about the size of the small vessel labeled with arrowheads

in Fig. 2·9(B) & (C)). The absorption coefficient of highly oxygenated arterial blood at 850 nm is approximately  $5.5 \text{ cm}^{-1}$ . Light passing through the diameter of this vessel is only attenuated 1.6%. With the exposure conditions used to obtain Fig. 2·9(A), an average of 3800 photoelectrons ( $e^-$ ) per pixel are detected. The expected signal due to the small vessel is thus  $61 e^-$ . In comparison, the root-mean square (rms) noise in a shot noise-limited system is  $62 e^-$ , meaning that the signal-to-noise ratio (SNR) is no better than unity. Therefore, the vessel cannot be reliably detected with the exposure conditions used for Figure 2·9(A).

#### 2.4.1 Image registration and averaging

To improve SNR (i.e. increase detected photoelectrons), we record a series of shot-noise-limited frames, register each frame post-hoc, and average the registered frame series in time. Custom software was written in MATLAB, based on classic algorithms (Reddy and Chatterji, 1996; Guizar-Sicairos et al., 2008), to register sequential frames to subpixel precision and account for slight rotations from torsional eye movements. A plot of the detected translational (green: X, magenta: Y) and rotational (cyan) movements versus time for a typical image series is shown in Figure 2·9(D). With the exposure duration used in the present study (about 100 ms), eye motion inevitably corrupts a number of frames. The registration software detects and automatically excludes motion-corrupted frames from the final high-SNR average (shown as red background in Fig. 2·9(D)). The number of frames averaged ranged from 125 to 223 (out of 256), depending on the level of eye movement. The camera records 14-bit images, however we expand this range to 16-bits for data storage.

A comparison between a single frame and the high-SNR average frame is shown in Figure 2·9(B) & (C) with attendant line profiles plotted in Figure 2·9(E). No apparent loss of resolution is observed and variation is now limited by the underlying variation of the fundus itself.

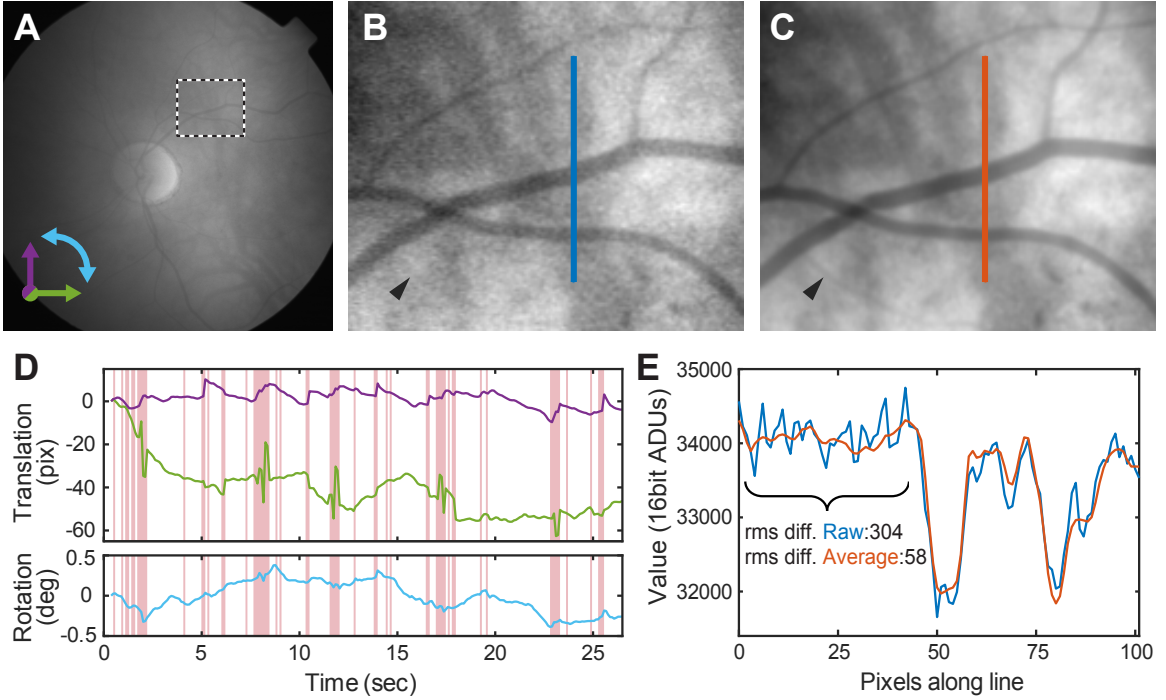


**Figure 2-9:** Registration and averaging improve SNR for intrinsically low contrast NIR retinal vasculature imaging. (A) Single frame from 850 nm LED image series (10 Hz acquisition). (B) Magnified view of highlighted region in A. Black/white levels are scaled to the region's min/max values. (C) 194-frame average improves SNR, revealing previously undetectable small features (arrowheads in B & C). (D) Detected translation (green: X, magenta: Y) and rotation (cyan) for 256-frame series. Motion-corrupted frames (red-background) are excluded from averaging. (E) Profiles for lines drawn in B & C, demonstrating SNR improvement. (rms diff.: Root-mean-square pixel to pixel difference)

#### 2.4.2 Relative absorbance calculation

Absorbance is calculated from transmitted and incident light power measurements:

$$A = -\log\left(\frac{I_{\text{trans}}}{I_{\text{inc}}}\right) \quad (2.1)$$

As is apparent in Figure 2-9(A), the illumination for transmission fundus imaging was not spatially uniform. To accurately compute absolute absorbance, the incident

light power as a function of location must be known. Since direct measurement of this is infeasible, we instead calculate a relative absorbance as follows.

First, the high-SNR average image (Fig. 2·10(A)) is corrected for slowly varying global illumination changes by fitting the image to a polynomial surface, avoiding the bright optic disc area. The average image is divided by the fit to produce a flattened image (Fig. 2·10(B)). Next the flattened image is local maximum filtered, that is, each pixel is replaced with the maximum value in a circular local area around the pixel. The filtered image is smoothed with a Gaussian kernel equal to half the diameter of the local maximum filter, producing Fig. 2·10(C). This smoothed local maximum image is used as a proxy for the incident light power to compute absorbance. In other words, this method calculates absorbance *relative the minimum absorbance* in a local neighborhood around each pixel. Technically, this should be referred to as relative attenuation, a more general term that additionally includes loss due to scattering outside the acceptance angle of the optical system. Such loss may happen, for instance, at blood vessels where erythrocytes are known to cause scattering (Hammer et al., 1998). However, in subsequent analysis the effect of spatially varying scattering loss is neglected. The assumption is that scattering is reduced and/or very strongly forward-directed when using NIR light.

## 2.5 Results

Preliminary results are shown in Figure 2·11. As predicted, the transillumination images in Figures 2·9, 2·10, and 2·11 are free from spurious back-reflections, either from the retinal ILM or NFL, which, in a conventional reflection-mode imaging, collectively appear as a glare that intensifies towards the optic disc. The images presented here (Fig. 2·9(B) & (C), especially) are also free from central vessel reflex. Interestingly, the optic disc appears bright compared with the fundus background, possibly due to

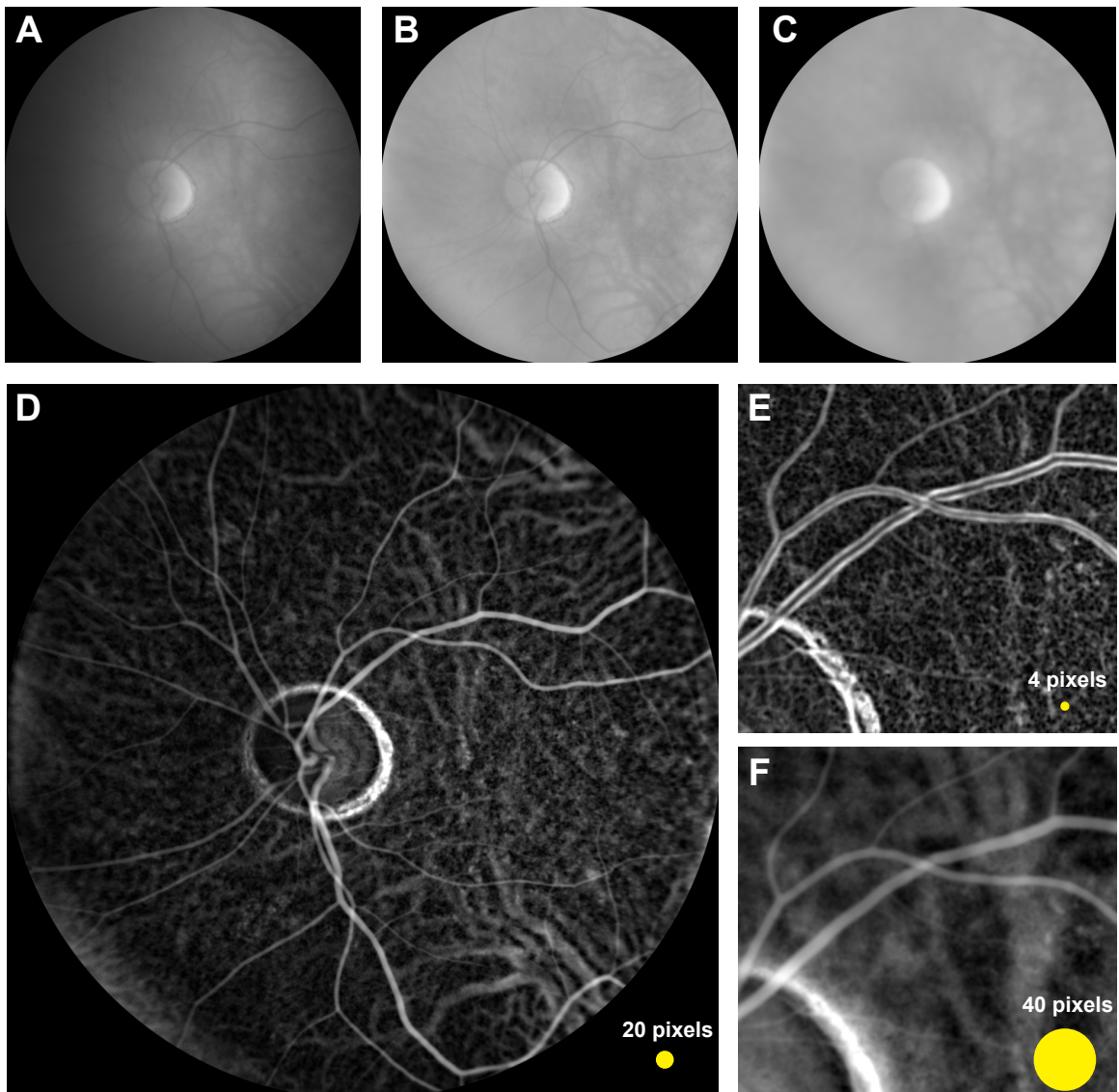


**Figure 2-10:** Demonstration of local maximum filtering and relative absorbance images from left eye of a healthy 59-year-old subject. (A-D) Relative absorbance calculation with 850 nm transillumination (refer to text for details). Yellow circle indicates size of the local maximum filter kernel relative the image. (E) & (F) Effect of changing local maximum filter kernel radius (zoomed region of D). A smaller radius emphasizes sharp changes in absorbance, revealing mottled pigmentation density fluctuations. Larger kernels emphasize larger features such as vessels in the choroid.



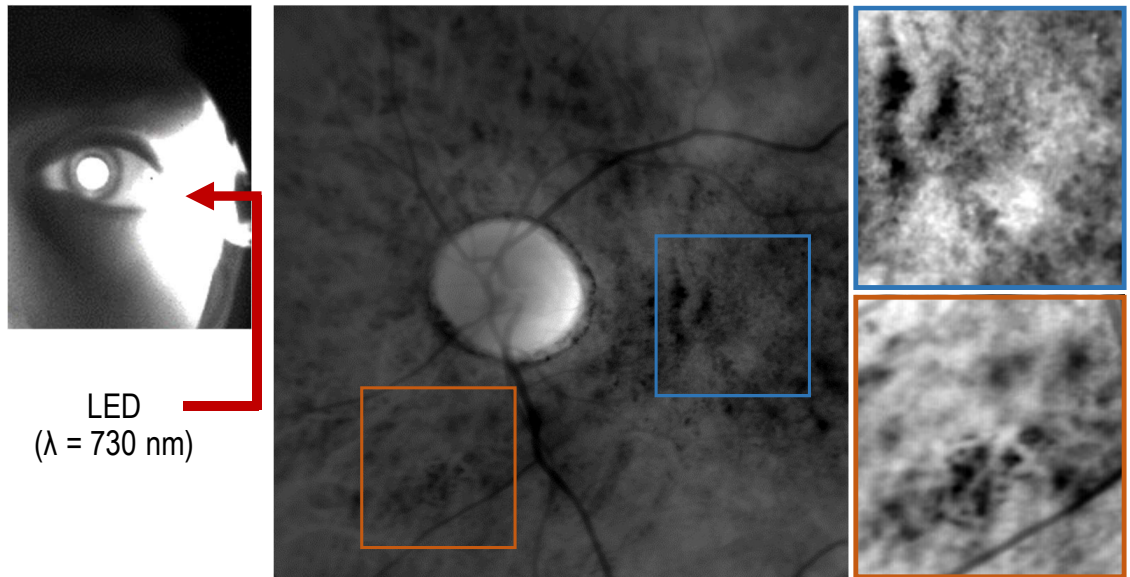


**Figure 2-11:** Transcranial back-illumination proof of concept test. (Left) 730 nm LED light emitted from fiber bundle clearly reaches the eye. (Center) Fundus image from 59-year old male volunteer with no eyeglass prescription, around the optic nerve, which appears bright due to the lack of pigmentation in the nerve. Paired arterioles and venules are distinguishable due to that fact that Hb is a stronger absorber than HbO<sub>2</sub>. (Right) The blue area shows slight pigment aggregation and orange area shows very fine vessels we believe are choroidal. The contrast settings for the blue and orange areas of interest has been auto-scaled to enhance visibility.

anisotropic forward scattering parallel the axonal fibers, and also likely due to the absence of underlying choroid and RPE pigment.

The contrast of the relative absorbance image (Fig. 2-10(D)) resembles that obtained with fluorescein angiography, since at 850 nm HbO<sub>2</sub> and Hb have similar absorption. A bright ring around the border of the optic disc is generated when the local maximum filter's spatial kernel intersects with the (relatively) bright disc. Thus the filter overestimates incident light power near the optic disc. A more sophisticated approach might segment the disc from its surroundings and compute local maxima for each domain separately. Regardless, we caution against using the relative ab-

sorbance representation when inspecting interfaces, such at the edge of the optic disc or, in cases of AMD or diabetic retinopathy (DR), near retinal scars, edemas, or focal deposits. Instead we recommend using the transmitted image (Fig. 2·10(A) or (B)), which should be free from this processing artifact.

In the relative absorbance images, visibility of certain features appears to depend on the diameter of the maximum filter kernel used. Namely, a small kernel highlights rapidly varying, tenuous features, tantamount to high-pass filtration because the local maximum-filtered image over such a small kernel is nearly a low-pass version of the image. Outside the optic disc, the distinctive mottled appearance of RPE pigment density variations is apparent (Delori et al., 1977). On the other hand, larger kernels emphasize large-scale features, such as large choroidal vessels, which are clearly visible in the background of Figure 2·10(F).

Notably, there is no evidence of the fovea, which under visible light fundus photography ordinarily appears as a dark spot 2-3 optic disc diameters temporal the optic disc. The absorbance of foveal/macular xanthophylls is well-known to be low for the NIR wavelengths used in this study (Snodderly et al., 1984).

### **2.5.1 Multispectral imaging and chromophore unmixing**

Data obtained using the other LED channels are processed in a similar way as to Section 2.4.2 and shown in Figure 2·12. As the wavelength of transillumination is scanned, two changes are obvious. First, for shorter wavelengths (660 and 730 nm), retinal arteries nearly disappear. This finding is well-known and explained by noting that under normoxia, arteries are highly oxygenated, and the absorbance of oxygenated hemoglobin is minimal around 690 nm (see Fig. 2·13(A) for complete HbO<sub>2</sub> and Hb absorption spectra). Retinal veins, however contain a mixture of HbO<sub>2</sub> and Hb, which results in broadband absorbance across the NIR spectrum and explains why retinal veins are visible in each spectral image.

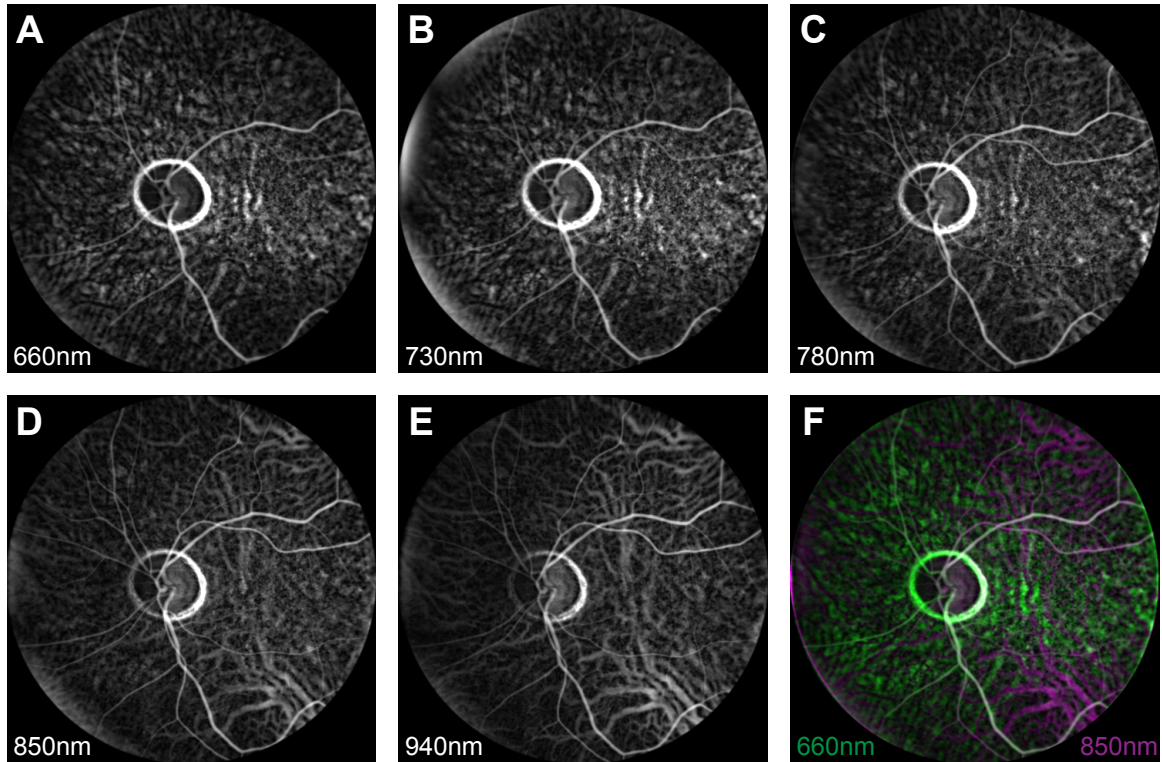


**Figure 2-12:** Relative absorbance images for several indicated NIR wavelengths in the retina near the optic disc. (A-E) Multispectral relative absorbance images. Brightness has been autoscaled for clarity. (F) 660 and 850 nm images overlaid in false-color for comparison. Vortex veins are readily observed in the top right and bottom right fields of 850 and 940 nm images.

The second notable change involves a contrast inversion of the large choroidal vessels. For shorter wavelengths, choroidal vessels appear dark, meaning that they are weaker absorbers than their surroundings (i.e. the extravascular stroma). For longer wavelengths (850 and 940 nm), choroidal vessels appear bright, meaning that they absorb more than the extravascular stroma. The extravascular stroma contains melanocytes which, for short wavelengths (660 and 730 nm), are highly absorbing. With increasing wavelength, the absorption of melanin monotonically decreases (Fig. 2-13(A), dotted line), while oxyhemoglobin absorption increases. Since choroidal vas-

culature is known to be highly oxygenated, beyond 780 nm, the choroidal vessels exhibit more absorbance than the extravascular melanin-containing stroma, explaining the contrast inversion. These observations are consistent with previous studies (Delori et al., 1977; Elsner et al., 1996) that assessed visibility of subretinal structures with NIR light.

To register each spectral image, we manually selected at least 10 retinal vein bifurcation points, estimated the movement, and applied a similarity transform. Two registered images, which exhibit both contrast changes mentioned above, are shown together in false color in Fig. 2.12(F).

With spatially-aligned multispectral images, one can also “unmix” the contributions from individual chromophores to the total observed absorbance via the Beer-Lambert law. Thus, a system of equations relating chromophore concentration to absorbance at each spectral channel may be written. Concentrations are averages over the volume approximately defined by the depth of focus and pixel area. The coefficients are equal to the weighted-average absorption coefficients for each chromophore over each LED spectrum (corrected with the transmission-responsivity curve explained at the end of Sec. 2.2.4). The system of equations is solved separately at each pixel using either a pseudoinverse or a non-negative least squares optimization routine (standard functions in MATLAB), the latter applying a positivity constraint to the estimated chromophore concentrations. The non-negative least squares solution was preferred for displaying chromophore maps, but produced less smoothly varying background estimates, particularly when the estimated chromophore concentration was around zero. The pseudoinverse solution yielded a smooth background which was preferable for the image inpainting problem described later.

Non-negative least squares-based unmixing of  $\text{HbO}_2$  and Hb is shown in Figure 2.13(B). The 940 nm channel was not included due to uncertainty in the large 26%

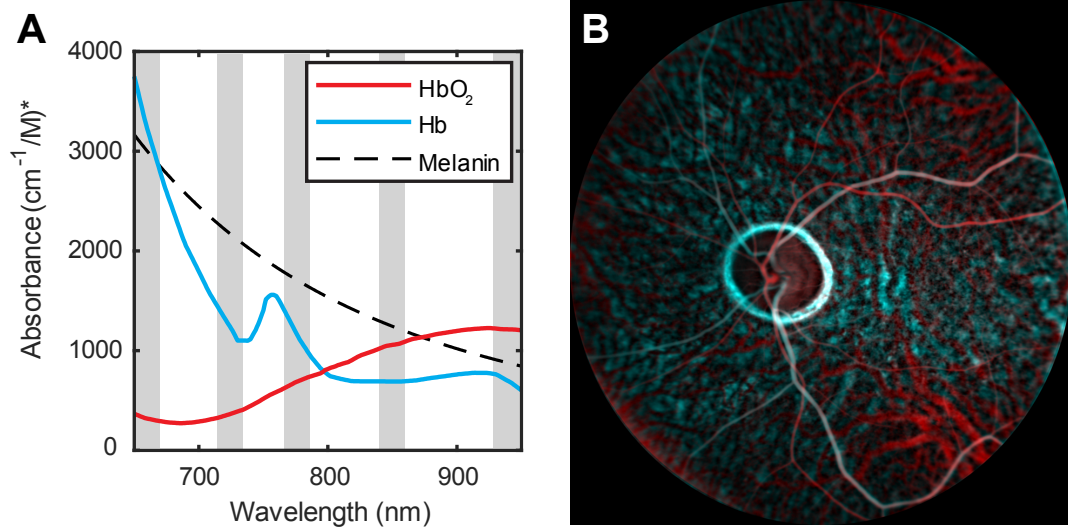


**Figure 2-13:** Linear spectral absorbance unmixing of contributions from dominant chromophores in the fundus. (A) The absorption spectra for the three dominant NIR chromophores of the eye. Gray background indicates available LED channel. (B) Oxy- and deoxyhemoglobin (HbO<sub>2</sub> and Hb) distributions based on absorption spectra in A and non-negative least squares spectral unmixing, using 660-850nm relative absorbance images. Hemoglobin spectra obtained from (Prahl, 1999) and average melanin slope from (Jacques, 1998). (\*Melanin spectrum scaled to permit comparison with hemoglobin. Units do not apply.)

weighted-average absorption coefficient correction for deoxyhemoglobin. The deoxyhemoglobin channel (cyan) in Figure 2-13 likely contains contribution from melanin in the pigmented extravascular choroidal stroma. However, incorporating melanin as a third component in unmixing yielded poor results (not shown), likely because at the discrete wavelengths used, the orthogonality between Hb and melanin is small.

### 2.5.2 Retinal oximetry

With estimates for HbO<sub>2</sub> and Hb concentration, oxygen saturation may be readily calculated as,

$$SO_2 = \frac{[HbO_2]}{[Hb] + [HbO_2]} \times 100\% \quad (2.2)$$

For a quantitative comparison with results from previous retinal oximetry studies, chromophore concentrations in retinal vessels must be isolated from the influence of the choroidal background, which can be quite significant for NIR transillumination. Relative to the retinal vessels, the background is generally slowly varying, (i.e. only the largest choroidal vessels are visible). Thus the background may be numerically estimated using an image restoration technique known as inpainting. For this study, a simple inpainting algorithm that is included in MATLAB was used. Essentially the algorithm interpolates unknown pixel values based on the solution to Laplace's equation subject to discrete 2D boundary conditions given by the value of the surrounding pixels. The process is graphically illustrated in Figure 2.14(A). First, clearly delineated retinal vessels are manually segmented from HbO<sub>2</sub> and Hb maps. Pixels within segmented vessels are set to zero. The background is estimated with inward interpolation (inpainting). Finally, the background-estimated image is subtracted from the original chromophore image, which removes substantial variation and offset introduced by the choroidal background.

For retinal oximetry, a larger local maximum filter kernel (32 pixels) was used for the relative absorbance calculation and the pseudoinverse was used to provide the spectral solution. These tended to produce a more smoothly varying background for which the background removal strategy outlined above performed well. Several large branching retinal arteries and veins were segmented and background-corrected. Veins over the optic disc exhibited mild spontaneous venous pulsation causing blurring in the average image. These veins segments were therefore excluded from oximetric analysis. The corrected vessel maps were smoothed using a low pass filter (Gaussian, 32-pixel FWHM), to remove disruptions near vessel intersections. The effect of this

low pass-filter is shown as dotted lines in the line profiles of Figure 2-14(A). Estimated  $\text{SO}_2$  is overlaid in pseudocolor onto a map of total hemoglobin concentration and shown in Figure 2-14(B).

Additionally, the mean and standard deviation of  $\text{SO}_2$  were computed for different anatomical regions around the optic disc and summarized in Table 2.2. The arteriovenous (A-V)  $\text{SO}_2$  difference is also given for each region, as a relative indicator of local oxygen extraction and metabolic demand. The combined average  $\text{SO}_2$  was 89% for arteries and 57% for veins (32% A-V difference).

**Table 2.2:** Quantified retinal oximetry results in regional quadrants and across the whole fundus shown in Figure 2-14.  $\text{SO}_2$ : % oxygen saturation, temporal: right side of image, superior: top.

Anatomical region	$\text{SO}_2$ mean $\pm$ S.D. (# pixels)		A-V difference
	Arterial	Venous	
Superior temporal	$88 \pm 5$ (6849)	$64 \pm 4$ (5539)	24
Superior nasal	$92 \pm 6$ (3229)	$48 \pm 7$ (2543)	44
Inferior nasal	$93 \pm 4$ (1097)	$39 \pm 3$ (1404)	54
Inferior temporal	$87 \pm 6$ (4877)	$58 \pm 5$ (7139)	29
Combined	$89 \pm 6$ (16,761)	$57 \pm 9$ (16,625)	32

## 2.6 Discussion

### 2.6.1 Retinal vessel oximetry

Compared with prior work, the arterial and venous retinal  $\text{SO}_2$  values presented here appear reasonable. Previously, for arterial  $\text{SO}_2$ , Delori reported 98% using a scanning three-visible wavelength approach (Delori, 1988). De Kock et al. reported 97% with a time-resolved whole fundus pulse oximeter (de Kock et al., 1993). Hyperspectral approaches yielded 92% (Schweitzer et al., 1999) and 104% (Mordant et al., 2011), and recently visible light OCT reported an average across subjects of 92% (Chen

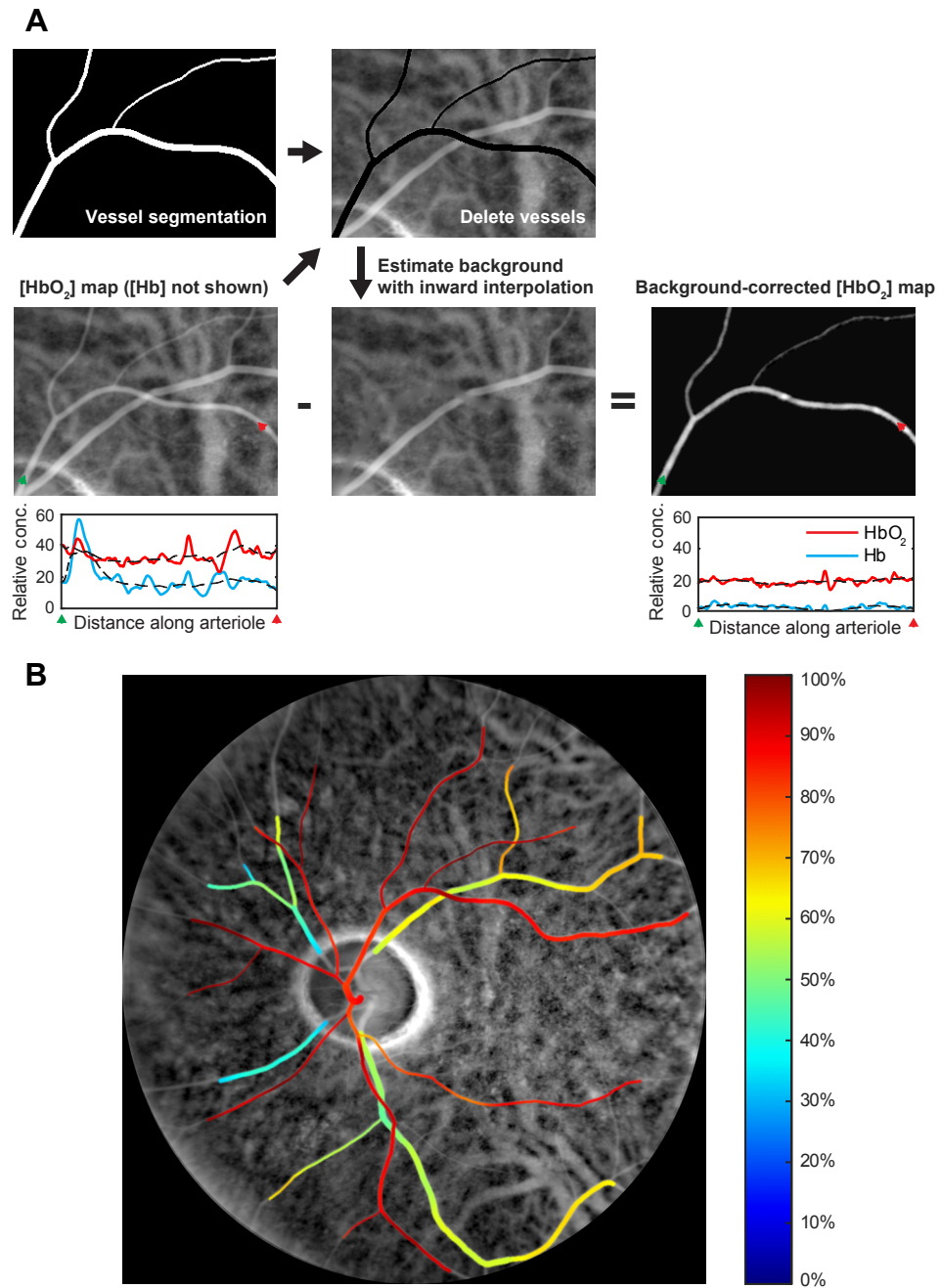


**Figure 2-14:** Chromophore background correction and widefield retinal oximetry map in fundus of the left eye of a normal volunteer. Input data is spectrally unmixed HbO<sub>2</sub> and Hb relative absorbance images using the pseudoinverse solution. A: Processing workflow leading to background-corrected vessel chromophore maps (refer to text). B: Pseudocolor overlay of SO<sub>2</sub> in major retinal vessels.



et al., 2017b). For venous  $\text{SO}_2$ , Hickam et al. reported 59% at the optic disc using a two-color photographic method (Hickam et al., 1963). Delori reported 45% (Delori, 1988). Beach and colleagues used a digital two-color imaging method to calculate 55% after correcting for pigmentation and vessel diameter effects (Beach et al., 1999). Hyperspectral techniques yielded 35% (Mordant et al., 2011) and 58% (Schweitzer et al., 1999), while an average of 77% was found using visible light OCT (Chen et al., 2017b).

For this subject, the nasal quadrants exhibited greater A-V differences. Interestingly, this is contrary to the findings of Schweitzer et al. (Schweitzer et al., 1999), who reported a statistically significant increase in A-V difference in the inferior temporal quadrant compared with the inferior nasal quadrant. Since retinal oxygen consumption is greater in darkness (Hardarson et al., 2009), one possible explanation might be that the nasal regions of the transilluminated retina, which are farther away from the light source, are exposed to less light, thus their oxygen consumption is increased relative to the temporal side. This effect would only be significant for the 660 nm LED channel, however this channel plays an outsized role in spectral unmixing due to the large difference in absorption between  $\text{HbO}_2$  and Hb. It is also possible that the gradient neutral density filter may not be perfectly neutral, leading to a system-induced bias on one side. More transillumination imaging data (preferably without the filter) is needed to confirm this relation.

### 2.6.2 Potential sources of error

It should be stressed that the oximetric results presented here were obtained without external calibration and instead used only the published extinction spectra for  $\text{HbO}_2$  and Hb. An external calibration is time-consuming, but useful in accounting for attenuation or spurious back-reflections due to tissue scattering (Beach et al., 1999). In this study, it was assumed that NIR light was weakly and predominantly forward-

scattered, which is generally valid for biological tissue. Thus, local attenuation due to spatially varying scattering (e.g. at blood vessels) was ignored and relative concentrations of oxy- and deoxyhemoglobin were calculated according to the Beer-Lambert law. This assumption is probably not absolutely true since it is known that whole blood deviates from Beer-Lambert due to multiple scattering (Anderson and Sekelj, 1967). This additional scattering attenuation might be partially offset by the possibility of some light scattering *into* the detection beam path, as in dark-field microscopy.

The attenuation due to scattering may also falsely contribute to the unmixed deoxyhemoglobin, since its spectral dependence is likely to be similar to the absorption of deoxyhemoglobin, which could explain why the average arterial  $\text{SO}_2$  determined here is somewhat lower than previous results and also why incorporating melanin into the spectral unmixing led to unsatisfactory results. Monte Carlo simulations of fundus transillumination may provide useful insights and help resolve the question of scattering attenuation in this new geometry. Certainly more sophisticated models which take into account wavelength-dependent scattering from retinal features could be adopted, however this is beyond the scope of this preliminary methodology report.

Another obvious question concerns the validity of spectroscopy obtained over the course of a few minutes. Because our camera's low frame rate prevented temporally interleaved multispectral imaging, the different LED channels were recording sequentially over a total period of 2 minutes. It is possible that vessel oxygenation can vary over this time period, however Hickham and colleagues have found little  $\text{SO}_2$  variation over this time period (Hickam et al., 1963), so such dynamics may indeed be safely neglected.

### 2.6.3 Comparison with reflection imaging

Compared with reflection-based fundus photography, transillumination fundus imaging offers several unique advantages. First, imaging penetration is deep, meaning that individual choroidal vessels are plainly visible. This is due to a combination of the NIR wavelengths used, which are only weakly absorbed and scattered in the inner retina, and the absence of spurious back-reflections, which can easily overwhelm weak signal emanating from deeper structures. Elsner and colleagues (Elsner et al., 1996) have exploited the same factors to image sub-retinal structures, but rather than a transmission geometry, they used confocal detection and an annular aperture to reject inner retinal reflection. There are also now OCT-based approaches for deep choroidal imaging (Spaide et al., 2008), which intrinsically separate anterior surface scatter. Compared to these techniques, transillumination instrumentation is considerably less complicated, and thus may be more appropriate for high-throughput disease screening. Also because the technique is single-pass, transillumination may offer some advantage in imaging retinas of patients with cataracts or other anterior eye opacities.

Second, transillumination ensures that all light detected has traversed the tissue or vessel of interest. This has important implications for retinal oximetry, where vessel surface reflections are a common confounding factor (Harris et al., 2003). Researchers have attempted to compensate for these reflections either by fitting the wings of the vessel profile to a Gaussian model (Roberts, 1987) or by choosing to analyze only the darkest point along the profile (Hardarson et al., 2006). Both of these techniques reduce the sensitivity because they essentially discard possible data points. In contrast, transillumination is free from surface reflections and may utilize the entire vessel profile for oximetric calculations.

#### 2.6.4 Potential improvements

The proof-of-concept system detailed here is far from optimized. The SNR, or more precisely, the absorption contrast-to-noise ratio, is primarily limited by shot noise, which is fundamentally linked to the number of photoelectrons generated in the camera sensor. The adoption of newer CMOS sensors, which feature higher NIR sensitivity (up to 2.5-times greater at 850 nm) and faster readout times, will increase the number of possible detected photoelectrons. As evident in Table 1, there is also the possibility of using more power, by adding several of the same LED and/or spreading the incident light over a larger area of skin. Illumination from other locations, such as the palate or nose, may also offer improved or complementary transillumination efficiency. For longer wavelengths, significantly more power may be used before reaching the ANSI Z136.1 skin MPE. This is fortunate since the quantum efficiency of silicon-based cameras decreases sharply in this spectral range. Since our aim is to demonstrate fundus transillumination on a clinically compatible platform, the current system was designed around a commercial non-mydratic fundus camera. However, the fundus camera's internal stop limits detection to just 1 mm of pupil diameter. If the fundus camera is instead replaced with a system capable of utilizing the entire naturally dilated pupil (up to 8 mm typically) for detection, light throughput is expected to increase by a factor of 64. However, unless adaptive optics (Liang et al., 1997) is used, any increase in collection will be offset by increased aberration (Atchison and Smith, 2000) thus reducing resolution. A diameter of about 3 mm is considered optimal (Liang et al., 1997) and would still yield an increase in light collection by about an order of magnitude.

### 2.6.5 Future applications

Beyond retinal vessel oximetry, which was explored extensively in this chapter, there are several additional future uses of the transcranial illumination imaging technique. The first is to estimate choroidal vessel oxygen saturation, however the processing method, which used local maximum filtering, would need to be amended in order to establish a reliable background (i.e. incident) light signal. The technique could also be used to spectroscopically detect the presence of other chromophores. For instance, there are lipid spectral peaks in the near-infrared that may be separable with multispectral contrast. Detection of abnormal lipid levels may be useful for age-related macular degeneration screening.

Another promising application that has not been explored in this thesis is for low-cost fundus imaging. With external illumination, the optics of the imaging system can be greatly simplified relative to the more complicated fundus camera, which must both illuminate and collect reflected light. In principle, the imaging subsystem could be as simple as a cell phone camera, provided the camera was sensitive to NIR light.

## 2.7 Conclusion

In conclusion, an alternative illumination method for human non-mydratric fundus imaging has been presented. It is based on the transcranial delivery of NIR light and on multiple scattering to redirect a portion of this light to the posterior eye, resulting in glare-free chorioretinal imaging. The use of NIR light enables transillumination, however at the expense of absorption contrast. We showed that with careful image processing, the contrast-to-noise ratio may be rendered adequate for oximetry measurements. Compared with conventional reflection-based fundus photography techniques, NIR transillumination simplifies absorption measurements and allows imaging deep into the choroid. Importantly, the technique is compatible with

reflection-based techniques and we have shown that it works well with a commercial fundus camera. Combining information from these two illumination approaches may improve spectroscopic analysis of the fundus. The first steps towards this multimodal image fusion are presented in the next chapter.

## Chapter 3

# Comparison of Transcranial and Reflection Fundus Imaging

### 3.1 Background

In Chapter 2, we introduced transcranial fundus imaging, a noninvasive method for obtaining single-pass transillumination images of the human fundus. As expected, images obtained from this method were free from glare and central vessel reflex. In the absence of these confounding artifacts, we were able to estimate physiologically plausible oxygen saturation values in retinal vessels using a simple linear Beer-Lambert absorption model, without the need for calibration.

While we have made some qualitative comparisons to reflection fundus images found in literature (see Fig. 2·2), quantitative comparison is generally impossible. The reason is that there are too many uncontrolled variables that influence the appearance of fundus images, and particularly the apparent optical density of retinal vessels. The latter quantity is used in vessel oximetry. Important variables include illumination wavelength (Delori et al., 1977), illumination incident vergence, fundus pigmentation (Hammer et al., 2008; Smith et al., 2001; Beach et al., 1999; Delori and Pflibsen, 1989), vessel size (Hammer et al., 2008), hematocrit, and flow velocity (Jeppesen and Bek, 2019). Adding to this difficulty, in reflection, multiple light paths contribute to the backreflected signal. Some hypothetical light paths are illustrated in Figure 3·1.

Additionally, because the light is single-pass we hypothesized that in transmission,

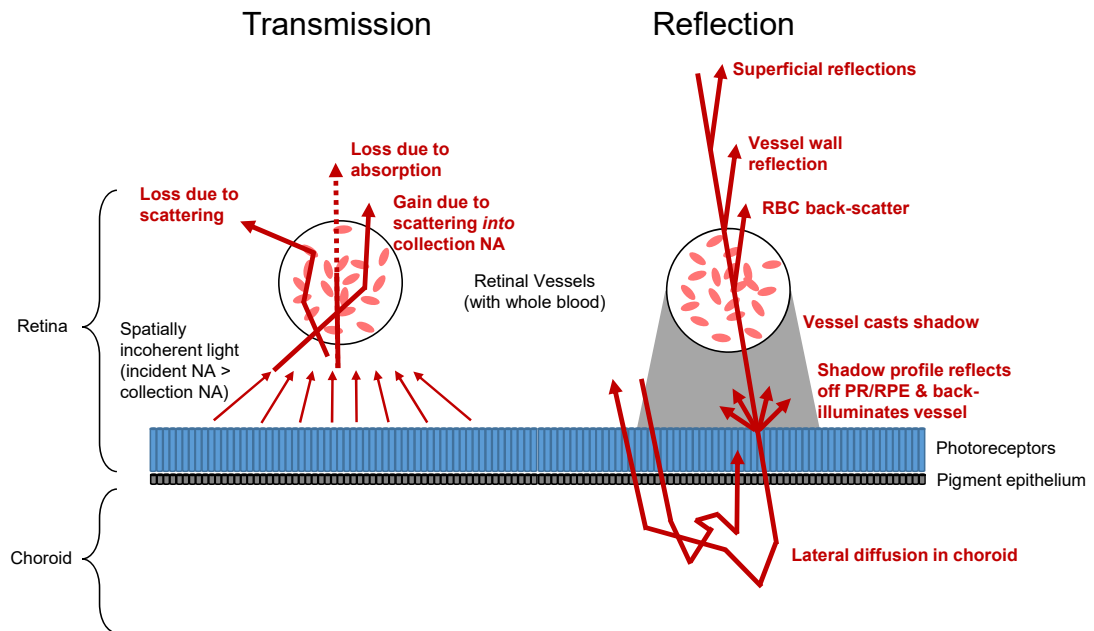


**Figure 3·1:** Hypothetical light paths for transmission and reflection imaging in the vicinity of a vessel (oriented perpendicular to the page). In transmission, the vessel is diffusely trans-illuminated and virtually all the collected light as pass through the vessel once. In reflection, the collected light is a combination of light paths that may have traversed the vessel once, twice, or not at all. Additionally, the shadowing effect increases the apparent vessel width.



choroidal vasculature might be easier to visualize because it must only pass the highly scattering and absorbing RPE layer once.

In this chapter we will present the first quantitative comparison between conventional reflection and transcranial transmission fundus imaging. Our strategy is to control as many parameters as possible, thereby isolating effect of illumination geometry. We have modified our fundus camera to provide quasi-simultaneous reflection and transmission imaging channels. Parts of the chapter have been presented at the 2019 ARVO Annual Meeting (Weber and Mertz, 2019a; Weber and Mertz, 2019b).

## 3.2 Methods

### 3.2.1 Fundus camera modifications

We modified the fundus camera used in Chapter 2 to couple light from a separate 850 nm LED into the normal illumination pathway for the fundus camera. We replaced the original flash tube with the distal end of an additional flexible fiber bundle. LED light was coupled into the bundle with another 3D-printed LED light collector (as seen in Fig. 2.8). The transcranial transmission imaging was performed the same as in Chapter 2.

To achieve quasi-simultaneous reflection and transmission imaging, we temporally-multiplexed (i.e. strobed) the separate reflection and transmission LED channels. With a custom Arduino microcontroller program, we synchronized the strobing LED channels with a free-running sCMOS camera (Andor Xyla), thereby achieving quasi-simultaneous transmission and reflection imaging.

To even non-uniform illumination, in post-processing we divided both transmission and reflection images by a fitted 3<sup>rd</sup> polynomial function of itself, avoiding the area around the optic disc.

### 3.2.2 Vessel fitting

To quantify vessel diameters and extinction, we manually traced several retinal vessels. From those paths, we interpolated several consecutive perpendicular line profiles, so as to straighten the vessel and its surrounding along a linear path (see Fig. 3.4 for an example). We fit the straightened 2D areas to a cylindrical vessel model. A 2D fit was preferred over a single 1D cross sectional line, as it reduces the influence of background inhomogeneities. Vessels are straightened along their path and fit to the following nonlinear model in MATLAB.

$$I_{\text{measure}}(x, y) = N(x, y) \exp(-\mu_e L(x)) \quad (3.1)$$

$N(x, y)$  is a polynomial describing the illumination gradient,  $\mu_e$  is the extinction coefficient, and

$$L(x) = 2\sqrt{r^2 - (x - x_0)^2} \quad (3.2)$$

is the path length through the vessel. The model estimates  $\mu_e$ ,  $r$ , and polynomial coefficients in  $N(x, y)$ .

## 3.3 Results

### 3.3.1 Simultaneous transmission and reflection fundus imaging

We were able to simultaneously acquire reflection and transmission images. A wide-field (45° FOV) is provided in Figure 3.2. The most obvious difference is the appearance of the optic disc which, in transmission appears bright, nearly saturating the image. We did not notice an increase in clarity of the major choroidal vessels, when using transmission.

In Figure 3.3, we show an higher magnification view (20° FOV), which clearly depicts the different appearance of retinal vessels. We also plot cross sectional line

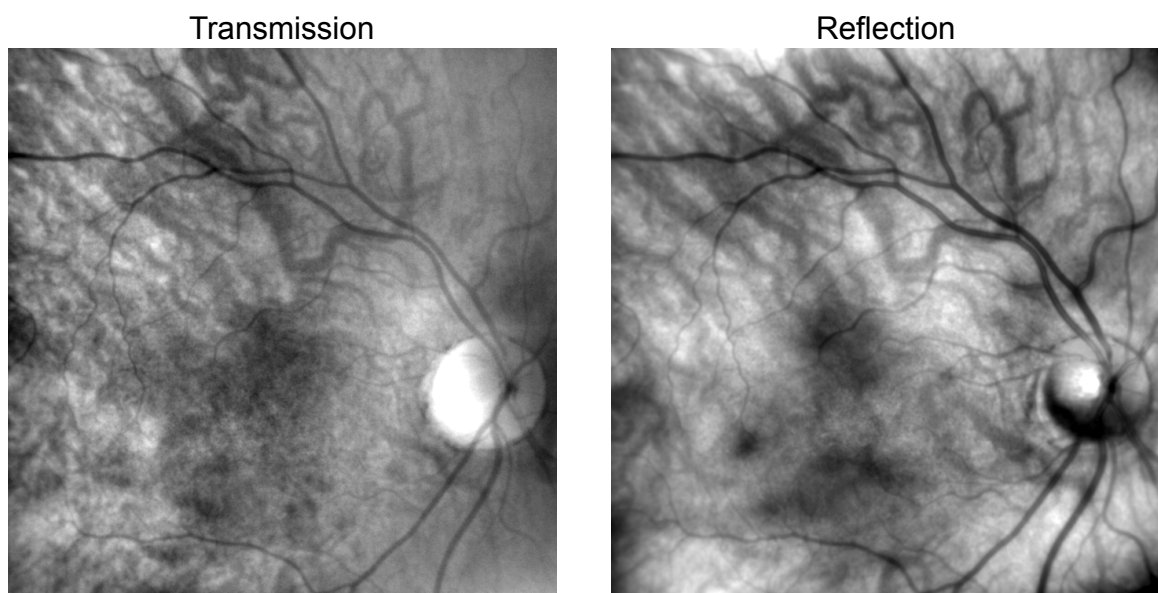


**Figure 3·2:** Quasi-simultaneous transmission and reflection fundus imaging results at 850 nm. In transmission, the optic is bright, due to the absence of posterior pigment epithelium. In reflection, large vessels exhibit central reflex and are slightly wider than the same vessels seen in transmission. Nonuniform illumination has been corrected with 3<sup>rd</sup> order polynomial fit.

profiles through the vessels. As expected a prominent central vessel reflex appears in the reflection image. The retinal vessels also appear slightly wider in the reflection image.

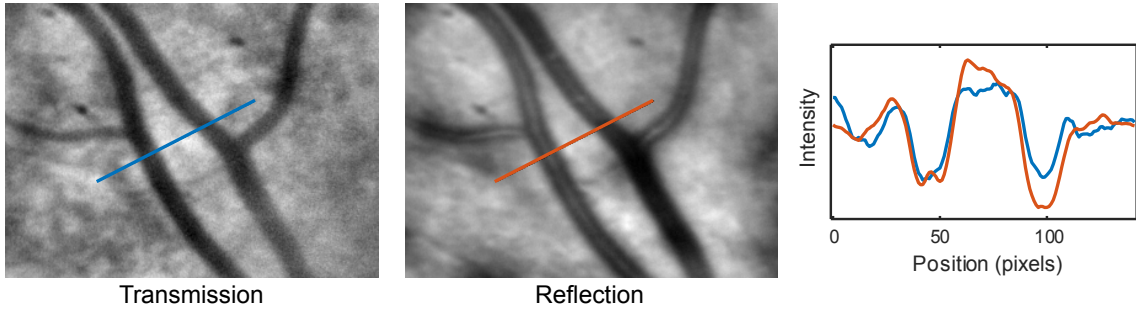


**Figure 3-3:** Quasi-simultaneous transmission and reflection imaging of retinal vessels. (Left and center) Higher magnification images of vessels at 780 nm. (Right) Cross sectional profiles through indicated lines. A small reflex is apparent in the reflection image corresponding to an artery. No apparent reflex was observed in the paired vein. Nonuniform illumination has been corrected with 3rd order polynomial fit.

### 3.3.2 Vessel fitting

In Figure 3-4, we show two examples of vessel stretches that has been straightened (by interpolating consecutive lines perpendicular to the vessel path), and fit to the model provided by Equations 3.1 and 3.2. The estimated radius,  $r$  and extinction coefficient,  $\mu_e$  are provided along with a visualization of the model fit, which confirms fit validity. We also show the fit residual map (the straightened data minus the model) in the right column. The original vessel is hardly visible in the residual indication that the model has adequately accounted for the vessel attenuation.

For each of the major retinal vessels we have performed the 2D model fit on straightened data. The results are shown in Figure 3-5. The estimated vessel radius is consistently larger in the reflection image. There was no such clear relationship for the extinction coefficient.

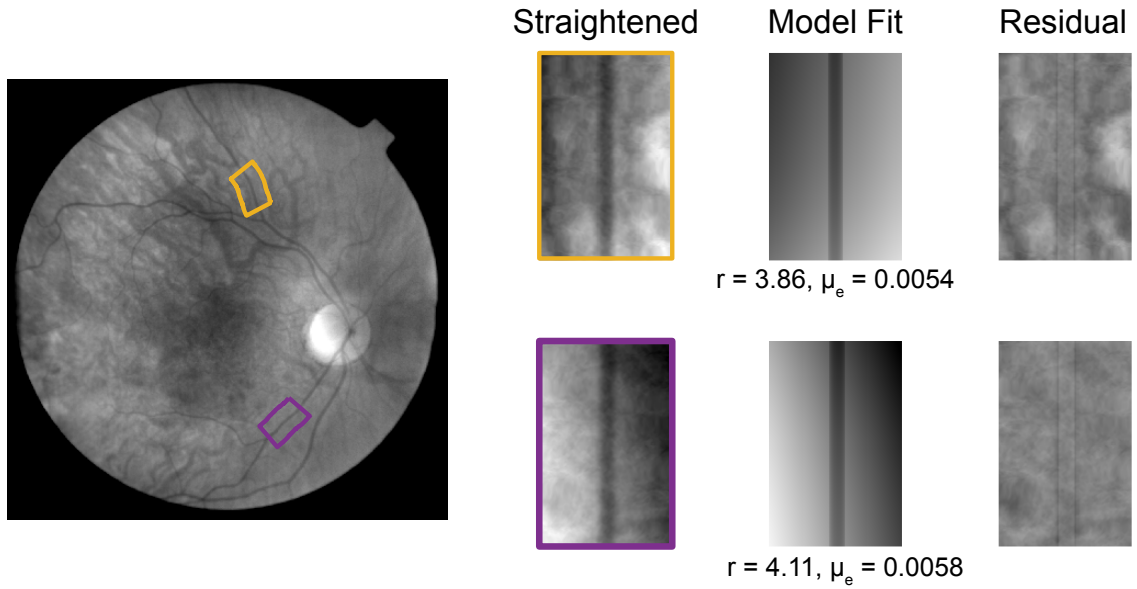


**Figure 3-4:** Fitting the 2D model of a retinal vessel to straightened segments extracted from image data. (Left) Flattened transmission image indicating vessel fitting locations. (Right) The straightened vessel segment, model fits and parameter estimates (units: pixels and pixels<sup>-1</sup> for  $r$  and  $\mu_e$ , respectively), and fit residuals.

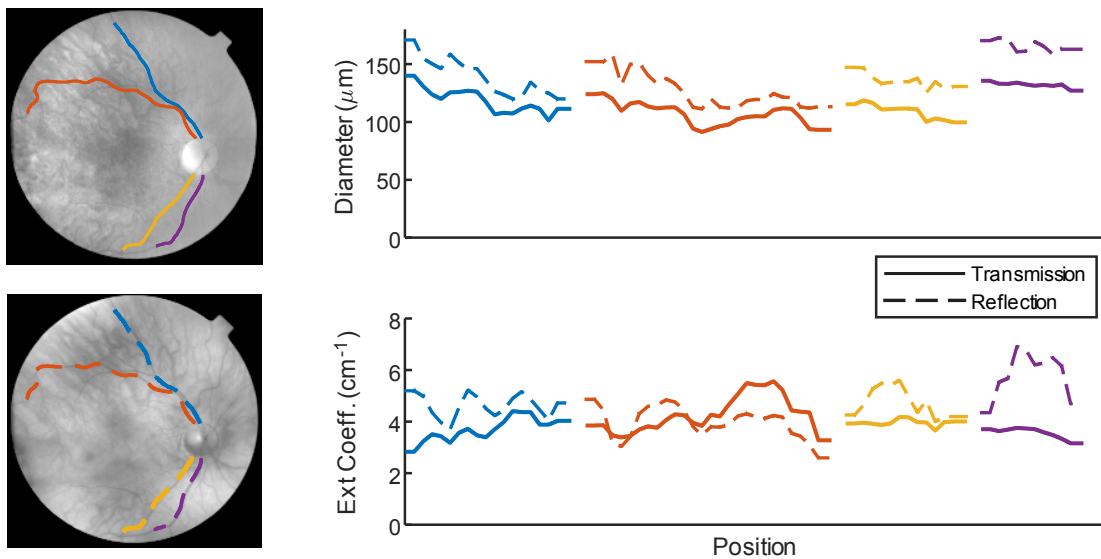


**Figure 3-5:** Vessel model fitting results across extended lengths of retinal vessels. (Left, top) Flattened transmission image. (Left, bottom) Flattened reflection image. Right: Vessel model parameter fit results for diameter and extinction coefficient ( $\mu_e$ ).

### 3.4 Discussion

This chapter presented a preliminary quantitative comparison between the transcranial transmission and convention reflection-mode fundus imaging. We isolated the effect of illumination geometry (i.e. reflection or transmission) by performing quasi-simultaneous transmission and reflection imaging with a modified fundus camera.

Contrary to our hypothesis, the transmission image did not show enhanced visibility of choroidal vessels compared to reflection. In fact, the reflection geometry may even provide better choroidal contrast. A possible explanation for this is that in reflection, a significant portion of the light double passes the choroid and reflects off the sclera.

The vessel fitting procedure easily fit the 2D straightened vessel stretches. In the residual images, the vessel was nearly eliminated, except faintly towards the edges (see Fig. 3-4), possibly due to unaccounted diffractive blurring.

When fit to a basic attenuating vessel model, we consistently saw a higher estimated radius for the reflection images. Although this finding has not, to our knowledge, been explicitly stated in the literature, it could possibly be inferred from previous analysis on the effective point spread due to scattering in the fundus (Hodgkinson et al., 1994). We believe that the reflection images give an erroneously high estimation of vessel diameter because, as depicted in Figure 3-1, the incident light casts a shadow which expands as it reaches the RPE. The shadow on the RPE is slightly defocused when capturing the vessel image, causing an apparent increase in width.

## Chapter 4

# Retroillumination Microscopy

### 4.1 Introduction

#### 4.1.1 Significance

Non-invasive cellular-scale optical imaging of the cornea is a valuable tool for disease diagnostics, management, and monitoring. In clinical practice, it is often used to distinguish forms of infectious keratitis (i.e. amoebic, bacterial, fungal, viral, etc.) *in situ* when corneal biopsy is infeasible or culturing fails to yield a diagnosis (Vaddavalli et al., 2011). It is frequently used to examine the *in vivo* (or donor tissue) endothelium for evidence of structural change or dysfunction, which can cause corneal edema and concomitant vision impairment (McCarey et al., 2008; Tuft and Coster, 1990; Bourne, 2003). Cellular-scale corneal nerve imaging has also been suggested as a means to monitor systemic disease, such as diabetes mellitus, and recovery from refractive surgery or other wounds (Nitoda et al., 2012; Patel and McGhee, 2009).

In this chapter, we will confine our attention mainly to imaging techniques, however it is also worth mentioning that optical spectroscopy modalities, when applied to the anterior eye, have shown great promise, as well. Brillouin spectroscopy has been applied to image intact corneal mechanical properties, which are perturbed in ectatic diseases such as keratoconus (Scarcelli et al., 2012). There is also evidence that  $\beta$ -amyloid may be present in the cytosol of lens fibers of subjects with Alzheimer's disease (Goldstein et al., 2003), suggesting a potential role for the crystalline lens as a non-invasive biomarker for neurodegenerative diseases.

### 4.1.2 Evolution of existing clinical methods

Currently, the established microscopic clinical imaging methods are specular microscopy (SM) (Laing et al., 1979a; Laing et al., 1979b) and *in vivo* confocal microscopy (IVCM) (Guthoff et al., 2006).

#### Specular microscopy

The foundation for SM can be traced back to early work by Swiss ophthalmologist Alfred Vogt who observed that endothelial cell edges could be visualized with a very narrow beam generated by a slit lamp biomicroscope when focused on the interface between the cornea and aqueous humor (Vogt, 1920). Due to the slight difference in refractive index between the posterior endothelium and the backing aqueous humor, a reflection, largely confined to a thin plane (hence “specular”) is observed. This is also the interface responsible for the second Purkinje image (Schwiegerling, 2004). The edges of cells do not efficiently reflect incident light and therefore appear dark on a bright background.

The first specular microscope was introduced by Maurice in the 1960’s for laboratory studies of corneal endothelial function in enucleated rabbit eyes (Maurice, 1968). This was the first device to use part of the objective lens pupil for illumination and the remainder of the pupil for imaging. Thus, the incident beam and reflected beam are oppositely tilted relative to ocular axis/surface normal (see Fig. 4.1(A)). This modification reduced objective lens back reflections endemic to most reflection-mode microscopes and reduced the prominent glare originating at the air-cornea interface. The basic design was subsequently modified for clinical use by Laing, Sandstrom, and Leibowitz (Laing et al., 1975) and further modified by Bourne and Kaufman (Bourne and Kaufman, 1976). Today, specular microscopes are ubiquitous in ophthalmic clinics (Fig. 4.1(B)). Importantly, modern systems also include automatic endothelial



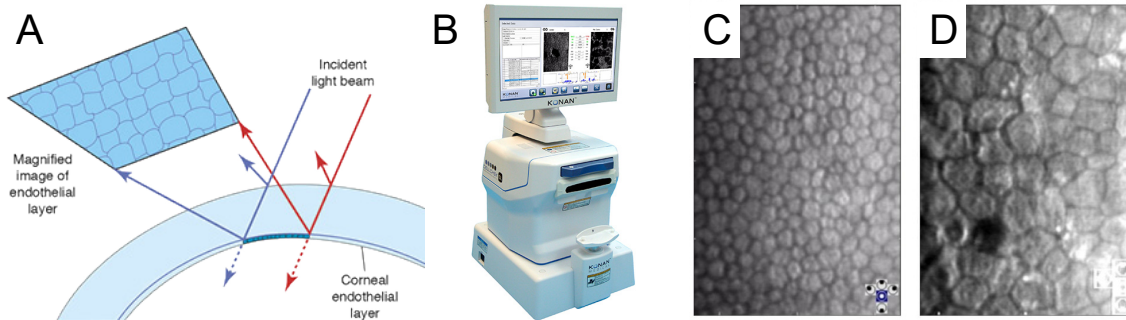


**Figure 4-1:** Specular microscopy concept and sample images. (A) Artistic depiction of specular reflection (Miller et al., 2005). A degree of optical sectioning occurs because the incident light beam and exit beam are oppositely tilted, avoiding strong reflection from the air-cornea interface, and also because the endothelium reflects more strongly than nearby stromal tissue. (B) Modern semi-automated clinical specular microscope (Konan CellChek SL). Sample images from (C) a healthy cornea and (D) a low cell density cornea with prominent gutta (black spot), likely an area of cell loss. Images (B)-(D) (Konan Medical, 2020).

cell counting and morphological analysis (McCarey et al., 2008), which helps distill image information for the clinician down to a couple important actionable metrics.

Nevertheless, SM has a few key limitations. First, it has a small field of view (FOV), limited to the width of the narrow illumination beam, and typically only about  $0.2 \times 0.5 \text{ mm}^2$ . For comparison, the corneal surface is about  $140 \text{ mm}^2$  (Dawson et al., 2011), hence it is possible to miss individual cell absences (called guttae, see Fig. 4-1(D)), even with multiple images. The presence of guttae is thought to represent endothelial stress. Second, the optical sectioning, while strong enough to visualize the bright specular endothelial reflection, is not strong enough to discriminate stromal backscattering from adjacent plane scattering. Reducing the slit beam width can improve sectioning strength, however doing so would drastically reduce FOV.

### **In vivo confocal microscopy**

The beginning of IVCM can be traced remarkable also to Maurice, who recognized the importance of reducing the slit width down to the order of the desired optical section depth (approx. 3  $\mu\text{m}$ ). To increase the field of view, he devised a method to translate the sample (enucleated rabbit cornea) and photographic recording film at precisely the same ratio of rates such that a highly-sectioned widefield was exposed sequentially across the film (Maurice, 1974). This was essentially a sample-scanned line confocal microscope, however sample scanning was not adaptable for *in vivo* clinical use (each frame took on the order of 1 min).

Later Koester introduced an oscillating polygonal mirror into the beam path of a similar system (see Fig. 4.2) and was able to capture images of approximately 0.5  $\text{mm}^2$  in area—a five-fold increase. The mirror simultaneously scanned a slit across the sample, descanned the backscattered beam through a stationary filtering slit, and finally rescanned the filtered beam across recording film, creating a composite image (Koester, 1980). The mirror oscillation rate was high enough (500 Hz) to permit direct viewing of the sectioned image. It was also capable of capturing *in vivo* images. However, optical sectioning was not as strong as in Maurice's system, because, in order to maintain sufficient signal, the slit width could not be reduced to any lower than 50  $\mu\text{m}$ .

In the early 1990's, Masters and Thaeer introduced a similar "flying slit" confocal system, which overcame previous signal strength issues (Masters and Thaeer, 1994). Their system featured a double-sided oscillating mirror, a high NA immersion objective, and an intensified video camera. The higher-NA objective improved signal collection efficiency and sectioning strength, while the intensified camera increased signal gain. They showed clear images of superficial, wing, and basal epithelial cells, corneal nerves, keratocyte nuclei, and endothelial cells. This design has been com-

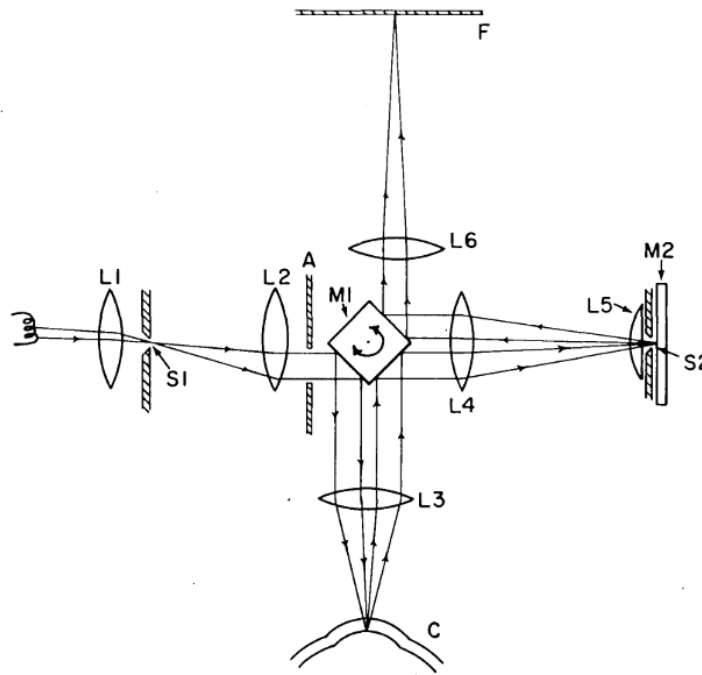


**Figure 4.2:** Koester's scanning mirror microscope. L1-6: lenses, S1: illumination slit, S2: detection slit, A: aperture, M1: oscillating mirror, M2: mirror, F: recording film, C: cornea. Reproduced from (Koester, 1980).

mercialized and is in use today (i.e the Nidek Confoscan series).

Although the speed of slit-scanning confocal is sufficient for *in vivo* use, it is only truly confocal in the axis perpendicular to the slit. Sectioning strength, and hence contrast, can be improved by adopting a point scanning approach. The first *in vivo* demonstration of this principle was by Cavanagh (Cavanagh et al., 1990), who used a parallel array of scanned points, rather than a single point due to speed and illumination efficiency concerns. This system was a modified version of Petr an's tandem scanning confocal microscope (TSCM) (Petr an et al., 1968).

True single point scanning confocal microscopy is typically achieved with a focused laser (LSCM) and has higher axial sectioning strength and stray light control. LSCM was first limited to the *ex vivo* cornea and crystalline lens (Masters and Paddock,

1990a; Masters and Paddock, 1990b; Masters, 1992), as the frame rate of most laser scanning confocal systems were initially too slow for *in vivo* use. However, with development of laser diodes and improved resonant scanning systems, this limitation was eventually overcome.

Rather than building their own 2D scanning system, Guthoff and colleagues at the University of Rostock adapted an existing cSLO (Webb et al., 1987) platform, the Heidelberg Retinal Tomographer series (HRT), into a fully fledged confocal corneal microscope (Stave et al., 2002). Compared to slit-scanning devices, the HRT equipped with the Rostock Cornea Module (RCM) provides the higher sectioning strength, which in turn improves contrast and image quality (Alkabes et al., 2007; Szaffik, 2007). The laser scanning confocal concept, a photograph of the HRT + RCM system, and sample images are given in Figure 4-3. The system can be equipped with a 670 nm diode laser and multiple options for the objective lens. The most common configuration is with a Zeiss 63X/0.95 NA water immersion objective lens. The developer lists a resolution is about 1-2  $\mu\text{m}$  (Stachs et al., 2019), which is much higher than the expected diffraction-limited resolution from a 0.95 NA objective. From this observation, and the published design of a typical cSLO (Webb et al., 1987), we can infer that the HRT-RCM must underfill the objective back aperture while using a large confocal pupil (large than the Airy disc size for the objective), possibly to increase signal strength. We note that the nearly 20-year-old HRT is now obsolete technology and the Rostock group appears to be actively developing a replacement module based on the popular Heidelberg Spectralis platform, a multimodal OCT and cSLO device (Stachs et al., 2017; Bohn et al., 2019).

Whereas SM is restricted to the endothelium, IVCN is able to produce high contrast images throughout the full thickness of the human cornea and resolve nerves and cells in 3D (Bohn et al., 2018). A caveat is that IVCN is usually performed

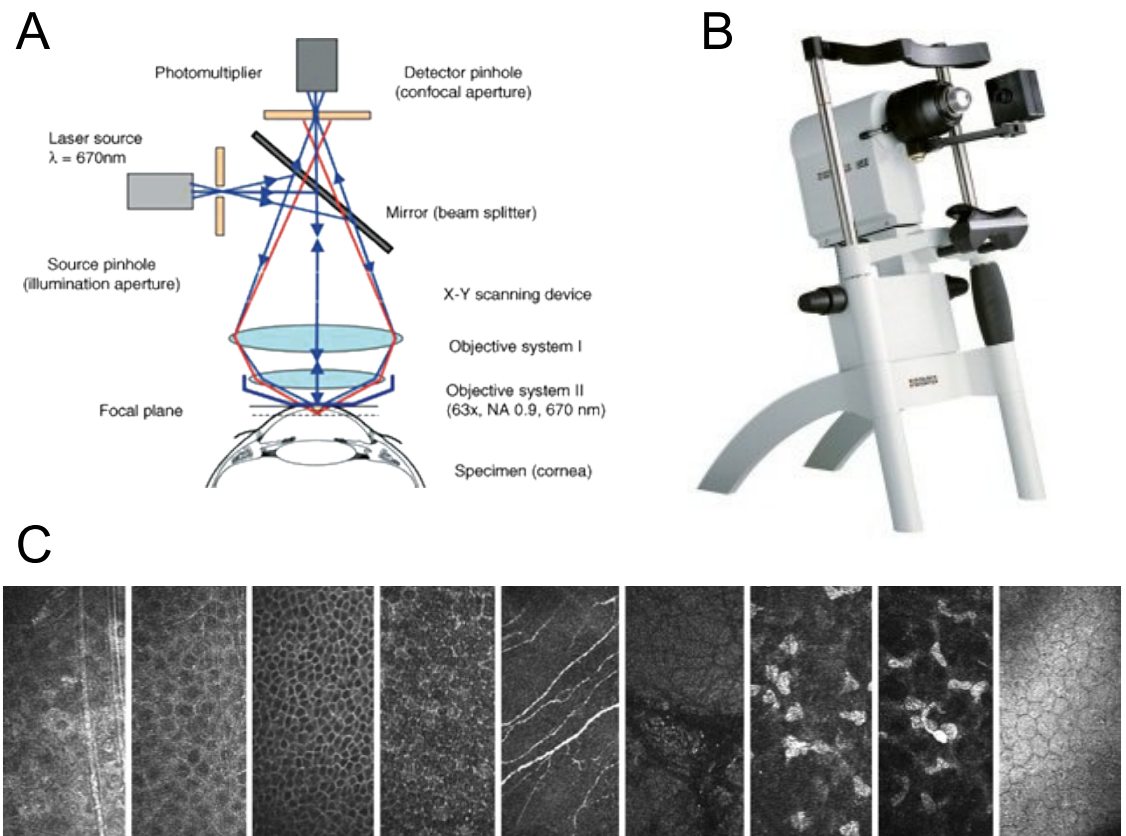


**Figure 4.3:** IVCN diagram and sample images. (A) Simplified beam paths for the HRT + RCM system. Objective system I is the lens used ordinarily for retinal examination. Objective system II is the RCM. Light from out-of-focus planes (red) is blocked by the pinhole before detection. (B) Image of the HRT + RCM. (C) Example images, from left to right: superficial epithelial cells, upper wing cells, lower wing cells, basal cells, subbasal nerves, Bowman's membrane, anterior stromal keratocytes, posterior stroma, endothelium. (A) & (C) Reproduced from (Guthoff et al., 2009).

in contact with the cornea, meaning the objective lens (or protective cap) touches the cornea during the examination. Topical anesthetic must be administered prior to imaging in order to avoid discomfort and reduce involuntary eye movements or blinks. With an experienced technician, contact operation is safe and straightforward. The dissertation author underwent contact IVCN and reports little discomfort. Neverthe-

less, there are many subjects with phobias that will not tolerate contact operation. Moreover, for routine screening purposes where speed is critical, non-contact methods are highly desired.

It should be mentioned that the Rostock group initially developed a non-contact module (Stave and Guthoff, 1998), but, lacking the mechanical coupling between the cornea and microscope, stability may have hindered further development. Hence, the non-contact module never made an impact on the clinical market. Others have developed non-contact systems recently (Pritchard et al., 2014; Pascolini et al., 2020), but these are not yet commercially available.

#### 4.1.3 OCT-based corneal microscopy

Much of the recent research in non-contact *in vivo* corneal imaging has involved various flavors of optical coherent tomography (OCT) (Huang et al., 1991; Fercher, 1996), largely due to its remarkable depth selectivity (i.e. optical sectioning). Multiple groups have applied ultra-high resolution OCT to *in vivo* corneal imaging (Bizheva et al., 2017; Werkmeister et al., 2017), however they provided no *en face* imagery. Chen et al. described a micro-OCT system capable of *en face* swine cornea imaging (Chen et al., 2017a). However, the A-line rate was not fast enough to provide useful *en face* images in the presence of normal tissue motion.

Mazlin and colleagues took a different approach and applied a parallelized full-field version of time-domain OCT (FF-OCT). They were able to acquire very large  $1.26 \times 1.26 \text{ mm}^2$  *en face* images in human corneas (Mazlin et al., 2018). With faster A-line rates, Tan et al. later showed high-resolution imaging in 3D was feasible with conventional raster-scanned spectral-domain OCT (Tan et al., 2018). Recently, Gabor-domain optical coherence microscopy (Rolland et al., 2010; Tankam et al., 2019) has also been successfully demonstrated *in vivo*, albeit only in anesthetized mice after careful motion correction (Canavesi et al., 2020). Similarly, ultra-high resolution

OCT has recently been demonstrated in primate cornea, but only after extensive motion suppression (Yao et al., 2019). Finally, recognizing that motion is a significant hindrance to raster-scanned OCT, Han and colleagues have returned to slit-scanning approaches (Han et al., 2019). Their system disperses the scanned slit out onto the area of an ultra-fast 2D areal image sensor.

#### 4.1.4 Fundus retroillumination

All of the techniques mentioned in this chapter so far have been based on reflection, or, more precisely, directly *backscattered* light from corneal microstructures. Here we introduce an *in vivo* microscopy technique based instead on transmitted light, which is sensitive to *forward-scattered* light. We call this approach asymmetric fundus retroillumination microscopy, or simply retroillumination microscopy, for short, in deference to the related but lower-resolution slit lamp technique (Brown, 1971). The key idea (shown graphically in Fig. 4-4) is to use the ocular fundus as a diffuse back-reflector, thereby folding the light path of a widefield transmission microscope into one which requires access to only one side of the sample (either the cornea or crystalline lens). To maximize back-reflection, we use near-infrared (NIR) light, which is weakly absorbed in the fundus and virtually undetectable to the subject. Additionally, we implement asymmetric illumination, a well-established method for enhancing intrinsic phase-gradient contrast (Kachar, 1985; Mehta and Sheppard, 2009; Ford et al., 2012). Our method is non-contact and produces images with high lateral resolution, comparable to state-of-the-art IVCN systems (1-2  $\mu\text{m}$ ), and across a large field in the cornea (1-mm diagonal). A strength of the system is its instrumental simplicity, making it a promising candidate for high-throughput disease screening or global-health applications.

The purpose of this chapter is to describe the retroillumination microscope design in detail. We also present representative images of the cornea and lens obtained

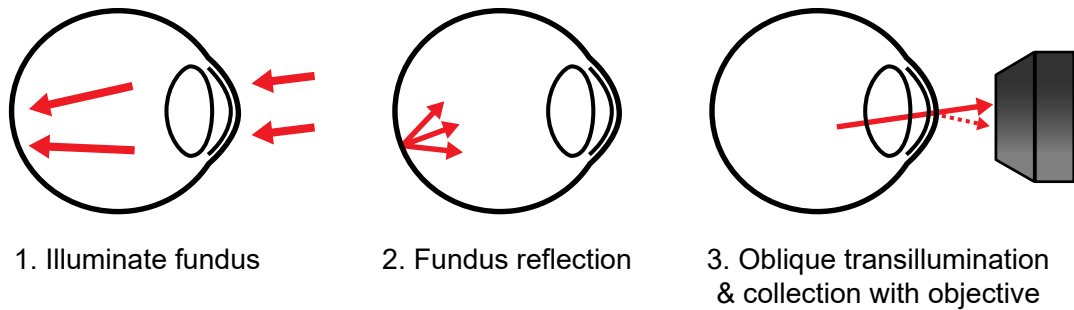


**Figure 4-4:** Asymmetric fundus retroillumination concept.

from healthy volunteer subjects. The basis for this chapter is a pending article, also available as a preprint (Weber and Mertz, 2020).

## 4.2 Device description

### 4.2.1 Hardware

A schematic for the retroillumination microscope is given in Figure 4-5 and cross-sectional illustrations of the illumination beam at the cornea and fundus are given in Figure 4-6. Additionally, a photograph of the system is provided in Figure 4-7.

### Subject interface

The subject is seated in front of the microscope in a dim room, allowing their pupils to dilate. The subject's head is placed on a chin rest, while their gaze is stabilized with a dim external fixation target. The microscope is mounted on motorized translation stages for alignment with the eye. Vertical adjustment is made with the chin rest. The flexible forehead strap has been replaced with more rigid supports in order to reduce motion.



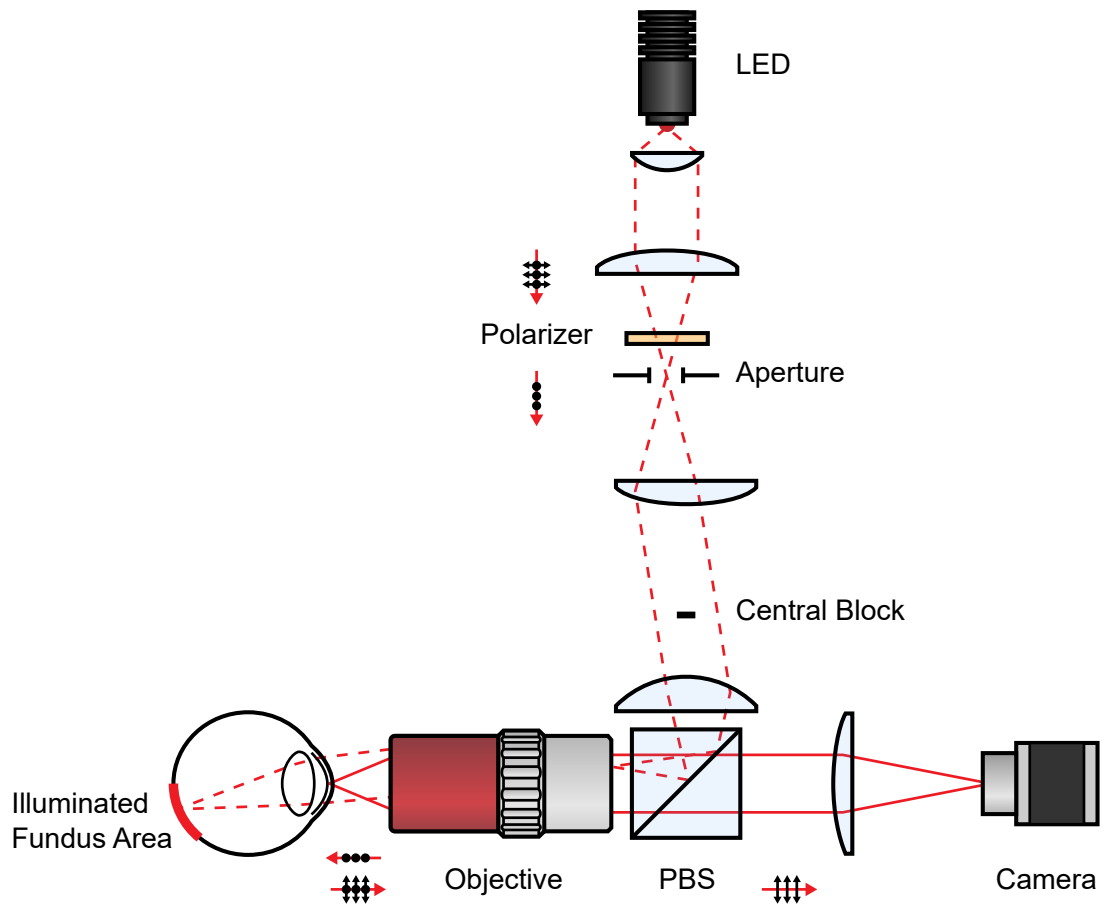


**Figure 4-5:** Retroillumination prototype system optical diagram. Dotted lines: illumination path, Solid lines: imaging (scattered) path. PBS: Polarizing beamsplitter

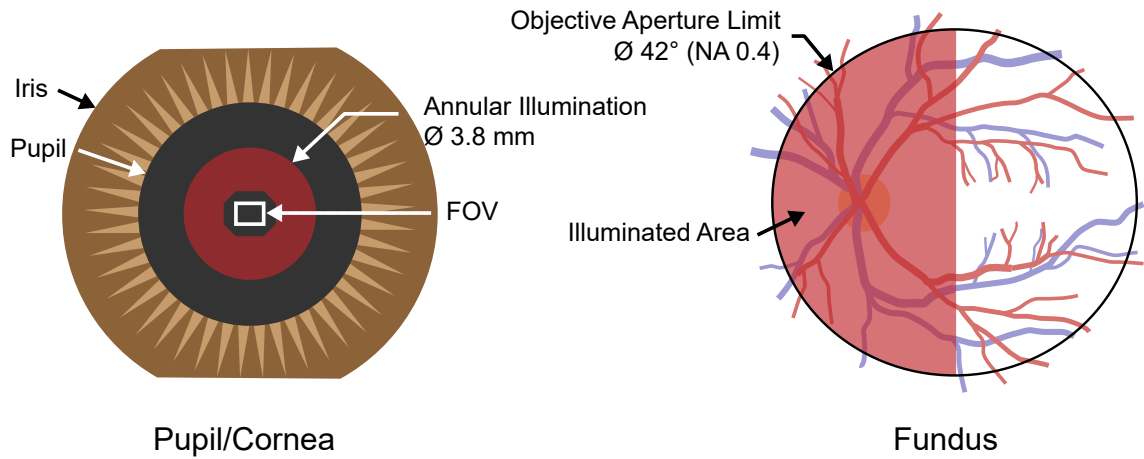


**Figure 4-6:** Illumination in cross-section at the pupil/cornea (left) and at the fundus (right).

### Illumination and fundus reflection

Illumination consists of a high power NIR LED (LZ1-10R602, Osram; 850 nm center wavelength), which is offset and magnified to span a semi-circular aperture and subsequently relayed through a polarizing beamsplitter (PBS; CCM1-PBS252, Thorlabs) cube to the back focal plane of a long working distance objective lens (MPlanApoNIR 20X / 0.4NA, Mitutoyo). The diameter of the aperture is adjusted such that its image half fills the objective's back aperture. The objective lens then projects the semi-circular LED image onto the fundus with a visual angle of about  $42^\circ$  (right side of Fig. 4-6). The beam diameter at the pupil is about 3.8 mm (Fig. 4-6, left), which should fit within the dilated iris of most subjects (Atchison and Smith, 2000). The objective lens working distance is 20 mm, which allows the subject to freely blink and maintain tear film.

We assume the fundus acts as a spatially-uniform diffuse reflector. Features such as retinal vessels and the optic nerve head exhibit rather weak contrast with NIR illumination (Weber and Mertz, 2018a) and hence their contrast can be ignored.

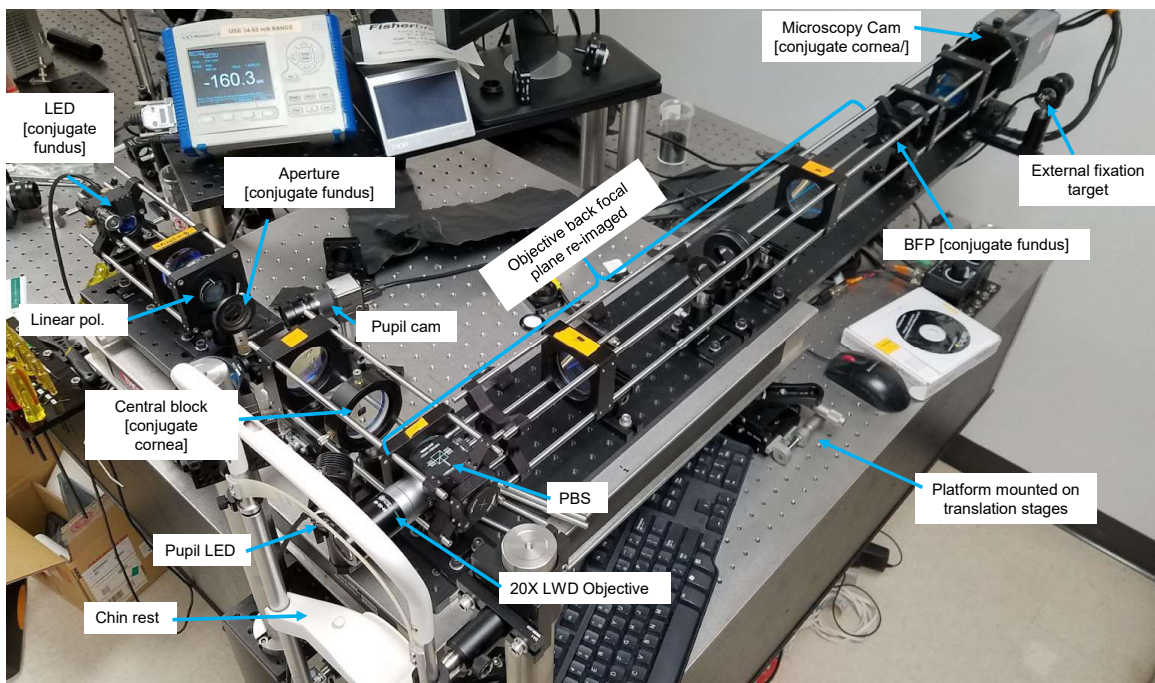


**Figure 4.7:** Photograph of the actual prototype retroillumination microscope and location of planes conjugate to planes depicted in Figure 4.6. The back focal plane re-imaging is to reduce the imaging NA for use in the crystalline lens, as in Section 4.4.5.

Multiple scattering in the fundus could cause the semi-circular area of the back-reflected light to broaden or laterally spread, however this is negligible (100-200  $\mu\text{m}$  for red (Hodgkinson et al., 1994)) compared to the overall size of the illuminated area. Lateral spreading should also help homogenize any LED image structure.

### **Microscope imaging path**

Reflected light from a confined semi-circular area on the fundus obliquely transilluminates (i.e. retroilluminates) the anterior segment. Rays clearing the iris are collected by the same objective and magnified with a compound tube lens onto the sensor of a machine vision camera (acA2000-340kmNIR, Basler), running at 348 frames/sec. We chose this speed based on speeds used successfully in corneal FF-OCT (Mazlin et al., 2018). We used two off-the-shelf achromats (AC508-300-B and AC508-150-B, Thorlabs) spaced by about 2 mm to achieve the desired tube lens power while avoiding additional aberration.

### **Back-reflection and stray light mitigation**

The system described thus far is susceptible to direct backreflections from the objective and to a lesser extent, the anterior segment interfaces, which can severely impair image contrast. To mitigate direct backreflections, we use cross-polarized detection and exploit the fact that multiple scattering in the fundus largely depolarizes the retro-scattered illumination. Specifically, the LED light is linearly polarized (LPVIS100-MP2, Thorlabs) and combined with a PBS cube.

In the illumination path, we also insert a small central block (mounted on a transparent window) conjugate to the cornea in order to darken the microscopy field of view (FOV) and reduce depolarized stray light. The block is responsible for the octagon-shaped hole in the incident illumination on the left in Figure 4.6. Although this configuration resembles an ophthalmoscope configuration, with its spatially seg-

mented input and output beams, we emphasize that the retroillumination microscope is focused on the anterior segment FOV, not the fundus.

### **Pupil location**

In practice, it is difficult to align the microscope to the eye using only the high-resolution FOV. We obtain a wider field for alignment by using an auxiliary camera to image the subject’s pupil with ambient light.

Specifically, a motorized flip mirror is inserted in the illumination path just after the aperture (omitted from Fig. 4.5 for clarity), which temporarily redirects an approximately 7 mm diameter low-resolution image of the pupil onto a free-running machine vision camera (DCC3240N equipped with camera lens MVL6WA, Thorlabs). We use the edges of the subject’s iris to then center the microscope prior to microscopic imaging. This alignment procedure increases operator repeatability. After locating the desired structures, we usually capture sets of 1024 frames—about a 3 sec video.

#### **4.2.2 Resolution and field of view**

In the asymmetric retroillumination microscope, and indeed all microscopes based on asymmetric illumination, the phase-to-intensity point spread function is no longer an Airy pattern, making it difficult to ascribe a resolution based on, for instance, the Rayleigh criterion. Instead we report spatial frequency bandwidth as a surrogate for resolution. For 850 nm light and 0.4 NA (illumination and imaging), the maximum spatial frequency is laterally  $940 \text{ mm}^{-1}$  (1.1  $\mu\text{m}$  period) and axially  $98 \text{ mm}^{-1}$  (10  $\mu\text{m}$  period), in air. In Appendix A, we display the lateral and axial frequency support graphically (specifically, see Fig. A.1). The camera produced images of dimensions 1540 x 1088 pixels. This corresponds to a field of view (FOV) of about 820 x 580  $\mu\text{m}$  (or 1 mm diagonal) in the cornea.

### 4.2.3 Light levels and safety

The total incident light power on the cornea is adjustable between 50-100 mW. This light level (at 850 nm) does not cause significant pupil contraction and is just barely visible to the subject. Crucially, because the power is distributed over large areas, the corneal and retinal irradiances are below the limits for non-hazardous Group 1 devices in the latest ophthalmic safety standard, the ANSI Z80.36-2016.

## 4.3 Image processing

Even with asymmetric retroillumination, intensity contrast at the image plane is low ( $< 5\%$ ). Two major sources of noise restrict useful post-hoc expansion of this range: photo response non-uniformity (PRNU) and shot noise. Note that offset noise is corrected on chip with correlated double sampling. Read and quantization noise are negligible. PRNU results from varying pixel gain and is easily corrected by dividing each raw frame by a calibration frame. We use a 256 frame average of uniform intensity, near the expected signal level, as the calibration frame.

Averaging several frames (equivalent to integrating more photons) reduces shot noise, but increases susceptibility to motion blur. Nevertheless, we could still average several frames by laterally registering frames prior to averaging. Registration was performed with standard FFT-based phase-correlation methods (Reddy and Chatterji, 1996). We found that we can usually average at least 9 frames before axial motion decorrelates the FOV. An example of the signal-to-noise ratio (SNR) improvement after averaging is given in Figure 4-8, where one half of the image is from a single frame and the other half is the result of a nine-frame rolling registered average.

Additionally, we remove any slowly-varying illumination gradients by dividing the image by a Gaussian-filtered version of itself ( $\sigma = 24$  pixels or  $13 \mu\text{m}$  in the cornea). Processing is performed efficiently in a consumer GPU (with MATLAB

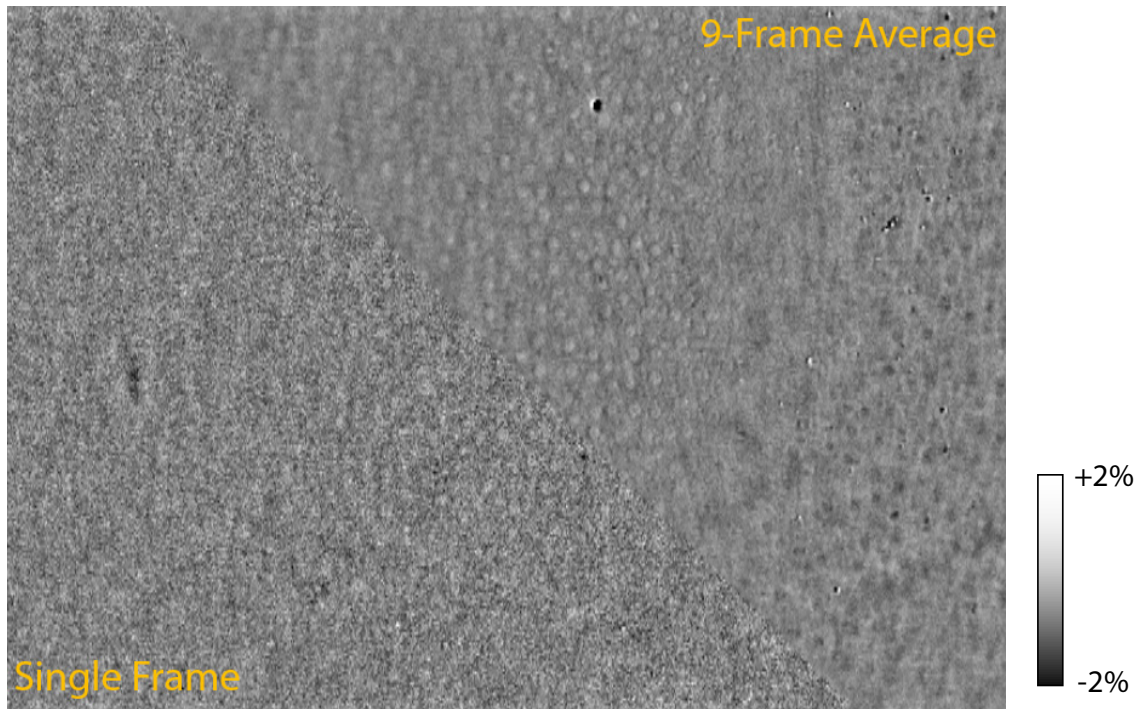


**Figure 4-8:** SNR enhancement after frame averaging at the endothelial cell layer, one of the lowest contrast layers examined.

built-in commands) and a cropped version of the images is displayed in real time at approximately 20 Hz. Following acquisition, we perform the same processing on the full FOV and for each frame in the stack.

## 4.4 Example images

### 4.4.1 Subjects

We imaged the left eye of 3 healthy volunteers ranging in age from 26 to 57 and with varying fundus pigmentation. For each subject, informed consent was obtained prior to imaging. The research was approved by the Boston University Institutional Review Board and conformed to the principles stated in the Declaration of Helsinki.

#### 4.4.2 Epithelium

The subbasal nerve plexus (SBP) was the most visible structure observed in the epithelium. The SBP is a highly-branched network of sensory nerve fibers located in a narrow plane between the basal epithelial cell layer and Bowman's layer. Figure 4.9(A) shows the SBP across nearly the entire FOV in the central cornea of a 28-year-old male. The large dark spots are out-of-focus aggregates of either mucin or shedded epithelial cell debris on the superficial cornea, anterior to the focal plane. These spots appear dark because the aggregates scatter light outside the collection aperture resulting in a decrease in local image intensity. The aggregates usually shift over time and move rapidly following a blink.

Enlarged areas are given in Figure 4.9(B) & (C) showing the complex SBP branching and variation of fiber diameter. We also repeatedly saw globular structures (yellow arrows) near or just anterior to the SBP plane of focus. These structures are more discernible in video. They may be Langerhans cells (resident macrophages) or intraepithelial nerve branches, but not nerve terminals since these are too small to discern with light microscopy (Marfurt et al., 2010).

Other periepithelial features are shown in Figure 4.10. The tear layer has a punctate appearance (Fig. 4.10(A)) with sparse highly-scattering aggregates. The edges of squamous and wing epithelial cells are occasionally visible (Fig. 4.10(B)), but have low contrast and are therefore difficult to distinguish. The basal epithelial cell mosaic (Fig. 4.10(C)) is always visible with positive or negative contrast depending on the relative position in the focal plane. In one subject, we saw numerous dendritic cells with clearly resolvable cell bodies and processes (Fig. 4.10(D)). We were unable to detect any discernible features in Bowman's layer.



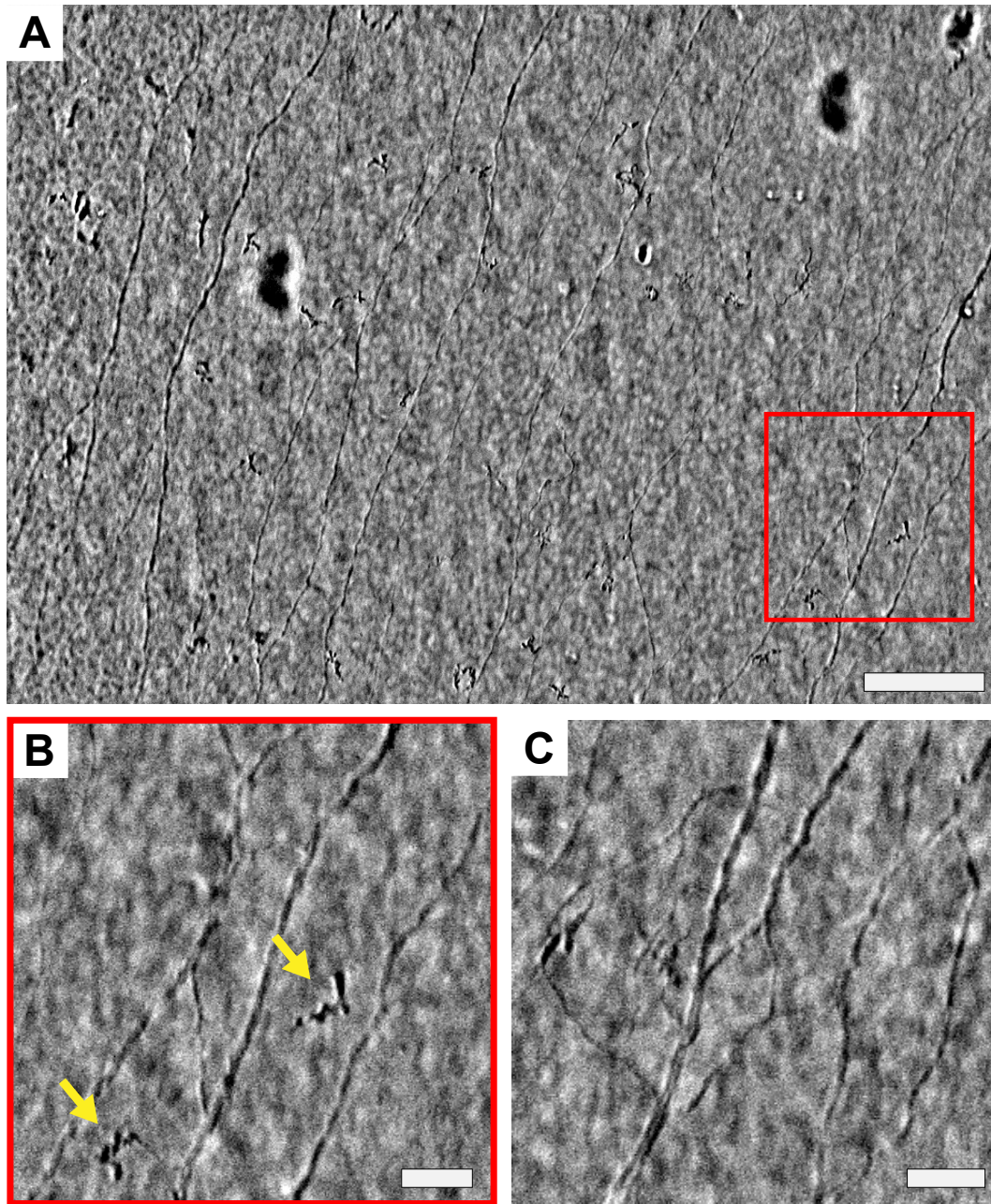


**Figure 4-9:** Subbasal nerve plexus of a 28-year-old male near the corneal apex visualized with retroillumination microscopy. (A) Full FOV (820 x 580  $\mu\text{m}$ ) and (B) indicated area in detail. Arrows indicate suspected Langerhans cells or intraepithelial fibers. (C) Another area seen later in the image sequence showing complex anastomoses. Scale bars: (A) 100  $\mu\text{m}$ , (B) & (C) 25  $\mu\text{m}$ .

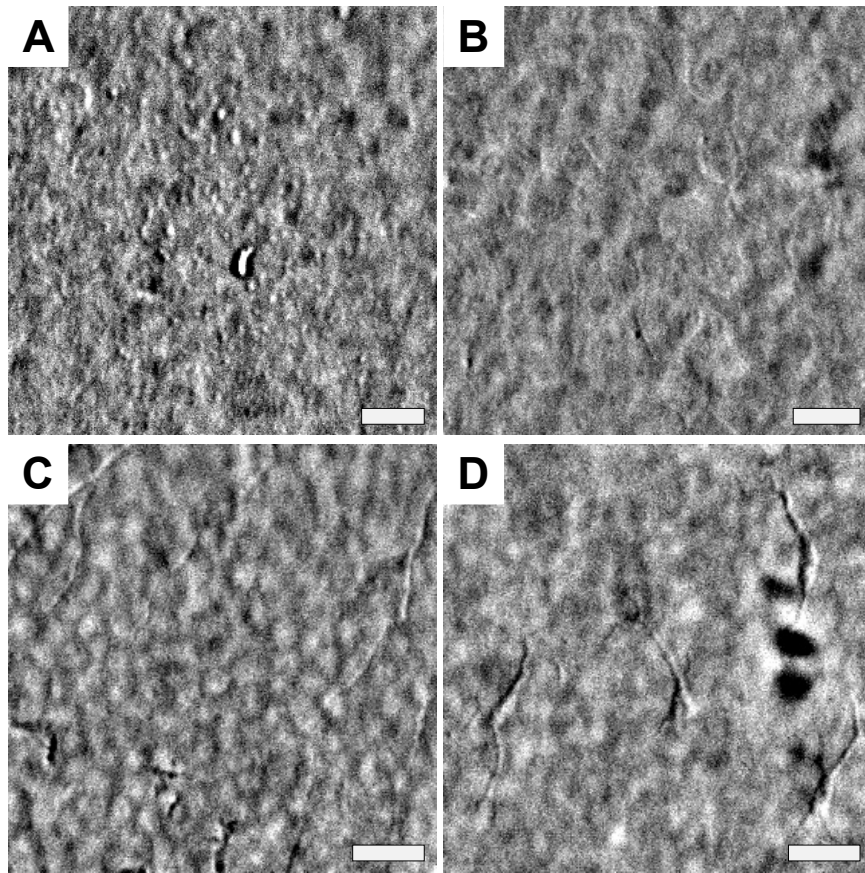


**Figure 4.10:** Other periepithelial structures visualized with retroillumination microscopy. (A) The tear layer of a 26-year-old female. (B) Superficial and (C) basal epithelial cells in a 28-year-old male. (D) Dendritic immune cells in a 57-year-old male. Scale bars: 25 $\mu$ m.

### 4.4.3 Stroma

Within the stroma, we observed large branching nerves. In contrast to subbasal nerves which are largely confined to a plane, stromal nerves are distributed throughout the anterior two thirds of the stromal volume. Hence, it was challenging to obtain images where large portions of the nerve were in focus. Figure 4-11 shows a few stromal nerve segments. Panels A and B are cropped views of the same stromal nerve trunk but at slightly different focal planes. Arrows indicate the common branch point.

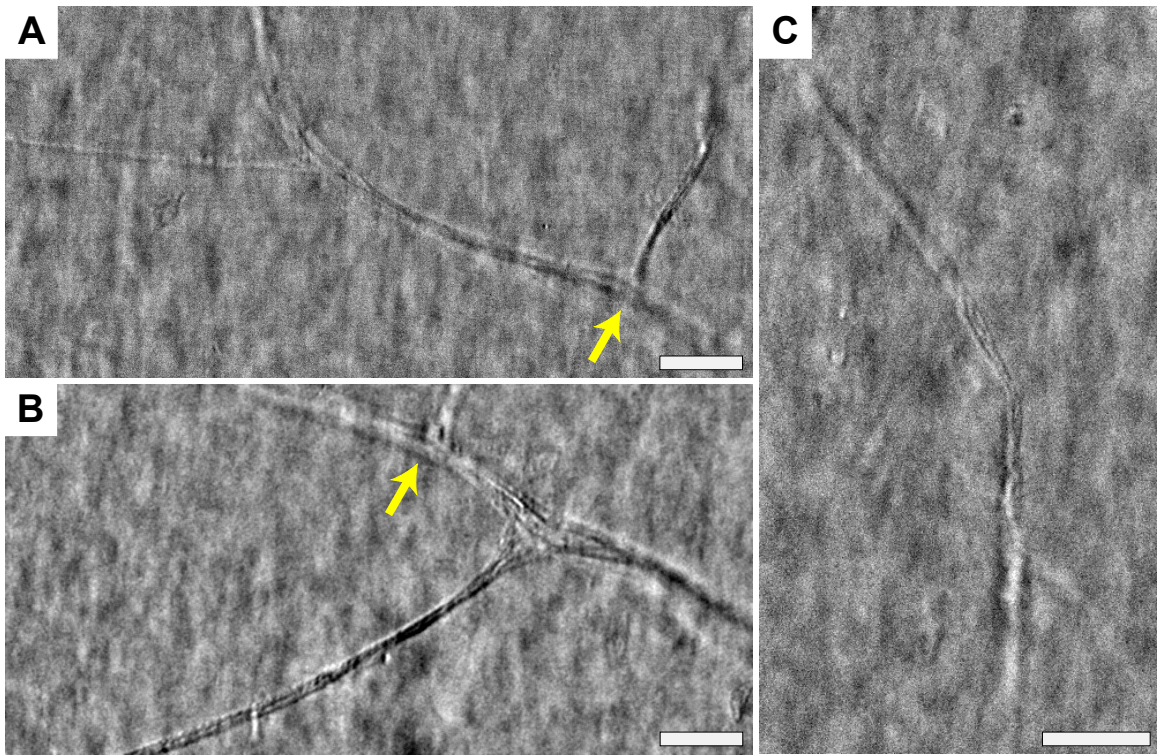


**Figure 4-11:** Large stromal nerves in a 28-year-old male. (A) Stromal nerve segment just anterior to view shown in (B). Arrows indicate the same branch point. (C) Stromal nerve in focus near the center and out of focus at the top and bottom. Scale bars: 50  $\mu\text{m}$ .

Keratocyte nuclei were notably absent from our retroillumination images. This was surprising based on their density in the stroma and high contrast in IVCM (Guthoff et al., 2006). In video sequences, we occasionally observed distinct struc-

tures about the size of a cell, but in much lower abundance than expected for normal keratocytes. We also did not see any indication of the subepithelial nerve plexus (SEP), however we confined most of our imaging to the central cornea where the SEP may simply be absent. Other authors have described this plexus as patchy (Marfurt et al., 2010).

#### 4.4.4 Endothelium

The endothelium, a monolayer of cells that coats the posterior surface of the cornea, was readily visible with retroillumination microscopy. A widefield 1 mm diameter view is shown in Figure 4-12. Interestingly, it appears that endothelial cell nuclei, and not cell edges, exhibit the best contrast (see Fig. 4-13 for detailed view). Similar to basal epithelial cells, when endothelial cell nuclei are above (i.e. anterior to) the focal plane, they produce positive contrast and conversely, when they are below the focal plane, they produce negative contrast. The curvature of the endothelium is also evident in Figure 4-12. Just anterior the endothelium, at the approximate location of Deschemet's membrane, we also repeatedly saw small high contrast (hyper-diffractive) spots. These spots were much smaller than the size of the nearby endothelial cells.

#### 4.4.5 Crystalline lens

With a 20 mm working distance objective lens we can easily adjust the system to focus on the crystalline lens, which begins about 3.3 mm behind the air-cornea interface. However, ray tracing software indicated that strong spherical aberration, from the air-cornea refractive index mismatch, impedes clear imaging. To reduce sensitivity to spherical aberration, we lowered the effective imaging NA by relaying the objective's back focal plane to an external iris prior to focusing on the camera. Passage through the iris reduced the imaging NA down to 0.2. Despite the lower resolution, both the lens epithelium and anterior lens fibers were discernible. Example images from a

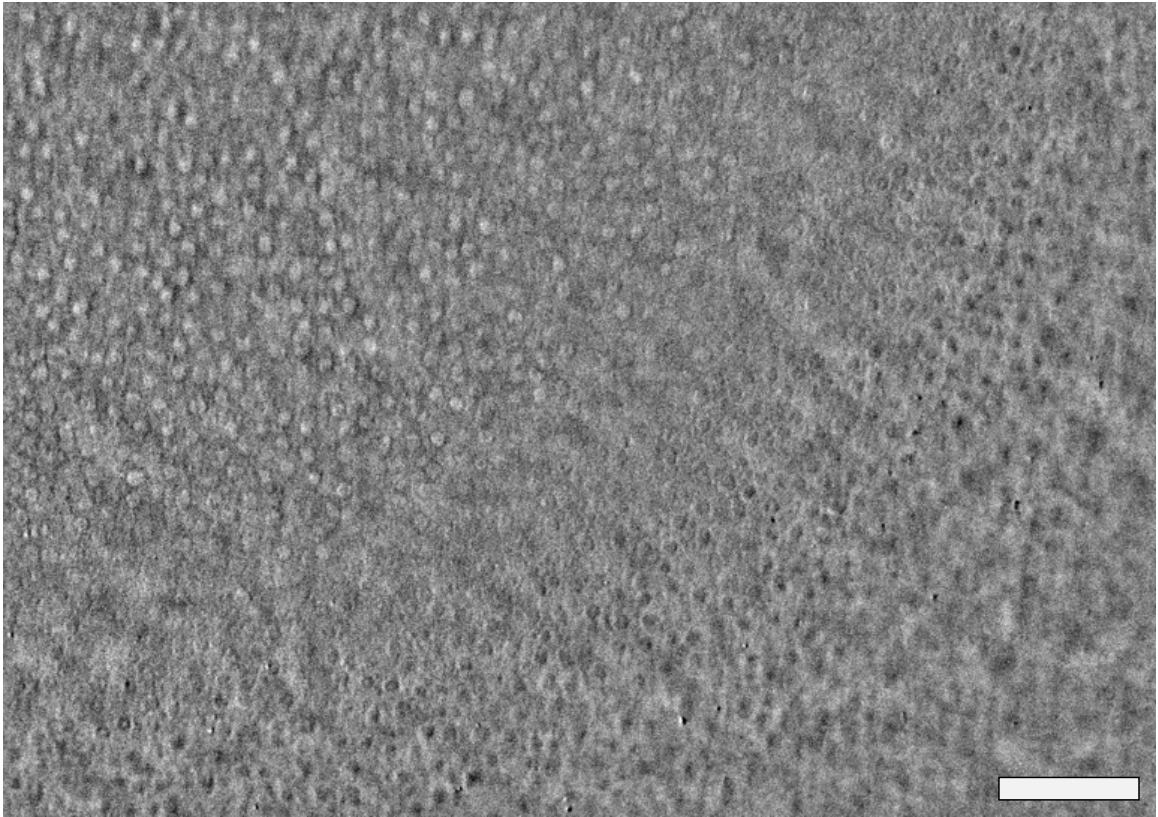


**Figure 4-12:** Wide field of view of the endothelium in a 26-year-old female. Bright/dark circles are nuclei anterior or posterior the focal plane. The curved zone of null contrast suggests that the corneal apex is located near the top left corner of the image. Scale bar: 100  $\mu\text{m}$ .

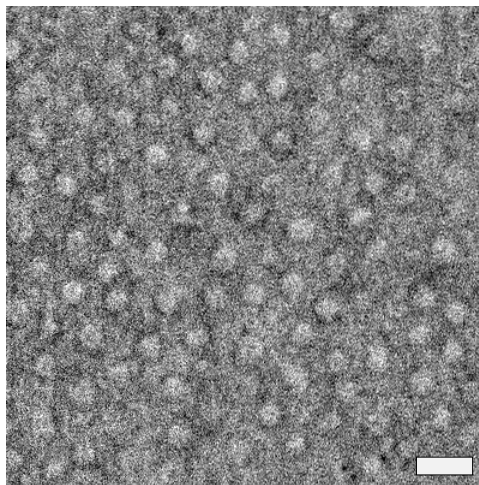


**Figure 4-13:** Cropped view of endothelium near the corneal apex of a 26-year old female. Scale bar: 25  $\mu\text{m}$ .

28-year-old male are shown in Figure 4.14.

## 4.5 Subbasal nerve plexus density

The density of the subbasal nerve plexus is an emerging biomarker for various ocular, as well as systemic diseases (Patel and McGhee, 2009; Cruzat et al., 2010). It is usually given in units of total nerve length visible in an image frame per area. We applied NeuronJ (Meijering et al., 2004), a semi-automated neuron tracing plugin to ImageJ (Schneider et al., 2012) to aid in nerve length measurement. Although the tool was developed for bright or dark neurites, such as those seen with fluorescent or dye labeling, we found that the plugin also readily worked on our phase gradient contrast images, in spite of dark tear aggregate artifacts. The program typically traced along the bright edge of the gradient.

An annotated image is shown in Figure 4.15. The total measured length is 8.5 mm. With the area of the image,  $0.48 \text{ mm}^2$ , we compute a density of  $18 \text{ mm/mm}^2$ .

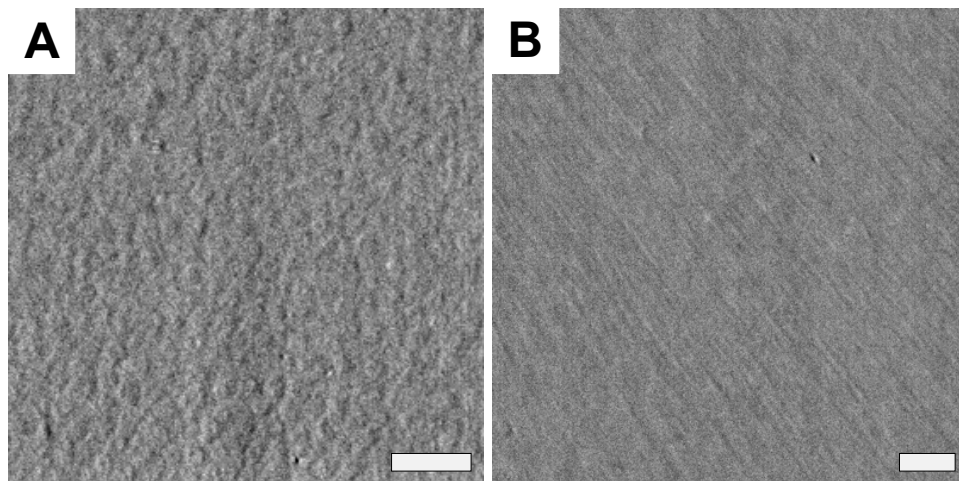


**Figure 4.14:** Crystalline lens (A) epithelium and (B) anterior fibers just below the epithelium. Scale bars  $50 \mu\text{m}$ .

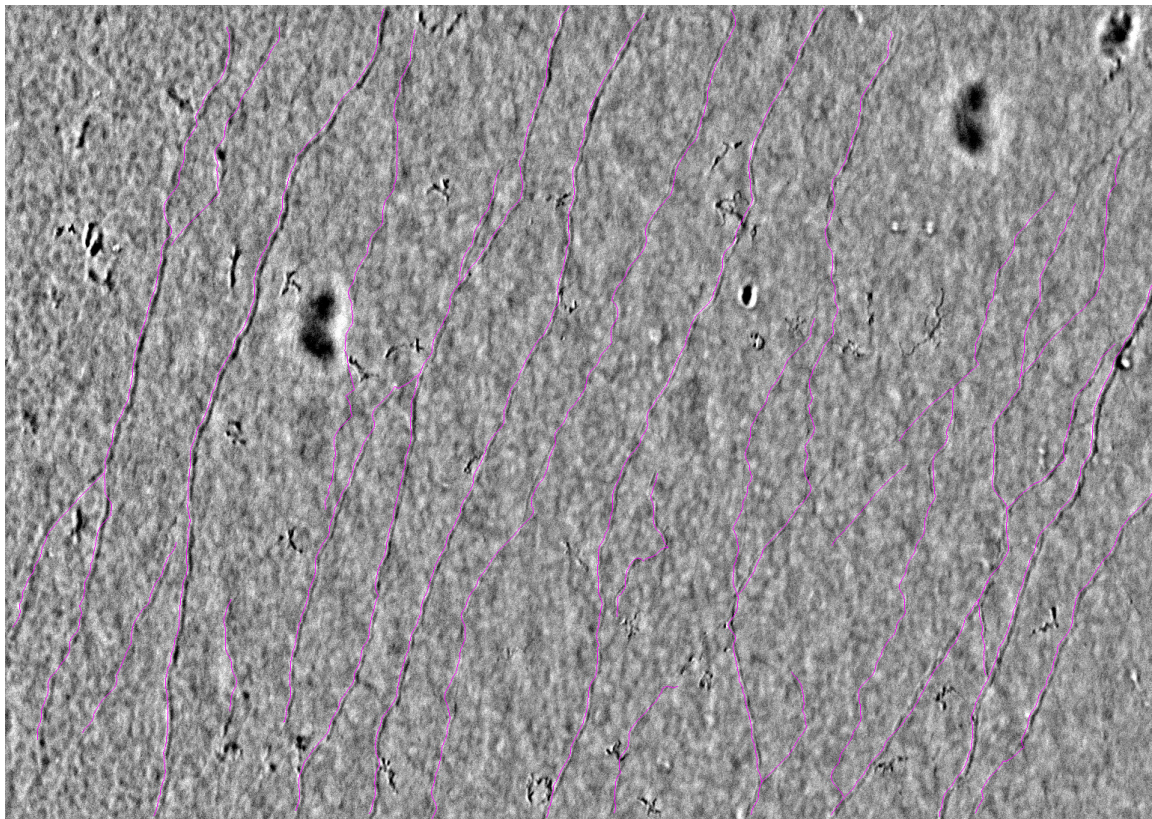


**Figure 4-15:** Results of semi-automated nerve tracing on widefield SBP image shown in Figure 4-9.

## 4.6 Endothelium through-focus

As mentioned in Section 4.4.4, endothelial cell nuclei exhibit positive contrast when anterior to the focal plane and negative contrast when posterior. To examine this effect in more detail, we stabilized the video sequence corresponding to Figure 4-12, with StackReg (Thevenaz et al., 1998), a free plugin to ImageJ (Schneider et al., 2012). From the stabilized stack, we selected several representative frames to show the contrast inversion (see Fig. 4-16).

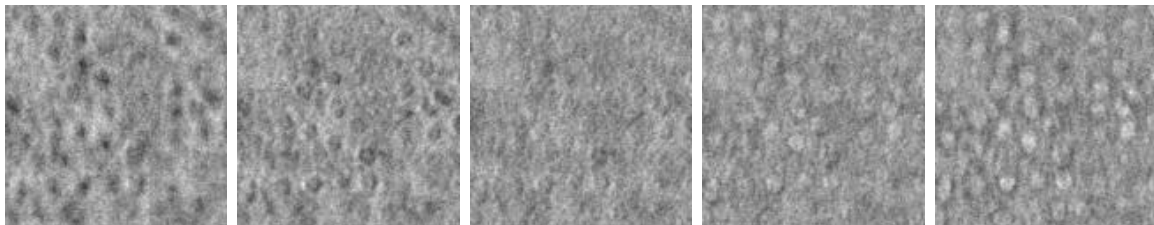


**Figure 4-16:** Inversion of contrast in endothelium seen in video corresponding to Figure 4-12. Left side shows cells located posterior to the microscope focal plane; right side, anterior. The middle frame is presumably in focus.

## 4.7 Discussion

We have described a new *in vivo* corneal and lenticular imaging method, which we call retroillumination microscopy. The technique is non-contact and produces images with high lateral resolution (1-2  $\mu\text{m}$ ), comparable to state-of-the-art IVCN.

### 4.7.1 Transmission vs. reflection imaging

Unlike most other *in vivo* eye imaging techniques, retroillumination microscopy is based on transmitted light. This difference has a fundamental impact on obtainable image contrast (Fercher, 1996; Sentenac and Mertz, 2018). In order for light reflection, or more precisely, backscattering to occur, the sample must present an abrupt change in refractive index. This could either be an interface (specular reflection) or a clump of scattering structures each smaller than the wavelength of incident light (Rayleigh-like scattering). On the contrary, transmission microscopy is sensitive to forward-scattered light, such as that primarily generated by larger structures, for example cell bodies or nuclei. A clear example is the different appearance of the corneal endothelium, which in reflection contrast usually appears as a hyper-reflective interface with dark paths delineating cell borders (Laing et al., 1975). In transmission contrast, it is the cell nuclei that are most apparent, while cell edges are undetectable (see Figs. 4-12 and 4-13).



As an aside, the adaptive optics ophthalmoscopy community has already recognized the utility of forward scattered light (Guevara-Torres et al., 2020) as a method to enhance contrast of blood flow (Chui et al., 2012), photoreceptor cone inner segments (Scoles et al., 2014), retinal ganglion cells (Rossi et al., 2017), and other cell bodies (Guevara-Torres et al., 2015). There are likely many other corneal features where transmission contrast can contribute complimentary information.

Transmission imaging also avoids superficial sample reflections, such as the prominent corneal anterior surface reflection. Excess background from this reflection can easily dominate intracorneal backscattering. Hence, high optical sectioning strength (e.g. confocal filtering or coherence gating) is normally required to diminish its effect, which in turn increases system complexity. In the absence of this reflection, we are able to form useful *en face* images across a large, 1-mm diagonal FOV with little more than a widefield microscope made of readily available off-the-shelf components. Instrumentation for this setup (Fig. 4.5) is extremely simple and many of the critical components leverage large existing markets (NIR LEDs and NIR-sensitive CMOS cameras for machine vision and surveillance, GPUs for gaming, etc), thus lowering costs. The overall low cost and simple optical design also makes retroillumination a possible candidate for global health applications.

#### 4.7.2 Comparison to slit lamp technique

Our method bears resemblance to the well-known slit lamp technique also known as retroillumination (Brown, 1971) (n.b. the naming similarity is intentional). Both techniques reflect light off posterior structures in order to back-illuminate the lens and cornea. However, unlike the slit lamp biomicroscope, which features separate, non-overlapping illumination and imaging paths, our system is designed around a single objective lens. With this configuration we are free to use a much higher collection angle (NA) in the imaging path without physically obstructing the illumination. Thus

our single lens configuration provides higher optical resolution than that obtainable with standard slit lamps. Similarly, our design enables unimpeded illumination of large fundus areas. We use this freedom to implement asymmetric illumination, a well-established method to enhance phase-gradient contrast (Kachar, 1985).

### 4.7.3 Single versus dual image

We note that many asymmetric illumination (or equivalently asymmetric detection (Hamilton and Sheppard, 1984; Mertz et al., 2014)) microscopy methods employ a dual image strategy (Mehta and Sheppard, 2009; Ford et al., 2012; Ford and Mertz, 2013; Mertz et al., 2014; Tian et al., 2014; Tian and Waller, 2015; Paudel et al., 2018), where two images, corresponding to opposite asymmetric illumination/detection are obtained and subtracted. This yields an image where the in-focus attenuation due to absorption is nullified. In our situation, the normal cornea presents very little absorption, so the dual image strategy serves no purpose.

### 4.7.4 Limitations

All of our corneal *in vivo* imagery was obtained from the central cornea, near the corneal apex. There are, however, important structures in the peripheral cornea that could have clinical utility. For instance, the limbus, the border between the cornea and sclera, contains radially-arrange fibrous protrusions called the palisades of Vogt, which are thought to harbor epithelial stem cells (Kruse, 1994). In the current configuration of the retroillumination microscope, peripheral corneal areas are inaccessible for imaging because the illumination beam would be blocked by the iris from reaching the retina. One possibility for adapting retroillumination to the peripheral cornea would be to use the iris, rather than the fundus, as the back-reflector.

In each of our three subjects, there was sufficient back-reflected light to form

corneal images. Predictably, in the subject with the highest fundus pigmentation, intensity was markedly reduced, in accordance with previous reports which showed about a three-fold difference in NIR reflectance between lightly and darkly pigmented fundi (Delori and Pflibsen, 1989). We mitigated SNR loss by increasing the illumination power, however this was only partly effective since the background also increased (up to nearly half the dynamic range of the camera). We could also average more frames, however axial motion limited the maximum number of frames to about 20. Additional averaging would require concurrent axial tracking, such as with a coaligned OCT beam (Bohn et al., 2019; Mazlin et al., 2020), and reconstruction of partial volumes.

Because this technique is widefield, the optical sectioning strength is modest. However, reduced optical sectioning appears to be tolerable, except perhaps near the anterior cornea where tear film aggregates cause dark spot artifacts (Fig. 4.9(A)). Since the spots were observed to move over time, it should be possible to remove them in post-processing.

#### 4.7.5 Corneal subbasal nerve density

Retroillumination provides excellent contrast of corneal nerves, particularly the subbasal plexus, which is recognized as a potential biomarker for ocular, as well as systemic diseases such as diabetic peripheral neuropathy (Misra et al., 2015; Pritchard et al., 2011) and rheumatoid arthritis (Villani et al., 2008). Combined with the large FOV (3X larger area than current IVCN) and non-contact operation, retroillumination microscopy may be a useful tool for monitoring diabetic neuropathy or other ocular diseases affecting corneal nerves.

Although this study reports only one density value (18 mm/mm<sup>2</sup>), this value appears to fall within a standard deviation (SD) from the mean of most recent laser scanning confocal microscopy (LSCM) studies on healthy populations. These studies

**Table 4.1:** Recent studies reporting central cornea subbasal nerve density in healthy populations. LSCM: Laser scanning confocal microscopy, SSCM: Slit scanning confocal microscopy, TSCM: Tandem scanning confocal microscopy, FF-OCT: Full-field OCT, RIM: Retroillumination Microscopy. \*This study used a montaged area from multiple individual confocal images. †This study selected the highest density image from multiple images each eye.

Study	Method	No. Eyes	Density (mm/mm <sup>2</sup> )	
			Mean	SD
(Oliveira-Soto and Efron, 2001)	SSCM	14	11.1	4.3
(Erie et al., 2005)	TSCM	65	8.4	2.0
(Patel and McGhee, 2005)	LSCM*	3	21.7	1.4
(Niederer et al., 2007b)	LSCM	30	21.6	6.0
(Niederer et al., 2007a)	LSCM	85	20.3	6.5
(Niederer et al., 2008)	LSCM	52	22.4	6.0
(Patel et al., 2009)	LSCM†	31	25.9	7.0
(Hertz et al., 2011)	LSCM	20	16.2	4.1
(Nitoda et al., 2012)	LSCM	47	16.6	4.2
(Parissi et al., 2013)	LSCM	207	19	4.3
(Mazlin et al., 2020)	FF-OCT	1	15	
<b>Current study</b>	RIM	1	18	

and others utilizing different technology are summarized in Table 4.1.

The technique used to obtain the image appears to have an impact. Earlier methods, such as slit scanning confocal microscopy (SSCM) and tandem scanning confocal microscopy (TSCM), have lower axial resolution compared to laser scanning confocal (LSCM) and produce images with reduced contrast, making detection of fine interconnecting nerve branches more challenging. Figure 4-17 shows a comparison between SSCM and LSCM. LSCM studies, most of which used the HRT + RCM combination, report consistent mean nerve density values near 19-21 mm/mm<sup>2</sup>, although differences in image selection procedure can also lead to discrepancy. For instance, in

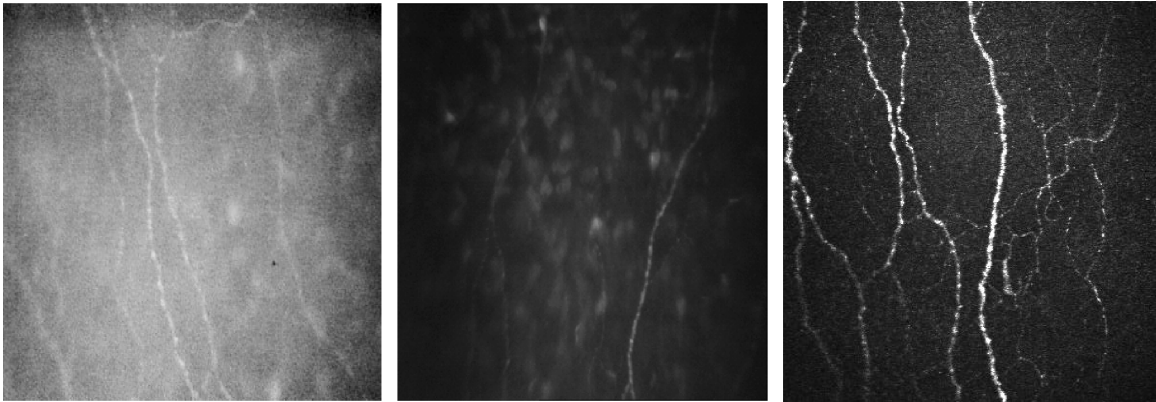


**Figure 4-17:** Subbasal nerve plexus contrast varies considerable depending on the acquisition method. From left to right: Tomey Confocscan, Nidek Confoscan, HRT-RCM. Reproduced from (Tavakoli et al., 2008).

one study (Patel et al., 2009), several non-overlapping images were obtained for each eye and the maximum density for each eye was selected to compute the population mean, leading to an expectedly higher mean. SD was fairly consistent across studies, but is also likely dependent on tracing and image selection criteria. Interestingly, the SD was markedly lower in one study (Patel and McGhee, 2005) where densities were computed from a composite image. The composite image was a montage of several individual frames, forming an area of about  $0.64 \text{ mm}^2$  or about 4X larger than the normal image area. This finding supports the use of a larger FOV, such as that provided with retroillumination microscopy. FF-OCT, another widefield technique, has recently reported a density of  $15 \text{ mm}^2$  in a single subject (Mazlin et al., 2020). This number is somewhat lower than most of those reported in LSCM literature, possibly because FF-OCT contrast is partly degraded by coherency artifacts.

Curiously, all *in vivo* nerve density results are consistently much lower than those reported *ex vivo*. For instance, Marfurt et al. examined 16 donor corneas with immunohistochemically stained anterior cornea whole mounts and reported subbasal

nerve densities of  $46 \pm 5.2$  mm/mm<sup>2</sup> (Marfurt et al., 2010). It is assumed that a large number of fine, interconnecting nerve processes cannot be visualized with current *in vivo* imaging methods. Device-dependency will be a fundamental limitation for the use of *in vivo* corneal nerve density as a useful biomarker.

Future work in retroillumination microscopy will aim to answer whether these fine nerves, invisible in reflection, are viewable in transmission. With the current prototype, the answer appears to be no, however the use of a large NA, increased averaging, or more aggressive spatial filtering may change this.

#### 4.7.6 Defocused contrast

In Section 4.6, we showed how endothelial nuclear contrast was inverted when the focal plane of the microscope was swept through the cellular monolayer. This defocused contrast inversion behavior was not expected based on asymmetric illumination with matched illumination and imaging NAs. Instead it is reminiscent of so-called "partially coherent" imaging (Sheppard, 2002; Sheppard, 2004), where the illumination aperture underfills the imaging aperture (i.e. NA). Like asymmetric illumination, partially coherent imaging converts sample-induced phase differences into intensity contrast on the image plane. It is a generalization of the transport of intensity solution to phase imaging (Teague, 1983).

To better understand the 3D imaging properties of retroillumination microscopy, we developed a wave optics image formation model (see Appendix A). We show simulated 3D point spread functions (PSFs) and optical transfer functions (OTFs). Our conclusion is that retroillumination corneal imaging is both partially coherent and asymmetric.

#### 4.7.7 Future applications

In addition to potential use for large-area corneal nerve tracking, we also anticipate that retroillumination could play a valuable role in very early diagnostics of microbial keratitis (i.e. amoebic, fungal, bacterial). The use of invisible, near-infrared illumination and non-contact operation are key advantages for this application. The method may also be more tolerable in challenging subjects, such as children. In research, the unique ability of retroillumination microscopy to visualize corneal endothelial nuclei may be useful for monitoring proliferative therapies to regenerate endothelial cells.

## Appendix A

# Three-dimensional Image Formation Model for Retroillumination Microscopy

### A.1 Introduction

In this appendix we will formulate a scalar 3D model for partially coherent phase imaging with a microscope. We will use the paraxial (often called Fresnel) approximation (Mertz, 2019), which simplifies the mathematics considerably.

This model is largely derived from seminal works by Streibl (Streibl, 1984; Streibl, 1985). There is little that is new about this derivation. Nonetheless, we have included it in hopes that by providing several intermediate steps (and corrections to original misprints), it will help clarify the original derivation for some interested readers. At the end we provide evaluations of the resulting OTF and PSF for different parameters meant to simulate conditions used in Chapter 4.

### A.2 Propagation of partially coherent light

We define the mutual coherence function as  $\Gamma$ . Assuming that the light is quasi-monochromatic, we can separate the mutual coherence function into space and time-dependent parts.

$$\Gamma(\vec{r}_1, \vec{r}_2; \tau) = \langle u(\vec{r}_1, t') u^*(\vec{r}_2, t' + \tau) \rangle \quad (\text{A.1})$$

$$= J(\vec{r}_1; \vec{r}_2) \exp(i\omega\tau) \quad (\text{A.2})$$



The measurable quantity is the intensity,  $E$  of a light field. It defined as the diagonal part of  $\Gamma$ :

$$E(\vec{r}) = J(\vec{r}; \vec{r}) = \Gamma(\vec{r}, \vec{r}; \tau = 0) \quad (\text{A.3})$$

and note the following restrictions:

$$E(\vec{r}) = J(\vec{r}; \vec{r}) \geq 0 \quad (\text{A.4})$$

$$J(\vec{r}_1; \vec{r}_2) = J^*(\vec{r}; \vec{r}) \quad (\text{A.5})$$

Define an analytical wave as  $u(\vec{r})$ . It must obey the Helmholtz equation:

$$(\nabla^2 + k^2)u(\vec{r}) = 0 \quad (\text{A.6})$$

Now we take the Helmholtz equation and multiply both sides by  $u^*(\vec{r}_2)$ , yielding Helmholtz equation for mutual intensity. Repeat for its complex conjugate. Note that  $\nabla_{1,2}^2$  are Laplace operators specifically on coordinates  $\vec{r}_1$  and  $\vec{r}_2$ :

$$\begin{aligned} (\nabla_1^2 + k^2)u(\vec{r}_1)u^*(\vec{r}_2) &= 0 \\ (\nabla_1^2 + k^2)J(\vec{r}_1; \vec{r}_2) &= 0 \end{aligned} \quad (\text{A.7})$$

$$\begin{aligned} (\nabla_2^2 + k^2)u^*(\vec{r}_2)u(\vec{r}_1) &= 0 \\ (\nabla_2^2 + k^2)J(\vec{r}_1; \vec{r}_2) &= 0 \end{aligned} \quad (\text{A.8})$$

Also the Fourier transform (denoted by the tilde) of mutual intensity is:

$$\begin{aligned} \tilde{J}(\vec{\mu}_1, \eta_1; \vec{\mu}_2, \eta_2) &= \iint J(\vec{x}_1, z_1; \vec{x}_2, z_2) \\ &\times \exp[-2\pi i(\vec{\mu}_1 \cdot \vec{x}_1 - \vec{\mu}_2 \cdot \vec{x}_2 + \eta_1 z_1 - \eta_2 z_2)] d^3\vec{r}_1 d^3\vec{r}_2 \end{aligned} \quad (\text{A.9})$$

where  $\vec{\mu}$  and  $\eta$  denote (2D) lateral and (1D) longitudinal spatial frequencies, respectively. Next we insert the inverse Fourier transform representation of  $J(\vec{r}_1; \vec{r}_2)$  into

each Helmholtz equation.

$$(\nabla_1^2 + k^2) \iint \tilde{J}(\vec{\mu}_1, \eta_1; \vec{\mu}_2, \eta_2) \\ \times \exp[+2\pi i(\vec{\mu}_1 \cdot \vec{x}_1 - \vec{\mu}_2 \cdot \vec{x}_2 + \eta_1 z_1 - \eta_2 z_2)] d^2 \vec{u}_1 d\eta_1 d^2 \vec{u}_2 d\eta_2 = 0$$

$$((2\pi i \mu_1)^2 + (2\pi i \eta_1)^2 + k^2) \iint \tilde{J}(\vec{\mu}_1, \eta_1; \vec{\mu}_2, \eta_2) \\ \times \exp[+2\pi i(\vec{\mu}_1 \cdot \vec{x}_1 - \vec{\mu}_2 \cdot \vec{x}_2 + \eta_1 z_1 - \eta_2 z_2)] d^2 \vec{u}_1 d\eta_1 d^2 \vec{u}_2 d\eta_2 = 0$$

$$\left( \mu_1^2 + \eta_1^2 + \frac{k^2}{(2\pi i)^2} \right) \iint \tilde{J}(\vec{\mu}_1, \eta_1; \vec{\mu}_2, \eta_2) \\ \times \exp[+2\pi i(\vec{\mu}_1 \cdot \vec{x}_1 - \vec{\mu}_2 \cdot \vec{x}_2 + \eta_1 z_1 - \eta_2 z_2)] d^2 \vec{u}_1 d\eta_1 d^2 \vec{u}_2 d\eta_2 = 0$$

$$(\mu_1^2 + \eta_1^2 - \lambda^{-2}) \tilde{J}(\vec{\mu}_1, \eta_1; \vec{\mu}_2, \eta_2) = 0 \quad (\text{A.10})$$

$$(\mu_2^2 + \eta_2^2 - \lambda^{-2}) \tilde{J}(\vec{\mu}_1, \eta_1; \vec{\mu}_2, \eta_2) = 0 \quad (\text{A.11})$$

And thus the spectrum  $\tilde{J}$  is only non-zero on intersection of two hypersurfaces on 6D Fourier space:

$$S_1 : \quad \mu_1^2 + \eta_1^2 = \lambda^{-2} \quad (\text{A.12})$$

$$S_2 : \quad \mu_2^2 + \eta_2^2 = \lambda^{-2} \quad (\text{A.13})$$

$S_1$  and  $S_2$  are spheres for the  $(\vec{\mu}_1, \eta_1)$  and  $(\vec{\mu}_2, \eta_2)$  coordinates. In 6D space, each are 5D hypersurfaces and therefore their intersection is 4D. So a function of 4 variables must be sufficient to specify  $\tilde{J}$  completely. Take a boundary condition in an arbitrary plane (i.e. 4D):

$$J_0(\vec{x}_1; \vec{x}_2) = J(\vec{x}_1, z_1 = 0; \vec{x}_2, z_2 = 0) \quad (\text{A.14})$$

Assuming that no light propagates backwards into the  $z < 0$  half-space from  $z = 0$  plane,

$$\tilde{J}(\vec{\mu}_1, \eta_1; \vec{\mu}_2, \eta_2) = \tilde{J}_0(\vec{\mu}_1; \vec{\mu}_2) \delta\left(\eta_1 - \sqrt{\lambda^{-2} - \mu_1^2}\right) \delta\left(\eta_2 - \sqrt{\lambda^{-2} - \mu_2^2}\right) \quad (\text{A.15})$$

$$\tilde{J}(\vec{\mu}_1, z_1; \vec{\mu}_2, z_2) = \tilde{J}_0(\vec{\mu}_1; \vec{\mu}_2) \exp\left[2\pi i \left(z_1 \sqrt{\lambda^{-2} - \mu_1^2} - z_2 \sqrt{\lambda^{-2} - \mu_2^2}\right)\right] \quad (\text{A.16})$$

Next we inverse Fourier transform Equation A.16 and use the convolution theorem of the Fourier transform to obtain the general result for mutual intensity propagation throughout space.

$$\begin{aligned} J(\vec{x}_1, z_1; \vec{x}_2, z_2) &= \iint \tilde{J}_0(\vec{\mu}_1; \vec{\mu}_2) \exp\left[2\pi i \left(z_1 \sqrt{\lambda^{-2} - \mu_1^2} - z_2 \sqrt{\lambda^{-2} - \mu_2^2}\right)\right] \\ &\quad \times \exp[+2\pi i(\vec{\mu}_1 \cdot \vec{x}_1 - \vec{\mu}_2 \cdot \vec{x}_2)] d^2 \vec{\mu}_1 d^2 \vec{\mu}_2 \\ J(\vec{x}_1, z_1; \vec{x}_2, z_2) &= \iint J_0(\vec{x}'_1; \vec{x}'_2) K(\vec{x}_1 - \vec{x}'_1, z_1; \vec{x}_2 - \vec{x}'_2, z_2) d^2 \vec{x}'_1 d^2 \vec{x}'_2 \quad (\text{A.17}) \end{aligned}$$

And we have defined auxiliary function  $K(\vec{\xi}_1, z_1; \vec{\xi}_2, z_2)$  as:

$$\begin{aligned} K(\vec{\xi}_1, z_1; \vec{\xi}_2, z_2) &= \iint \exp\left[2\pi i \left(z_1 \sqrt{\lambda^{-2} - \mu_1^2} - z_2 \sqrt{\lambda^{-2} - \mu_2^2}\right)\right] \\ &\quad \times \exp\left[+2\pi i \left(\vec{\mu}_1 \cdot \vec{\xi}_1 - \vec{\mu}_2 \cdot \vec{\xi}_2\right)\right] d^2 \vec{\mu}_1 d^2 \vec{\mu}_2 \quad (\text{A.18}) \end{aligned}$$

### A.3 Propagation of 3D intensity

We have derived a general expression for the propagation of mutual intensity, given a boundary condition, throughout space. We next derive similar expressions for the more practically useful quantity, intensity. Recall that intensity is the diagonal part of the mutual intensity (Eqn. A.3). It can be thought of as a slice  $\vec{r}_1 = \vec{r}_2$  in 6D mutual intensity space. Since slicing and projection are Fourier-reciprocal operations, in the

Fourier domain, we have the following projection law:

$$\tilde{E}(\vec{\mu}, \eta) = \iint \tilde{J}(\vec{\mu}' + \frac{1}{2}\vec{\mu}, \eta' + \frac{1}{2}\eta; \vec{\mu}' - \frac{1}{2}\vec{\mu}, \eta' - \frac{1}{2}\eta) d^2\vec{\mu}' d\eta' \quad (\text{A.19})$$

Next we insert the fully-Fourier domain propagation law (Eqn. A.15) into the projection law (Eqn. A.19):

$$\begin{aligned} \tilde{E}(\vec{\mu}, \eta) = \iint \tilde{J}_0(\vec{\mu}' + \frac{1}{2}\vec{\mu}; \vec{\mu}' - \frac{1}{2}\vec{\mu}) & \delta\left(\eta' + \frac{1}{2}\eta - \sqrt{\lambda^{-2} - |\vec{\mu}' + \frac{1}{2}\vec{\mu}|^2}\right) \\ & \times \delta\left(\eta' - \frac{1}{2}\eta - \sqrt{\lambda^{-2} - |\vec{\mu}' - \frac{1}{2}\vec{\mu}|^2}\right) d^2\vec{\mu}' d\eta' \end{aligned} \quad (\text{A.20})$$

$$\begin{aligned} \tilde{E}(\vec{\mu}, \eta) = \int \tilde{J}_0(\vec{\mu}' + \frac{1}{2}\vec{\mu}; \vec{\mu}' - \frac{1}{2}\vec{\mu}) \\ \times \delta\left(\eta - \sqrt{\lambda^{-2} - |\vec{\mu}' + \frac{1}{2}\vec{\mu}|^2} + \sqrt{\lambda^{-2} - |\vec{\mu}' - \frac{1}{2}\vec{\mu}|^2}\right) d^2\vec{\mu}' \end{aligned} \quad (\text{A.21})$$

A major simplification results from approximating the square roots by their first order Taylor expansion,

$$\sqrt{a^2 - x^2} = a^2 \sqrt{1 - (x/a)^2} \approx a^2 \left(1 - \frac{1}{2} \left(\frac{x}{a}\right)^2\right) = a^2 - \frac{1}{2}x^2 \quad (\text{A.22})$$

The argument in Equation A.21 then becomes,

$$\begin{aligned} \eta - \sqrt{\lambda^{-2} - |\vec{\mu}' + \frac{1}{2}\vec{\mu}|^2} + \sqrt{\lambda^{-2} - |\vec{\mu}' - \frac{1}{2}\vec{\mu}|^2} \\ = \eta - \lambda^{-2} + \frac{\lambda}{2}(\mu'^2 + \vec{\mu}' \cdot \vec{\mu} + \frac{1}{4}\mu^2) + \lambda^{-2} - \frac{\lambda}{2}(\mu'^2 - \vec{\mu}' \cdot \vec{\mu} + \frac{1}{4}\mu^2) \\ \eta - \sqrt{\lambda^{-2} - |\vec{\mu}' + \frac{1}{2}\vec{\mu}|^2} + \sqrt{\lambda^{-2} - |\vec{\mu}' - \frac{1}{2}\vec{\mu}|^2} = \eta + \lambda\vec{\mu} \cdot \vec{\mu}' \end{aligned}$$

And we can now rewrite Equation A.21 as

$$\tilde{E}(\vec{\mu}, \eta) = \int \tilde{J}_0(\vec{\mu}' + \frac{1}{2}\vec{\mu}; \vec{\mu}' - \frac{1}{2}\vec{\mu}) \delta(\eta + \lambda\vec{\mu} \cdot \vec{\mu}') d^2\vec{\mu}' \quad (\text{A.23})$$

This is a general expression for propagation of intensity throughout 3D space given the mutual intensity at plane  $z = 0$ .

#### A.4 Born approximation

Now we will consider our object to be imaged. It will be described in terms of its complex 3D refractive index distribution  $n(\vec{r})$ . For a slowly varying object (compared to the wavelength,  $\lambda$ ), then the light field amplitude obeys yet another Helmholtz equation:

$$[\nabla^2 + n^2(\vec{r})k^2] u(\vec{r}) = 0 \quad (\text{A.24})$$

We can equivalently describe the object by its scattering potential,  $V(\vec{r})$ , defined as:

$$V(\vec{r}) = k^2(1 - n^2(\vec{r})) \quad (\text{A.25})$$

$$(\nabla^2 + k^2)u(\vec{r}) = V(\vec{r})u(\vec{r}) \quad (\text{A.26})$$

We can also decompose  $V(\vec{r})$  into its real and imaginary parts,  $P$  and  $A$ , which correspond to phase and absorption, respectively.

$$V(\vec{x}, z) = P(\vec{x}, z) + iA(\vec{x}, z) \quad (\text{A.27})$$

For corneal imaging, we will assume no absorption, leading to the simplification that

$$V(\vec{x}, z) = P(\vec{x}, z); \quad (\text{A.28})$$

Recalling that  $J(\vec{r}_1; \vec{r}_2) = \langle u(\vec{r}_1)u^*(\vec{r}_2) \rangle$  (Eqn. A.1), we multiply both sides by  $u^*(\vec{r}_2)$  (and its complex conjugate),

$$(\nabla_1^2 + k^2)J(\vec{r}_1; \vec{r}_2) = V(\vec{r}_1)J(\vec{r}_1; \vec{r}_2) \quad (\text{A.29})$$

$$(\nabla_2^2 + k^2)J(\vec{r}_1; \vec{r}_2) = V^*(\vec{r}_2)J(\vec{r}_1; \vec{r}_2) \quad (\text{A.30})$$

Next we define the Green function  $G(\vec{r})$  of the Helmholtz equation as,

$$(\nabla^2 + k^2)G(\vec{r} - \vec{r}') = \delta(\vec{r} - \vec{r}') \quad (\text{A.31})$$

Assume that the mutual intensity satisfies the follows equation,

$$\begin{aligned} J(\vec{r}_1; \vec{r}_2) = & J_{IN}(\vec{r}_1; \vec{r}_2) + \iint [G(\vec{r}_1 - \vec{r}'_1)V(\vec{r}'_1)\delta(\vec{r}_2 - \vec{r}'_2) + \delta(\vec{r}_1 - \vec{r}'_1)G^*(\vec{r}_2 - \vec{r}'_2)V^*(\vec{r}'_2) \\ & - G(\vec{r}_1 - \vec{r}'_1)V(\vec{r}'_1)G^*(\vec{r}_2 - \vec{r}'_2)V^*(\vec{r}'_2)] \times J(\vec{r}'_1; \vec{r}'_2)d^3\vec{r}'_1d^3\vec{r}'_2 \quad (\text{A.32}) \end{aligned}$$

This is the mutual intensity of the light field just after interacting with the sample. It is possible to verify this equation by applying operator  $(\nabla_1^2 + k^2)$ , using Equation A.31, and noting that  $(\nabla_1^2 + k^2)J_{IN}(\vec{r}_1; \vec{r}_2) = 0$ . The result should simplify to Equation A.29. We will also assume that the object is weak ( $V(\vec{r}) \ll 0$ ), allowing us to use the first Born approximation and thus simplify Equation A.32 as,

$$\begin{aligned} J(\vec{r}_1; \vec{r}_2) = & J_{IN}(\vec{r}_1; \vec{r}_2) + \iint [G(\vec{r}_1 - \vec{r}'_1)V(\vec{r}'_1)\delta(\vec{r}_2 - \vec{r}'_2) \\ & + \delta(\vec{r}_1 - \vec{r}'_1)G^*(\vec{r}_2 - \vec{r}'_2)V^*(\vec{r}'_2)] \times J_{IN}(\vec{r}'_1; \vec{r}'_2)d^3\vec{r}'_1d^3\vec{r}'_2 \quad (\text{A.33}) \end{aligned}$$

The physical meaning of this approximation is that incident light interacts (i.e. scatters) only once with the object before being captured by the imaging optics.

## A.5 3D image formation

In this part we will consider the interaction of an incoherent light source  $\tilde{S}(\vec{\mu})$  with our sample, in terms of mutual intensity. Then we will use our intensity propagation law (Eqn. A.23) to compute the intensity image on the microscope camera plane. We will first apply the van Cittert-Zernike theorem and propagation laws of mutual

intensity (Mertz, 2019) to compute the incident mutual intensity on the object.

$$J_{IN}(\vec{x}_1, z_1; \vec{x}_2, z_2) = \int \tilde{S}(\vec{\mu}) \exp\{2\pi i[(z_1 - z_2)\sqrt{\lambda^{-2} - |\vec{\mu}|^2} + (\vec{x}_1 - \vec{x}_2) \cdot \vec{\mu}]\} d^2 \vec{\mu} \quad (\text{A.34})$$

When inserting this into the first order Born approximation (Eqn. A.33), we obtain several integrals of the type:

$$H = \int G(\vec{r}_1 - \vec{r}'_1) V(\vec{r}'_1) J_{IN}(\vec{r}'_1; \vec{r}_2) d^3 \vec{r}_1 \quad (\text{A.35})$$

We will use the angular spectrum representation (sometimes called the Weyl form) of the Green function  $G(\vec{r})$ , which is a spherical wave. Conveniently, the lateral spatial frequency spectrum of the Green function is then:

$$\tilde{G}(\vec{\mu}, z) = \frac{1}{4\pi i \sqrt{\lambda^{-2} - |\vec{\mu}|^2}} \exp[2\pi i |z| \sqrt{\lambda^{-2} - |\vec{\mu}|^2}] \quad (\text{A.36})$$

Then plugging this into Equation A.35 along with Equation A.34, we obtain:

$$H = \iiint V(\vec{x}'_1, z'_1) \frac{\tilde{S}(\vec{\mu}_2)}{4\pi i \sqrt{\lambda^{-2} - |\vec{\mu}_1|^2}} \exp\{2\pi i[(z'_1 - z_2)\sqrt{\lambda^{-2} - |\vec{\mu}_2|^2} + (\vec{x}'_1 - \vec{x}_2) \cdot \vec{\mu}_2 + |z_1 - z'_1| \sqrt{\lambda^{-2} - |\vec{\mu}_1|^2} + (\vec{x}_1 - \vec{x}'_1) \cdot \vec{\mu}_1]\} d^2 \vec{\mu}_1 d^2 \vec{\mu}_2 d^2 \vec{x}'_1 d^2 z'_1 \quad (\text{A.37})$$

If we only collect forward scattered light then,

$$|z_1 - z'_1| = z_1 - z'_1 \geq 0$$

and drop phase factors related to  $z_2$  and  $z_1$ , then Equation A.37 becomes:

$$H = \iint \frac{\tilde{S}(\vec{\mu}_2)}{4\pi i \sqrt{\lambda^{-2} - |\vec{\mu}_1|^2}} \exp\{2\pi i[(\vec{x}_1 \cdot \vec{\mu}_1 - \vec{x}_2 \cdot \vec{\mu}_2) \int V(\vec{x}'_1, z'_1) \times \exp\{-2\pi i[\vec{x}'_1 \cdot (\vec{\mu}_1 - \vec{\mu}_2) + z'_1 \sqrt{\lambda^{-2} - |\vec{\mu}_1|^2} - z'_2 \sqrt{\lambda^{-2} - |\vec{\mu}_2|^2}]\} d^2 \vec{x}'_1 d^2 z'_1 d^2 \vec{\mu}_1 d^2 \vec{\mu}_2 \quad (\text{A.38})$$

Notice that the inner integral (involving  $x'_1$  and  $z'_1$ ) is a scaled Fourier transform of the object  $V$  and the outer integral is also a Fourier transform. If we Fourier transform the first Born approximation (Eqn. A.33) and insert Equation A.37 (and its complex conjugate) in, we arrive at:

$$\begin{aligned} \tilde{J}_{\text{OBJ}}(\vec{\mu}_1; \vec{\mu}_2) &= \tilde{S}(\vec{\mu}_1)\delta(\vec{\mu}_1 - \vec{\mu}_2) \\ &+ \frac{\tilde{S}(\vec{\mu}_2)}{4\pi i \sqrt{\lambda^{-2} - |\vec{\mu}_1|^2}} \tilde{V} \left[ \vec{\mu}_1 - \vec{\mu}_2, \sqrt{\lambda^{-2} - |\vec{\mu}_1|^2} - \sqrt{\lambda^{-2} - |\vec{\mu}_2|^2} \right] \\ &- \frac{\tilde{S}(\vec{\mu}_1)}{4\pi i \sqrt{\lambda^{-2} - |\vec{\mu}_2|^2}} \tilde{V}^* \left[ \vec{\mu}_2 - \vec{\mu}_1, \sqrt{\lambda^{-2} - |\vec{\mu}_2|^2} - \sqrt{\lambda^{-2} - |\vec{\mu}_1|^2} \right] \end{aligned} \quad (\text{A.39})$$

where  $\tilde{V}(\vec{\mu}, \eta)$  represents the 3D Fourier transform of the object scattering potential,  $V(\vec{x}, z)$ . Since  $V(\vec{x}, z)$  is purely real (we assumed a pure phase object in Eqn. A.28) its Fourier conjugate is Hermitian, i.e.

$$\tilde{V}(\vec{\mu}, \eta) = \tilde{V}^*(-\vec{\mu}, -\eta) \quad (\text{A.40})$$

We will also approximate the square roots in Equation A.39 as their Taylor expansion (similar to Eqn. A.22) and relabel the scattering potential spectrum,  $\tilde{V}(\vec{\mu}, \eta)$  as  $\tilde{P}(\vec{\mu}, \eta)$ , leading to,

$$\begin{aligned} \tilde{J}_{\text{OBJ}}(\vec{\mu}_1; \vec{\mu}_2) &= \tilde{S}(\vec{\mu}_1)\delta(\vec{\mu}_1 - \vec{\mu}_2) \\ &+ \frac{\lambda}{4\pi i} [\tilde{S}(\vec{\mu}_2) - \tilde{S}(\vec{\mu}_1)] \tilde{P} \left[ \vec{\mu}_1 - \vec{\mu}_2, \frac{\lambda}{2} (|\vec{\mu}_2|^2 - |\vec{\mu}_1|^2) \right] \end{aligned} \quad (\text{A.41})$$

This equation represents the mutual intensity immediately following interaction with the sample. For a telecentric unit-magnification imaging system, the mutual intensity spectrum at the image plane,  $\tilde{J}_{\text{IMG}}$  is obtained by multiplying the object mutual intensity spectrum,  $\tilde{J}_{\text{OBJ}}$  by the system pupil function (Mertz, 2019):

$$\tilde{J}_{\text{IMG}}(\vec{\mu}_1; \vec{\mu}_2) = \tilde{p}(\vec{\mu}_1) \tilde{J}_{\text{OBJ}}(\vec{\mu}_1; \vec{\mu}_2) \tilde{p}^*(\vec{\mu}_2) \quad (\text{A.42})$$



To compute the intensity at the camera plane, we use the paraxial intensity propagation law (Eqn. A.23) derived earlier, along with Equations A.41 and A.42 to obtain the main result:

$$\tilde{E}_{\text{IMG}}(\vec{\mu}, \eta) = B\delta(\vec{\mu}, \eta) + \tilde{P}(\vec{\mu}, \eta)\tilde{T}_P(\vec{\mu}, \eta) \quad (\text{A.43})$$

$B$  is the uniform background light intensity and  $\tilde{T}_P(\vec{\mu}, \eta)$  is the phase to intensity transfer function, more commonly known as the optical transfer function (OTF), defined as:

$$\begin{aligned} \tilde{T}_P(\vec{\mu}, \eta) = \frac{i\lambda}{4\pi} \int \tilde{p}(\vec{\mu}' + \frac{1}{2}\vec{\mu})\tilde{p}^*(\vec{\mu}' - \frac{1}{2}\vec{\mu}) \\ [\tilde{S}(\vec{\mu}' + \frac{1}{2}\vec{\mu}) - \tilde{S}(\vec{\mu}' - \frac{1}{2}\vec{\mu})]\delta(\eta + \lambda\vec{\mu} \cdot \vec{\mu}')d^2\vec{\mu}' \end{aligned} \quad (\text{A.44})$$

The Fourier transform of  $\tilde{T}_P(\vec{\mu}, \eta)$  is the point spread function (PSF), and hence the intensity image is the convolution of the PSF with the phase distribution:

$$E_{\text{IMG}}(\vec{r}) = B + P(\vec{r}) * * * T_P(\vec{r}) \quad (\text{A.45})$$

where  $***$  denotes 3D convolution. To compute the OTF, it is useful to invoke the following delta function property:

$$\int_{R^n} f(\vec{x})\delta(g(\vec{x}))d\vec{x} = \int_{g^{-1}(0)} \frac{f(\vec{x})}{|\nabla g|}d\sigma(\vec{x}) \quad (\text{A.46})$$

where  $g^{-1}(0)$  is the  $n - 1$  dimensional surface defined by  $g(\vec{x}) = 0$  and  $\sigma$  is the hypersurface measure. For our derivation, we can use this property to replace the two-dimensional transfer function integral (Eqn. A.44) with a simpler line integral:

$$\tilde{T}_P(\vec{\mu}, \eta) = \int_L \frac{\tilde{p}(\vec{\mu}' + \frac{1}{2}\vec{\mu})\tilde{p}^*(\vec{\mu}' - \frac{1}{2}\vec{\mu})[\tilde{S}(\vec{\mu}' + \frac{1}{2}\vec{\mu}) - \tilde{S}(\vec{\mu}' - \frac{1}{2}\vec{\mu})]}{|\nabla g|}ds \quad (\text{A.47})$$

where

$$|\nabla g| = |\nabla(\eta + \lambda\vec{\mu} \cdot \vec{\mu}')| = \lambda|\vec{\mu}| \quad (\text{A.48})$$

resulting in

$$\tilde{T}_P(\vec{\mu}, \eta) = \frac{1}{\lambda|\vec{\mu}|} \int_L \tilde{p}(\vec{\mu}' + \frac{1}{2}\vec{\mu}) \tilde{p}^*(\vec{\mu}' - \frac{1}{2}\vec{\mu}) [\tilde{S}(\vec{\mu}' + \frac{1}{2}\vec{\mu}) - \tilde{S}(\vec{\mu}' - \frac{1}{2}\vec{\mu})] ds \quad (\text{A.49})$$

and  $L$  is the line parameterized by  $\eta + \lambda\vec{\mu} \cdot \vec{\mu}' = 0$ .

## A.6 Evaluation of the 3D OTF and PSF

We characterize symmetric and circular source and diffraction-limited pupil functions by spatial frequency cutoffs  $\rho_S$  and  $\rho_p$ , respectively. That is,

$$\tilde{p}(\vec{\mu}) = \begin{cases} 1 & \text{if } |\vec{\mu}| < \rho_p \\ 0 & \text{otherwise} \end{cases} \quad (\text{A.50})$$

$$\tilde{S}_{\text{SYM}}(\vec{\mu}) = \begin{cases} 1 & \text{if } |\vec{\mu}| < \rho_S \\ 0 & \text{otherwise} \end{cases} \quad (\text{A.51})$$

Additionally, for asymmetric illumination we impose:

$$\tilde{S}_{\text{ASYM}}(\vec{\mu}) = \begin{cases} 0 & \text{if } |\vec{\mu}| > \rho_S \\ 0 & \text{if } \mu_x > 0 \\ 1 & \text{otherwise} \end{cases} \quad (\text{A.52})$$

An analytical solution exists for the circularly-symmetric case (Streibl, 1985), but does exist for the asymmetric case. Instead, in this section we will evaluate several OTFs with both symmetric and asymmetric illumination and with varying levels of coherence. We parameterize coherence by  $\gamma = \rho_S/\rho_p$ , which we will call the

“incoherence” factor.  $\gamma = 0$  is completely coherent and  $\gamma = 1$  is incoherent (also called “matched” coherence).

For this simulation we try to closely mimic the parameters used in Chapter 4. Therefore, the wavelength is set to 850 nm, the maximum NA for illumination and imaging is 0.4, and the pixel pitch is 0.5  $\mu\text{m}$ . The results are shown in Figure A.1.

Symmetric illumination produces OTFs with odd symmetry about the  $\eta = 0$  plane. Upon projection along  $\eta$ , as is done to compute the in-focus lateral spectrum of a thin sample, we find that the OTF amplitude vanishes. This agrees with the well-known observation that symmetric illumination is insensitive to weak in-focus phase objects. When a thin sample is moved out of focus, or the sample is volumetric, imbalances about the  $\eta = 0$  plane result in a non-zero lateral spectrum when projected (i.e. imaged) onto a plane. Additionally, we see that for incoherent ( $\gamma = 1$ ) symmetric illumination, there is no possible contrast regardless of focus.

For high coherence ( $\gamma = 0.1$ ) asymmetric illumination, the OTF is similar to that of symmetric illumination. However, for partial coherence ( $\gamma = 0.75$ ) an asymmetry in the OTF is observed. For an in focus thin sample, the resulting image would display gradients of phase along the  $\mu_x$  axis. We also observe for the incoherent asymmetric case, that image contrast is in fact obtainable. This case also provides the highest lateral and axial frequency support.

We have also computed the PSF for each OTF in Figure A.1 by 3D Fourier transformation. Individual *en face* frames from the PSF at various depths are shown on the left side of Figure A.2 while cross-sectional XZ slices of each PSF are displayed in the right column. We see that symmetric illumination indeed provides no contrast when in focus ( $z = 0$ ) or completely incoherent ( $\gamma = 1$ ), and positive/negative contrast when out-of-focus. The asymmetric case is similar for low coherence ( $\gamma = 0.1$ ). For incoherent asymmetric illumination, the gradient of a point along  $x$  is observed

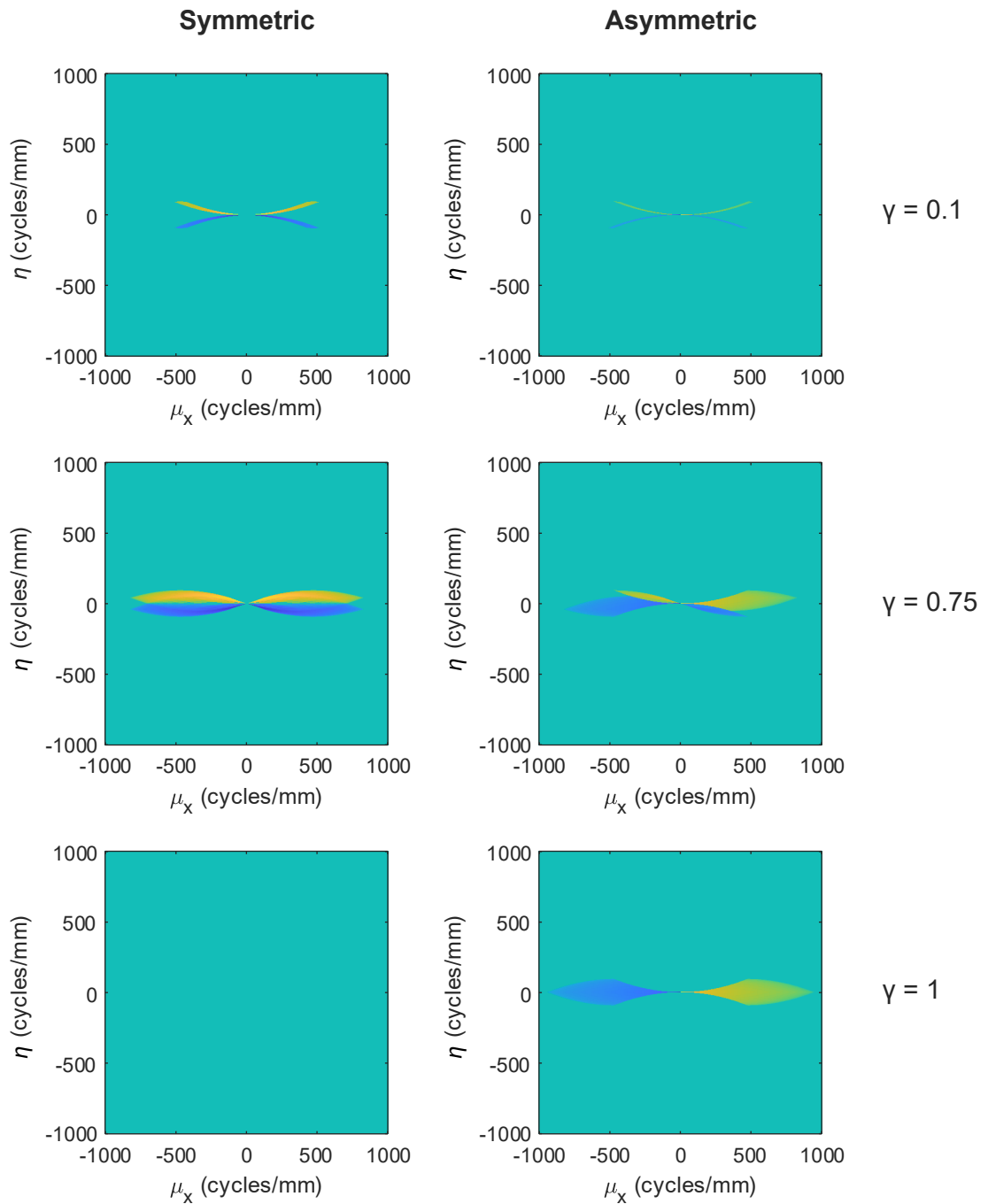


**Figure A.1:** Phase OTFs for symmetric and asymmetric illumination configurations with varying coherence  $\gamma$ .  $\eta$  and  $\mu$  and longitudinal and lateral spatial frequencies, respectively. Amplitudes are shown in bipolar log scale to improve visibility of small amplitudes.

in focus and quickly diminishes out of focus. The partially coherent asymmetric case appears to be a combination of asymmetric (left-right contrast inversion) and coherent (anterior-posterior contrast inversion) behavior, similar to what we observed in the endothelium (see Fig. 4-16, especially).

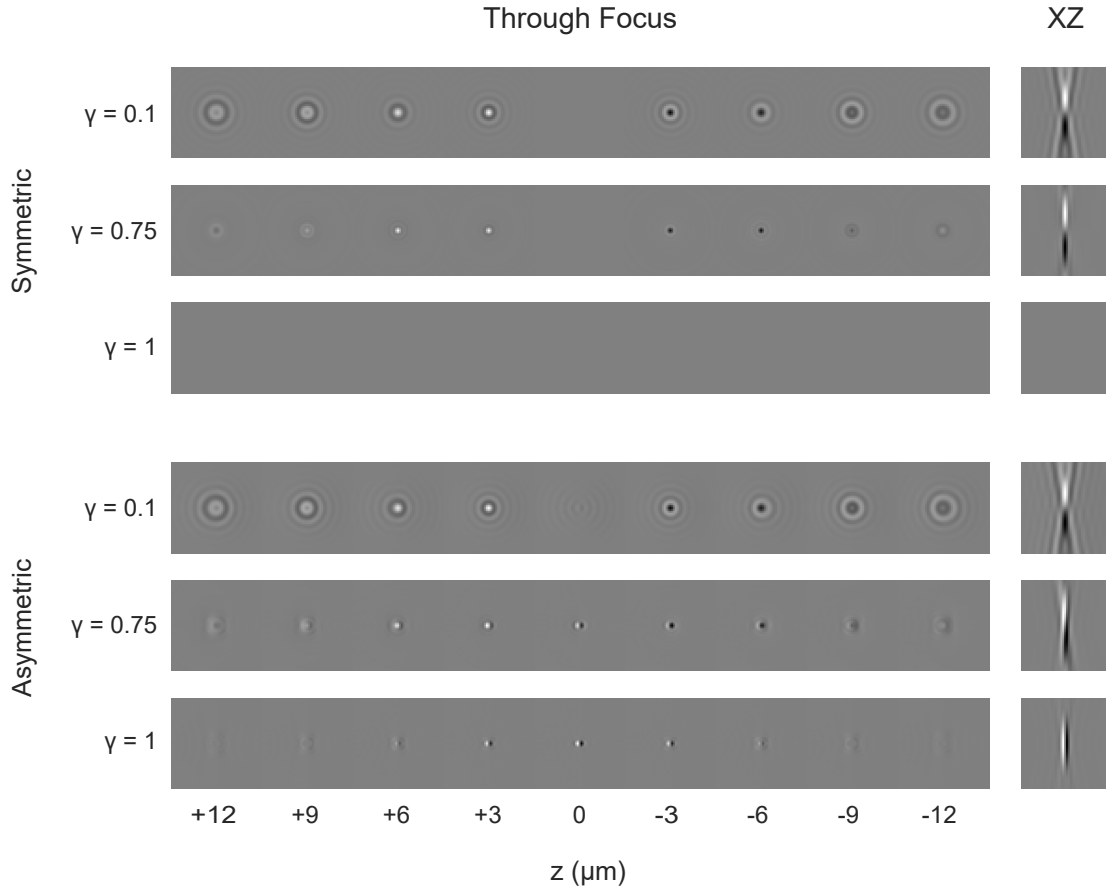


**Figure A-2:** Phase PSF axial sweep for both symmetric and asymmetric illumination configurations at various levels of coherence. Frame length/width: 12  $\mu\text{m}$ . The right column shows sagittal XZ slices through the 3D PSF for each configuration.

Endothelial cell nuclei are, however, not point objects. To model endothelial nuclei more accurately we used a sphere of homogeneous refractive index (higher than the background index) as the object in our model and recomputed the image at multiple depths. We additionally added a significant level of Gaussian white noise to simulate

realistic imaging conditions. The results for asymmetric illumination are shown in Figure A.3. The partially coherent case ( $\gamma = 0.75$ ) appears to recapitulate some of the behavior observed in Figure 4.16, namely the faint appearance of edges when in focus, and the stronger positive/negative contrast when defocused.

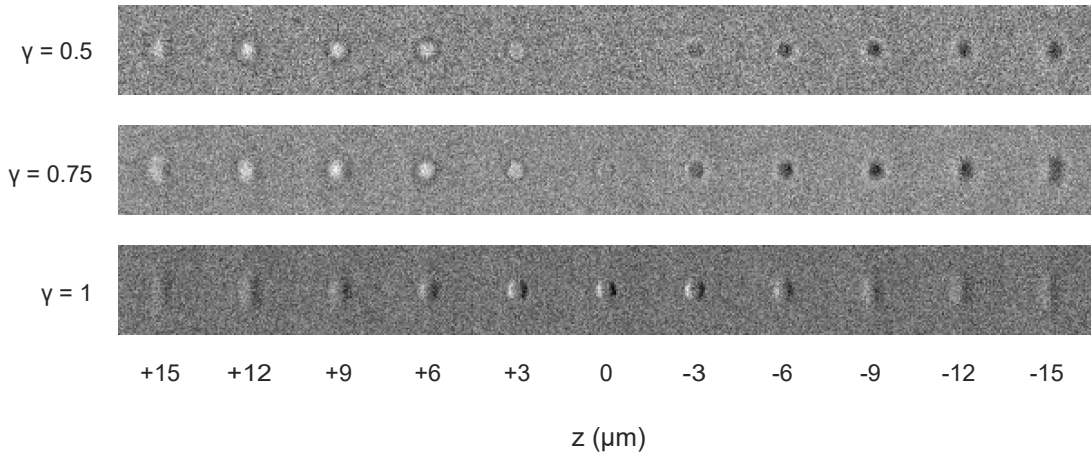


**Figure A.3:** Simulation of imaging a single endothelial cell nucleus with asymmetric illumination and varying degrees of coherence,  $\gamma$ . The nucleus diameter is  $5 \mu\text{m}$ , and a constant amount of Gaussian noise has been added to simulate shot noise.

This numerical simulation suggests that retroillumination imaging is both asymmetric and partially coherent. We believe that the reason the illumination is not incoherent, as one might have expected based on filling the objective aperture with the illumination beam (see Sec. 4.2.1), is because retroreflected rays illuminating the cornea have not been fully refracted by the corneal anterior surface. The model presented here is a start, but more detailed modelling, possibly using a finite eye model (Atchison and Smith, 2000), is needed to address this hypothesis and confidently predict the impact on 3D imaging.

## Appendix B

# Code for three-dimensional image formation model

### B.1 Outline

The following appendix contains the MATLAB code used to evaluate 3D optical transfer functions (OTFs) from Appendix A and simulate resulting 3D images of various test objects. The main script is `run_simulation.m`, which contains high-level commands. A list of user-adjustable parameters and brief descriptions is contained in script, `load_params.m`. The remaining files are ancillary and can be filed in an active subfolder named `utilities/`.

### B.2 Code

**Listing B.1:** Main simulation script, `run_simulation.m`

```

1 %% RUN_SIMULATION
2 % Main script to call a series of functions which simulate 3D imaging of a
3 % weak absorption or phase object with a widefield transmission microscope.
4 % Degree of coherence is adjustable.
5 %
6 % Timothy Weber
7 % Biomicroscopy Lab, BU
8 % April 2020
9
10
11 %% Set up: load the parameters, add subfolders to path
12 % Open "load_params" file to review all settings
13 load_params
14 addpath('utilities')
15
16
17 %% Generate OTF

```

```

18 % Determine spatial frequency range (variables correspond to Streibl's)
19 [mu_x,mu_y,eta] = set_spatial_freq_range(p);
20
21 % Generate transfer functions
22 [ptf,atf] = generate_TF_paraxial(p,mu_x,mu_y,eta);
23
24 % Pad the transfer functions to correct size
25 [ptf,atf] = pad_TFs(ptf,atf,p);
26
27
28 %% Filter object
29 object = make_3d_object(p);
30
31 % Filter with phase and absorption TFs
32 objectSpectrum = fftn(object);
33 objSpecFiltPhase = objectSpectrum.*ifftshift(ptf);
34 objFilteredPhase = real(1i*ifftn(objSpecFiltPhase));
35 objSpecFiltAbsorption = objectSpectrum.*ifftshift(atf);
36 objFilteredAbsorption = real(ifftn(objSpecFiltAbsorption));
37
38 % Add noise
39 imgPhase = objFilteredPhase + randn(size(objFilteredPhase)).*p.noiseLevel;
40 imgAbsorption = objFilteredAbsorption + randn(size(objFilteredAbsorption)).*p.
    noiseLevel;
41
42
43 %% Show simulated images
44 % Make composite through focus (axial sweep) images for display
45 compositeImgPhase = thru_focus_axial_slice(imgPhase,p.crop,p.frameThruFocusStartEnd,p.
    .frameThruFocusdz);
46 compositeImgAbsorption = thru_focus_axial_slice(-imgAbsorption,p.crop,p.
    frameThruFocusStartEnd,p.frameThruFocusdz);
47
48 subplot(2,1,1)
49 imshow(compositeImgPhase)
50 title(['Phase: ' label_maker(p)])
51 subplot(2,1,2)
52 imshow(compositeImgAbsorption)
53 title(['Absorption: ' label_maker(p)])

```

**Listing B.2:** List of simulation parameters, load\_params.m

```

1 %% LOAD_PARAMS
2 % Loads simulation parameters and put them into a structure, "p"
3 % Bracketed quantities in comments denote units
4
5 % Basic simulation parameters
6 p.dataType = 'single';      % data type in which to compute OTF (single or double)
7 p.pixelSize = 1/2;         % [um] per pixel
8
9 % Imaging parameters
10 p.lightWavelength = 0.85;  % [um]
11 p.imagingNA = 0.4;

```



```

12 p.gamma = 0.75;           % aka incoherence factor (0 is completely coherence, 1 is
    incoherent)
13 p.asymmetricIllumination = true;
14
15 % Number of points used to approximate line integral for each transfer function point
16 p.numLineIntPoints = 48;
17
18 % Object options
19 p.objectSize = 64;       % [um]
20 p.objectType = 'point';  % options: point, sphere, tube, monolayer
21 p.deltaN = single(0.1);  % refractive index difference, keep in single precision
22 p.radius = 1;           % [um], only for object type: sphere, tube, monolayer
23
24 % Object monolayer settings (only if using monolayer object type)
25 p.sphereCenterSpacing = 10; % [um]
26 p.centerRandomOffset = .5;
27 p.tiltXY = [.01 .03];    % [rad], about x axis and about y axis, resp.
28
29 % Display settings
30 p.noiseLevel = .002;
31 p.thruFocusImgWidthCrop = 12; % [um]
32 p.thruFocusRange = 15;    % [um] +/- from the focal plane
33 p.thruFocusdz = 3;        % [um]
34
35 % Automatically calculated
36 p.arrayLength = p.objectSize/p.pixelSize;
37 p.illuminationNA = p.imagingNA*p.gamma;
38 p.crop = p.thruFocusImgWidthCrop/p.pixelSize;
39 p.frameThruFocusStartEnd = p.thruFocusRange./p.pixelSize;
40 p.frameThruFocusdz = p.thruFocusdz./p.pixelSize;

```

## B.2.1 Utilities

The following functions are utilities and may be placed in a folder titled “utilities” for organization (optional).

**Listing B.3:** Generates phase and absorption 3D transfer functions with the paraxial approximation, `generate_TF_paraxial.m`

```

1 function [phaseTF,absorptionTF] = generate_TF_paraxial(p,mu_x,mu_y,eta)
2 % GENERATE_TF_PARAXIAL
3 % Function to generate phase and absorption transfer functions (TFs) for a
4 % partially coherent microscope under paraxial approximation.
5 %
6 % Variable names roughly match Streibl's notation, that is
7 % mu_x/y are transverse spatial frequencies
8 % eta is longitudinal spatial frequency
9
10 % Make sure 1D vectors are in correct dims: mu_x occupies 1st dimension,
11 % mu_y dim 2, eta dim 3, and t (which will be integration variable) dim 4
12 mu_x = mu_x(:)';
13 mu_y = mu_y(:);
14 eta = reshape(eta(:),[1 1 numel(eta)]);
15
16 % convert to requested data type
17 if strcmp(p.dataType,'single')
18     mu_x = single(mu_x);
19     mu_y = single(mu_y);
20     eta = single(eta);
21     p.imagingNA = single(p.imagingNA);
22     p.lightWavelength = single(p.lightWavelength);
23 end
24
25 % Autocalculated parameter: defines int limits of line integral [um^-1]
26 muLim = p.imagingNA*p.lightWavelength^-1;
27
28 % Make the amplitude/coherent transfer functions CSFs: tilde{p} & tilde{S}
29 [tildep,tildeS] = make_imaging_illumination_csfs(p);
30
31 % Make line integral parameter, t
32 t = reshape(linspace(-muLim,muLim,p.numLineIntPoints),[1 1 1 p.numLineIntPoints]);
33
34 % Transverse spatial frequency modulus
35 muAbs = sqrt(mu_x.^2 + mu_y.^2);
36
37 % Parameterize the primed variables (mu_x' and mu_y') by first forming a
38 % line as if mu_y=0 and mu_x,eta/=0, then rotate into place
39 mu_par = -eta./(p.lightWavelength.*muAbs);
40 mu_perp = t;
41 theta = atan2(mu_y,mu_x);
42 cosTheta = cos(theta); sinTheta = sin(theta); clear theta
43 mu_xPrime = cosTheta.*mu_par - sinTheta.*mu_perp;
44 mu_yPrime = sinTheta.*mu_par + cosTheta.*mu_perp; clear sinTheta cosTheta mu_par

```

```

45
46 % Break up integral into parts,
47 % part 0: prefactors
48 % part 1: tildep(muPrime + 1/2 mu) tildep*(muPrime - 1/2 mu)
49 % part 2A (for absorption): tildeS(muPrime + 1/2 mu) + tildeS(muPrime - 1/2 mu)
50 % part 2A (for phase): tildeS(muPrime + 1/2 mu) - tildeS(muPrime - 1/2 mu)
51 part0 = muAbs;
52 part1 = tildep(mu_xPrime+0.5*mu_x,mu_yPrime+0.5*mu_y).*conj(tildep(mu_xPrime-0.5*mu_x
    ,mu_yPrime-0.5*mu_y));
53 S1 = tildeS(mu_xPrime+0.5*mu_x,mu_yPrime+0.5*mu_y);
54 S2 = tildeS(mu_xPrime-0.5*mu_x,mu_yPrime-0.5*mu_y); clear mu_xPrime mu_yPrime
55 part2A = S1 + S2;
56 part2P = S1 - S2; clear S1 S2
57
58 % Compute integral approximates (ie sum along t dimension)
59 phaseTF = sum(part1.*part2P,4)./part0; clear part2P
60 absorptionTF = sum(part1.*part2A,4)./part0; clear part2A part1
61
62 % Set TF(mu=0) to 0
63 phaseTF(floor(end/2)+1,floor(end/2)+1,:) = 0;
64 absorptionTF(floor(end/2)+1,floor(end/2)+1,:) = 0;
65
66 % Set any NaNs to 0
67 phaseTF(isnan(phaseTF)) = 0;
68 absorptionTF(isnan(absorptionTF)) = 0;

```

**Listing B.4:** Makes list of spatial frequencies where to compute the OTF, `set_spatial_freq_range.m`

```

1 function [mu_x,mu_y,eta] = set_spatial_freq_range(p)
2 % Computes a set of spatial frequencies at which to calculate OTF
3
4 % Compute a list of lateral indices
5 nyquistLateral = 1/(2*p.pixelSize);
6 fullLateralIndex = linspace(-nyquistLateral,nyquistLateral,p.arrayLength+1);
7 fullLongitudinalIndex = linspace(-nyquistLateral,nyquistLateral,p.arrayLength*p.
    longitudinalUpsampling+1);
8 fullLateralIndex = fullLateralIndex(1:end-1);
9 fullLongitudinalIndex = fullLongitudinalIndex(1:end-1);
10 dmU = fullLateralIndex(2)-fullLateralIndex(1);
11
12 % Find indices only in support region for OTF, skip computing outside
13 % support range
14 maxLateralSpatialFreq = (p.illuminationNA+p.imagingNA)/p.lightWavelength;
15 lateralIndex = fullLateralIndex(abs(fullLateralIndex) <= (maxLateralSpatialFreq+dmU))
    ;
16 maxLongitudinalSpatialFreq = (1/p.lightWavelength)*(1-cos(asin(p.imagingNA)));
17 longitudinalIndex = fullLongitudinalIndex(abs(fullLongitudinalIndex) <= (
    maxLongitudinalSpatialFreq+dmU/p.longitudinalUpsampling));
18
19 % Assuming no symmetries
20 mu_x = lateralIndex;
21 mu_y = mu_x;

```

```
22 eta = longitudinalIndex;
```

**Listing B.5:** Makes coherent (amplitude) spread functions, `make_imaging_illumination_csfs.m`

```
1 function [H,Hi] = make_imaging_illumination_csfs(p)
2 % Creates anonymous functions for imaging and illumination coherent spread
3 % functions (CSFs)
4
5 % Convert parameters to requested data type
6 if strcmp(p.dataType,'single')
7     p.lightWavelength = single(p.lightWavelength);
8     p.imagingNA = single(p.imagingNA);
9     p.illuminationNA = single(p.illuminationNA);
10 end
11
12 % Make illumination NA < or = to imaging NA (validity check)
13 if p.illuminationNA > p.imagingNA
14     p.illuminationNA = p.imagingNA;
15 end
16
17 % Compute frequency cutoffs
18 imagingSpatialFrequencyCutoff = p.imagingNA/p.lightWavelength;
19 imagingSquared = imagingSpatialFrequencyCutoff^2;
20 illuminationSpatialFrequencyCutoff = p.illuminationNA/p.lightWavelength;
21 illumSquared = illuminationSpatialFrequencyCutoff^2;
22
23 % Many anon functions depending on data type
24 if strcmp(p.dataType,'single')
25     H = @(kx,ky) single(kx.^2 + ky.^2 <= imagingSquared);
26
27     if p.asymmetricIllumination
28         Hi = @(kx,ky) single((kx.^2 + ky.^2 <= illumSquared) & kx>=0);
29     else
30         Hi = @(kx,ky) single((kx.^2 + ky.^2 <= illumSquared));
31     end
32 else
33     H = @(kx,ky) double(kx.^2 + ky.^2 <= imagingSquared);
34
35     if p.asymmetricIllumination
36         Hi = @(kx,ky) double((kx.^2 + ky.^2 <= illumSquared) & kx>=0);
37     else
38         Hi = @(kx,ky) double((kx.^2 + ky.^2 <= illumSquared));
39     end
40 end
```

**Listing B.6:** Pad 3D OTFs with zeros to make them the appropriate size, `pad_TFs.m`

```
1 function [ptf,atf] = pad_TFs(ptfIn,atfIn,p)
2 %% PAD_TFS: pads 3D transfer functions to appropriate size
3
```

```

4 % dim 1
5 currentSize = size(ptfIn,1);
6 padAmount = p.arrayLength - currentSize;
7 ptf = padarray(ptfIn,[ceil(padAmount/2) 0 0], 'pre');
8 ptf = padarray(ptf,[floor(padAmount/2) 0 0], 'post');
9 atf = padarray(atfIn,[ceil(padAmount/2) 0 0], 'pre');
10 atf = padarray(atf,[floor(padAmount/2) 0 0], 'post');
11
12 % dim 2
13 currentSize = size(ptfIn,2);
14 padAmount = p.arrayLength - currentSize;
15 ptf = padarray(ptf,[0 ceil(padAmount/2) 0], 'pre');
16 ptf = padarray(ptf,[0 floor(padAmount/2) 0], 'post');
17 atf = padarray(atf,[0 ceil(padAmount/2) 0], 'pre');
18 atf = padarray(atf,[0 floor(padAmount/2) 0], 'post');
19
20 % dim 3
21 currentSize = size(ptfIn,3);
22 padAmount = p.arrayLength - currentSize;
23 ptf = padarray(ptf,[0 0 ceil(padAmount/2)], 'pre');
24 ptf = padarray(ptf,[0 0 floor(padAmount/2)], 'post');
25 atf = padarray(atf,[0 0 ceil(padAmount/2)], 'pre');
26 atf = padarray(atf,[0 0 floor(padAmount/2)], 'post');

```

Listing B.7: Makes synthetic object, `make_3d_object.m`

```

1 function object = make_3d_object(p)
2
3 % Initialize a 3D array for the object to fill
4 arraySize = p.objectSize/p.pixelSize;
5 object = zeros(arraySize,arraySize,arraySize,'single');
6
7 % Check which type of object
8 switch p.objectType
9
10     case 'point' % delta function
11         midPoint = arraySize/2+1;
12         object(midPoint,midPoint,midPoint) = p.deltaN;
13
14     case 'sphere'
15         % Make 3d indices
16         dimIdx = single((-arraySize/2):(arraySize/2-1));
17         [xGr,yGr,zGr] = meshgrid(dimIdx,dimIdx,dimIdx);
18
19         % Add centered sphere to object
20         sphereRadiusInPixels = p.radius/p.pixelSize;
21         sph = p.deltaN*(xGr.^2+yGr.^2+zGr.^2 < sphereRadiusInPixels^2);
22         object = object + sph;
23
24     case 'tube'
25         % Make 2d indices
26         dimIdx = single((-arraySize/2):(arraySize/2-1));
27         [xGr,~,zGr] = meshgrid(dimIdx,1,dimIdx);

```

```

28
29     % Add centered circle to 2D plane
30     circleRadiusInPixels = p.radius/p.pixelSize;
31     circ = p.deltaN*(xGr.^2 + zGr.^2 < circleRadiusInPixels^2);
32     object = object + repmat(circ,[arraySize 1 1]);
33
34     case 'monolayer'
35         % Make 3d indices
36         dimIdx = int16((-arraySize/2):(arraySize/2-1));
37         [xGr,yGr,zGr] = meshgrid(dimIdx,dimIdx,dimIdx);
38         sphereRadiusInPixels = p.radius/p.pixelSize;
39
40         % Determine sphere centers in hex lattice
41         spacingInPixels = p.sphereCenterSpacing/p.pixelSize;
42         xCenters = int16((-arraySize/2):spacingInPixels:(arraySize/2));
43         yCenters = int16((-arraySize/2):(spacingInPixels*sqrt(3)/2):(arraySize/2));
44
45         % Make prototype sphere
46         sph = uint8(xGr.^2+yGr.^2+zGr.^2 < sphereRadiusInPixels^2);
47
48         % Shift prototype sphere and add to image
49         object = zeros(arraySize,arraySize,arraySize,'uint8');
50         for yIdx = 1:length(yCenters)
51             yCenter = yCenters(yIdx);
52             for xIdx = 1:length(xCenters)
53                 xCenter = xCenters(xIdx) + mod(yIdx,2)*spacingInPixels/2;
54                 zOffset = round(xCenter*tan(p.tiltXY(2)) + yCenter*tan(p.tiltXY(1)));
55                 newSphere = circshift(sph,[yCenter,xCenter,zOffset] + int16(p.
centerRandomOffset*randn(1,3)));
56                 object = object + newSphere;
57             end
58         end
59
60         object = single(object)*p.deltaN;
61
62 end

```

**Listing B.8:** Extracts a few key frames from the 3D image and displays a “through focus” (i.e. axial sweep). Also provides an axial (XZ slice), `thru_focus_axial_slice.m`

```

1 function toShow = thru_focus_axial_slice(filtObj,crop,frameThruFocusStartEnd,
    frameThruFocusdz)
2
3 % Gather selected slices
4 slices = -frameThruFocusStartEnd:frameThruFocusdz:frameThruFocusStartEnd;
5 toShow = [];
6 for sIdx = slices
7     toShow = [toShow, filtObj((floor(end/2)+1-crop):(floor(end/2)+1+crop),(floor(end
    /2)+1-crop):(floor(end/2)+1+crop),floor(end/2)+1 + sIdx)];
8 end
9

```

```

10 % Append axial section
11 toShow = [toShow, squeeze(filtObj(floor(end/2)+1,(floor(end/2)+1-crop):(floor(end/2)
    +1+crop),(floor(end/2)+1-crop):(floor(end/2)+1+crop)))'];
12
13 % Scale
14 toShow = (toShow-min(toShow(:))./(max(toShow(:))-min(toShow(:))));

```

**Listing B.9:** Automatically makes a label for the through focus image,  
label\_maker.m

```

1 function outStr = label_maker(p)
2 % Automatically labels display image
3
4 p1 = ['+/-' num2str(p.thruFocusRange) '\mum'];
5 p2 = ' through focus,';
6 p3 = [' ' num2str(p.thruFocusdz) '\mum increments'];
7 p4 = ' + XZ slice';
8 p5 = [' (' num2str(p.thruFocusImgWidthCrop) ' x ' num2str(p.thruFocusImgWidthCrop) '
    \mum frame size)'];
9
10 outStr = [p1 p2 p3 p4 p5];

```

## References

- Abràmoff, M. D., Garvin, M. K., and Sonka, M. (2010). Retinal imaging and image analysis. *IEEE Reviews in Biomedical Engineering*, 3:169–208.
- Alkabes, M., Mazzolani, F., Ratiglia, R., and Orzalesi, N. (2007). A comparison of HRT II with the Rostock Cornea Module and CONFOSCAN 2 confocal microscopes. *Investigative Ophthalmology & Visual Science*, 48(13):3880.
- Anand-Apte, B. and Hollyfield, J. G. (2010). Developmental anatomy of the retinal and choroidal vasculature. In Dartt, D., Besharse, J., and Dana, R., editors, *Encyclopedia of the Eye*, pages 9–15. Academic Press.
- Anderson, N. M. and Sekelj, P. (1967). Light-absorbing and scattering properties of non-haemolysed blood. *Physics in Medicine & Biology*, 12(2):173–184.
- ANSI (2014). *Z136.1–American National Standard for Safe Use of Lasers*. Laser Institute of America, Orlando, FL.
- Artal, P. (2014). Optics of the eye and its impact in vision: a tutorial. *Advances in Optics and Photonics*, 6(3):340–367.
- Atchison, D. and Smith, G. (2000). *Optics of the Human Eye*. Butterworth-Heinemann.
- Beach, J. M., Schwenzer, K. J., Srinivas, S., Kim, D., and Tiedeman, J. S. (1999). Oximetry of retinal vessels by dual-wavelength imaging: calibration and influence of pigmentation. *Journal of Applied Physiology*, 86(2):748–758.
- Berendschot, T. T., DeLint, P. J., and van Norren, D. (2003). Fundus reflectance—historical and present ideas. *Progress in Retinal and Eye Research*, 22(2):171–200.
- Bizheva, K., Tan, B., MacLellan, B., Kralj, O., Hajialamdari, M., Hileeto, D., and Sorbara, L. (2017). Sub-micrometer axial resolution OCT for in-vivo imaging of the cellular structure of healthy and keratoconic human corneas. *Biomedical Optics Express*, 8(2):800–812.
- Boas, D. A., Brooks, D. H., Miller, E. L., Dimarzio, C. A., Kilmer, M., Gaudette, R. J., and Zhang, Q. (2001). Imaging the body with diffuse optical tomography. *IEEE Signal Processing Magazine*, 18(6):57–75.



- Bohn, S., Sperlich, K., Allgeier, S., Bartschat, A., Prakasam, R., Reichert, K.-M., Stolz, H., Guthoff, R., Mikut, R., Köhler, B., and Stachs, O. (2018). Cellular in vivo 3D imaging of the cornea by confocal laser scanning microscopy. *Biomedical Optics Express*, 9(6):2511–2525.
- Bohn, S., Sperlich, K., Stolz, H., Guthoff, R. F., and Stachs, O. (2019). In vivo corneal confocal microscopy aided by optical coherence tomography. *Biomedical Optics Express*, 10(5):2580–2587.
- Bourne, W. M. (2003). Biology of the corneal endothelium in health and disease. *Eye*, 17(8):912–918.
- Bourne, W. M. and Kaufman, H. E. (1976). Specular microscopy of human corneal endothelium in vivo. *American Journal of Ophthalmology*, 81(3):319–323.
- Brown, N. (1971). Visibility of transparent objects in the eye by retroillumination. *British Journal of Ophthalmology*, 55(8):517–524.
- Buttery, R. G., Hinrichsen, C. F., Weller, W. L., and Haight, J. R. (1991). How thick should a retina be? A comparative study of mammalian species with and without intraretinal vasculature. *Vision research*, 31(2):169–187.
- Canavesi, C., Cogliati, A., Mietus, A., Qi, Y., Schallek, J., Rolland, J. P., and Hindman, H. B. (2020). In vivo imaging of corneal nerves and cellular structures in mice with Gabor-domain optical coherence microscopy. *Biomedical Optics Express*, 11(2):711–724.
- Cavanagh, H. D., Jester, J. V., Essepian, J., Shields, W., and Lemp, M. A. (1990). Confocal microscopy of the living eye. *The CLAO Journal*, 16(1):65–73.
- Chen, S., Liu, X., Wang, N., Wang, X., Xiong, Q., Bo, E., Yu, X., Chen, S., and Liu, L. (2017a). Visualizing micro-anatomical structures of the posterior cornea with micro-optical coherence tomography. *Scientific Reports*, 7:10752.
- Chen, S., Shu, X., Nesper, P. L., Liu, W., Fawzi, A. A., and Zhang, H. F. (2017b). Retinal oximetry in humans using visible-light optical coherence tomography [Invited]. *Biomedical Optics Express*, 8(3):1415–1429.
- Choi, S.-Y., Borghuis, B., Rea, R., Levitan, E. S., Sterling, P., and Kramer, R. H. (2005). Encoding light intensity by the cone photoreceptor synapse. *Neuron*, 48(4):555–562.
- Chui, T. Y. P., VanNasdale, D. A., and Burns, S. A. (2012). The use of forward scatter to improve retinal vascular imaging with an adaptive optics scanning laser ophthalmoscope. *Biomedical Optics Express*, 3(10):2537–2549.

- Cioffi, G. A., Granstam, E., and Alm, A. (1987). Ocular circulation. In Hart, W. M., editor, *Adler's Physiology of the Eye: Clinical Application*, pages 747–787. Mosby, 8 edition.
- Cruzat, A., Pavan-Langston, D., and Hamrah, P. (2010). In vivo confocal microscopy of corneal nerves: Analysis and clinical correlation. *Seminars in Ophthalmology*, 25(5-6):171–177.
- Dawson, D. G., Ubels, J. L., and Edelhauser, H. F. (2011). Cornea and sclera. In Kaufman, P. L. and Alm, A., editors, *Adler's Physiology of the Eye*, chapter 4, pages 71–130. Saunders, 11 edition.
- de Carlo, T. E., Romano, A., Waheed, N. K., and Duker, J. S. (2015). A review of optical coherence tomography angiography (OCTA). *International Journal of Retina and Vitreous*, 1:5.
- de Kock, J. P., Tarassenko, L., Glynn, C. J., and Hill, A. R. (1993). Reflectance pulse oximetry measurements from the retinal fundus. *IEEE Transactions on Biomedical Engineering*, 40(8):817–823.
- Delori, F. C. (1988). Noninvasive technique for oximetry of blood in retinal vessels. *Applied Optics*, 27(6):1113–1125.
- Delori, F. C., Gragoudas, E. S., Francisco, R., and Pruett, R. C. (1977). Monochromatic ophthalmoscopy and fundus photography: The normal fundus. *Archives of Ophthalmology*, 95(5):861–868.
- Delori, F. C. and Pflibsen, K. P. (1989). Spectral reflectance of the human ocular fundus. *Applied Optics*, 28(6):1061–1077.
- Delori, F. C., Webb, R. H., and Sliney, D. H. (2007). Maximum permissible exposures for ocular safety (ANSI 2000), with emphasis on ophthalmic devices. *Journal of the Optical Society of America A*, 24(5):1250.
- DePaoli, D. T., Tossou, P., Parent, M., Sauvageau, D., and Côté, D. C. (2019). Convolutional neural networks for spectroscopic analysis in retinal oximetry. *Scientific Reports*, 9(1):11387.
- Elsner, A. E., Burns, S. A., Weiter, J. J., and Delori, F. C. (1996). Infrared imaging of sub-retinal structures in the human ocular fundus. *Vision Research*, 36(1):191–205.
- Erie, J. C., McLaren, J. W., Hodge, D. O., and Bourne, W. M. (2005). The effect of age on the corneal subbasal nerve plexus. *Cornea*, 24(6):705–709.
- Fercher, A. F. (1996). Optical coherence tomography. *Journal of Biomedical Optics*, 1(2):157–173.

- Ford, T. N., Chu, K. K., and Mertz, J. (2012). Phase-gradient microscopy in thick tissue with oblique back-illumination. *Nature Methods*, 9(12):1195–1197.
- Ford, T. N. and Mertz, J. (2013). Video-rate imaging of microcirculation with single-exposure oblique back-illumination microscopy. *Journal of Biomedical Optics*, 18(6):066007.
- Geeraets, W. J., Williams, R. C., Chan, G., Ham, W. T., Guerry, D., and Schmidt, F. H. (1960). The loss of light energy in retina and choroid. *Archives of Ophthalmology*, 64(4):606–615.
- Goldstein, L. E., Muffat, J. A., Cherny, R. A., Moir, R. D., Ericsson, M. H., Huang, X., Mavros, C., Coccia, J. A., Faget, K. Y., Fitch, K. A., Masters, C. L., Tanzi, R. E., Chylack, L. T., and Bush, A. I. (2003). Cytosolic  $\beta$ -amyloid deposition and supranuclear cataracts in lenses from people with Alzheimer’s disease. *The Lancet*, 361(9365):1258–1265.
- Guevara-Torres, A., Williams, D. R., and Schallek, J. B. (2015). Imaging translucent cell bodies in the living mouse retina without contrast agents. *Biomedical Optics Express*, 6(6):2106–2119.
- Guevara-Torres, A., Williams, D. R., and Schallek, J. B. (2020). Origin of cell contrast in offset aperture adaptive optics ophthalmoscopy. *Optics Letters*, 45(4):840–843.
- Guizar-Sicairos, M., Thurman, S. T., and Fienup, J. R. (2008). Efficient subpixel image registration algorithms. *Optics Letters*, 33(2):156.
- Guthoff, R. F., Baudouin, C., and Stave, J. (2006). *Atlas of Confocal Laser Scanning In-vivo Microscopy in Ophthalmology*. Springer-Verlag Berlin Heidelberg.
- Guthoff, R. F., Wiens, H., Hahnel, C., and Wree, A. (2005). Epithelial innervation of human cornea: a three-dimensional study using confocal laser scanning fluorescence microscopy. *Cornea*, 24(5):608–613.
- Guthoff, R. F., Zhivov, A., and Stachs, O. (2009). In vivo confocal microscopy, an inner vision of the cornea – a major review. *Clinical & Experimental Ophthalmology*, 37(1):100–117.
- Hamilton, D. and Sheppard, C. (1984). Differential phase contrast in scanning optical microscopy. *Journal of Microscopy*, 133(1):27–39.
- Hammer, M., Schweitzer, D., Michel, B., Thamm, E., and Kolb, A. (1998). Single scattering by red blood cells. *Applied Optics*, 37(31):7410–7418.

- Hammer, M., Schweitzer, D., Thamm, E., Kolb, A., and Strobel, J. (2001). Scattering properties of the retina and the choroids determined from OCT-A-scans. *International Ophthalmology*, 23:291–295.
- Hammer, M., Vilser, W., Riemer, T., and Schweitzer, D. (2008). Retinal vessel oximetry-calibration, compensation for vessel diameter and fundus pigmentation, and reproducibility. *Journal of Biomedical Optics*, 13(5):054015.
- Han, L., Hosseiaee, Z., Tan, B., and Bizheva, K. (2019). High resolution line-field SD-OCT with 2.5 kHz frame rate for cellular resolution imaging of biological tissue. In Fujimoto, J. G. and Izatt, J. A., editors, *Optical Coherence Tomography and Coherence Domain Optical Methods in Biomedicine XXIII*, volume 10867, pages 123–128. International Society for Optics and Photonics, SPIE.
- Hardarson, S. H., Basit, S., Jonsdottir, T. E., Eysteinnsson, T., Halldorsson, G. H., Karlsson, R. A., Beach, J. M., Benediktsson, J. A., and Stefansson, E. (2009). Oxygen saturation in human retinal vessels is higher in dark than in light. *Investigative Ophthalmology & Visual Science*, 50(5):2308–2311.
- Hardarson, S. H., Harris, A., Karlsson, R. A., Halldorsson, G. H., Kagemann, L., Rechtman, E., Zoega, G. M., Eysteinnsson, T., Benediktsson, J. A., Thorsteinsson, A., Jensen, P. K., Beach, J., and Stefansson, E. (2006). Automatic retinal oximetry. *Investigative Ophthalmology & Visual Science*, 47(11):5011–5016.
- Harris, A., Dinn, R. B., Kagemann, L., and Rechtman, E. (2003). A review of methods for human retinal oximetry. *Ophthalmic Surgery, Lasers and Imaging*, 34(2):152–164.
- Hecht, E. (2001). *Optics*, chapter 5, pages 191–195. Addison-Wesley, 4 edition.
- Hertz, P., Bril, V., Orszag, A., Ahmed, A., Ng, E., Nwe, P., Ngo, M., and Perkins, B. (2011). Reproducibility of in vivo corneal confocal microscopy as a novel screening test for early diabetic sensorimotor polyneuropathy. *Diabetic Medicine*, 28(10):1253–1260.
- Hickam, J. B., Frayser, R., and Ross, J. C. (1963). A study of retinal venous blood oxygen saturation in human subjects by photographic means. *Circulation*, 27(3):375–385.
- Hodgkinson, I. J., Greer, P. B., and Molteno, A. C. B. (1994). Point-spread function for light scattered in the human ocular fundus. *Journal of the Optical Society of America A*, 11(2):479–486.
- Huang, D., Swanson, E. A., Lin, C. P., Schuman, J. S., Stinson, W. G., Chang, W., Hee, M. R., Flotte, T., Gregory, K., Puliafito, C. A., and Fujimoto, J. G. (1991). Optical coherence tomography. *Science*, 254(5035):1178–1181.

- Jacques, S. L. (1998). Melanosome absorption coefficient. <https://omlc.org/spectra/melanin/mua.html>. Accessed: 4 May 2018.
- Jacques, S. L. (2013). Optical properties of biological tissues: a review. *Physics in Medicine and Biology*, 58(11):R37–R61.
- Jacques, S. L. and Pogue, B. W. (2008). Tutorial on diffuse light transport. *Journal of Biomedical Optics*, 13(4):041302.
- Jain, S., Hamada, S., Membrey, W. L., and Chong, V. (2006). Screening for age-related macular degeneration using nonstereo digital fundus photographs. *Eye*, 20(4):471–475.
- Jeppesen, S. K. and Bek, T. (2019). The retinal oxygen saturation measured by dual wavelength oximetry in larger retinal vessels is influenced by the linear velocity of the blood. *Current Eye Research*, 44(1):46–52.
- Kachar, B. (1985). Asymmetric illumination contrast: a method of image formation for video light microscopy. *Science*, 227(4688):766–768.
- Kashani, A. H., Chen, C.-L., Gahm, J. K., Zheng, F., Richter, G. M., Rosenfeld, P. J., Shi, Y., and Wang, R. K. (2017). Optical coherence tomography angiography: A comprehensive review of current methods and clinical applications. *Progress in Retinal and Eye Research*, 60:66–100.
- Koch, K., McLean, J., Segev, R., Freed, M. A., Berry II, M. J., Balasubramanian, V., and Sterling, P. (2006). How much the eye tells the brain. *Current Biology*, 16(14):1428–1434.
- Koester, C. J. (1980). Scanning mirror microscope with optical sectioning characteristics: applications in ophthalmology. *Applied Optics*, 19(11):1749–1757.
- Konan Medical (2020). Cellchek specular microscope. <https://konanmedical.com/cellchek/>. Accessed: 17 March 2020.
- Kruse, F. E. (1994). Stem cells and corneal epithelial regeneration. *Eye*, 8(2):170–183.
- Laing, R. A., Sandstrom, M. M., and Leibowitz, H. M. (1975). In vivo photomicrography of the corneal endothelium. *Archives of Ophthalmology*, 93(2):143–145.
- Laing, R. A., Sandstrom, M. M., and Leibowitz, H. M. (1979a). Clinical specular microscopy I. Optical principles. *Archives of Ophthalmology*, 97(9):1714–1719.
- Laing, R. A., Sandstrom, M. M., and Leibowitz, H. M. (1979b). Clinical specular microscopy II. Qualitative evaluation of corneal endothelial photomicrographs. *Archives of Ophthalmology*, 97(9):1720–1725.

- Leung, I. Y. and Snodderly, D. M. (2001). Vertical section of the foveal region in rhesus monkey. <http://www.sbs.utexas.edu/SnodderlyLab/gallery.html>. Accessed: 8 October 2017.
- Levin, L. A. and Albert, D. M. (2010). *Ocular Disease: Mechanisms and Management*. Saunders.
- Li, H. K. (1999). Telemedicine and ophthalmology. *Survey of Ophthalmology*, 44(1):61 – 72.
- Liang, J., Williams, D. R., and Miller, D. T. (1997). Supernormal vision and high-resolution retinal imaging through adaptive optics. *Journal of the Optical Society of America A*, 14(11):2884–2892.
- Lim, J. K. H., Li, Q. X., He, Z., Vingrys, A. J., Wong, V. H. Y., Currier, N., Mullen, J., Bui, B. V., and Nguyen, C. T. O. (2016). The eye as a biomarker for Alzheimer’s disease. *Frontiers in Neuroscience*, 10:536.
- Linsenmeier, R. A. and Padnick-Silver, L. (2000). Metabolic dependence of photoreceptors on the choroid in the normal and detached retina. *Investigative Ophthalmology & Visual Science*, 41(10):3117–3123.
- Linsenmeier, R. A. and Zhang, H. F. (2017). Retinal oxygen: from animals to humans. *Progress in Retinal and Eye Research*, 58:115–151.
- MacKenzie, L. E. and Harvey, A. R. (2018). Oximetry using multispectral imaging: theory and application. *Journal of Optics*, 20(6):063501.
- Marfurt, C. F., Cox, J., Deek, S., and Dvorscak, L. (2010). Anatomy of the human corneal innervation. *Experimental Eye Research*, 90(4):478–492.
- Masters, B. R. (1992). Confocal microscopy of the in-situ crystalline lens. *Journal of Microscopy*, 165(1):159–167.
- Masters, B. R. and Paddock, S. (1990a). In vitro confocal imaging of the rabbit cornea. *Journal of Microscopy*, 158(2):267–274.
- Masters, B. R. and Paddock, S. W. (1990b). Three-dimensional reconstruction of the rabbit cornea by confocal scanning optical microscopy and volume rendering. *Applied Optics*, 29(26):3816–3822.
- Masters, B. R. and Thaer, A. A. (1994). Real-time scanning slit confocal microscopy of the in vivo human cornea. *Applied Optics*, 33(4):695–701.
- Maurice, D. (1968). Cellular membrane activity in the corneal endothelium of the intact eye. *Experientia*, 24(11):1094–1095.

- Maurice, D. M. (1974). A scanning slit optical microscope. *Investigative Ophthalmology*, 13(12):1033–1037.
- Mazlin, V., Xiao, P., Dalimier, E., Grieve, K., Irsch, K., Sahel, J.-A., Fink, M., and Boccara, A. C. (2018). In vivo high resolution human corneal imaging using full-field optical coherence tomography. *Biomedical Optics Express*, 9(2):557–568.
- Mazlin, V., Xiao, P., Scholler, J., Irsch, K., Grieve, K., Fink, M., and Boccara, A. C. (2020). Real-time, non-contact, cellular imaging and angiography of human cornea and limbus with common-path full-field/SDOCT. *Nature Communications*.
- McCarey, B. E., Edelhauser, H. F., and Lynn, M. J. (2008). Review of corneal endothelial specular microscopy for FDA clinical trials of refractive procedures, surgical devices, and new intraocular drugs and solutions. *Cornea*, 27(1):1–16.
- Mehta, S. B. and Sheppard, C. J. R. (2009). Quantitative phase-gradient imaging at high resolution with asymmetric illumination-based differential phase contrast. *Optics Letters*, 34(13):1924–1926.
- Meijering, E., Jacob, M., Sarria, J.-C., Steiner, P., Hirling, H., and Unser, M. (2004). Design and validation of a tool for neurite tracing and analysis in fluorescence microscopy images. *Cytometry Part A*, 58(2):167–176.
- Mertz, J. (2019). *Introduction to Optical Microscopy*. Cambridge University Press, 2 edition.
- Mertz, J., Gasecka, A., Daradich, A., Davison, I., and Coté, D. (2014). Phase-gradient contrast in thick tissue with a scanning microscope. *Biomedical Optics Express*, 5(2):407–416.
- Miller, K. M., Albert, D. L., Asbell, P. A., Atebara, N. H., Schechter, R. J., Wang, M. X., and Morse, C. (2005). *Basic and Clinical Science Course, Section 03: Clinical Optics*, chapter 9, page 296. American Academy of Ophthalmology. after Neal H. Atebara, MD. Redrawn by Cyndie C. H. Wooley.
- Misra, S., Craig, J., Patel, D., McGhee, C., Pradhan, M., Ellyett, K., Kilfoyle, D., and Braatvedt, G. (2015). In vivo confocal microscopy of corneal nerves: An ocular biomarker for peripheral and cardiac autonomic neuropathy in type 1 diabetes mellitus. *Investigative Ophthalmology & Visual Science*, 56(9):5060–5065.
- Mordant, D. J., Al-Abboud, I., Muyo, G., Gorman, A., Sallam, A., Ritchie, P., Harvey, A. R., and McNaught, A. I. (2011). Spectral imaging of the retina. *Eye*, 25(3):309–320.

- Narasimha-Iyer, H., Mahadevan, V., Beach, J. M., and Roysam, B. (2008). Improved detection of the central reflex in retinal vessels using a generalized dual-gaussian model and robust hypothesis testing. *IEEE Transactions on Information Technology in Biomedicine*, 12(3):406–410.
- Niederer, R. L., Perumal, D., Sherwin, T., and McGhee, C. N. (2007a). Age-related differences in the normal human cornea: a laser scanning in vivo confocal microscopy study. *British Journal of Ophthalmology*, 91(9):1165–1169.
- Niederer, R. L., Perumal, D., Sherwin, T., and McGhee, C. N. (2007b). Corneal innervation and cellular changes after corneal transplantation: an in vivo confocal microscopy study. *Investigative ophthalmology & visual science*, 48(2):621–626.
- Niederer, R. L., Perumal, D., Sherwin, T., and McGhee, C. N. (2008). Laser scanning in vivo confocal microscopy reveals reduced innervation and reduction in cell density in all layers of the keratoconic cornea. *Investigative ophthalmology & visual science*, 49(7):2964–2970.
- Nitoda, E., Kallinikos, P., Pallikaris, A., Moschandrea, J., Amoiridis, G., Ganotakis, E., and Tsilimbaris, M. (2012). Correlation of diabetic retinopathy and corneal neuropathy using confocal microscopy. *Current eye research*, 37(10):898–906.
- Novotny, H. R. and Alvis, D. L. (1961). A method of photographing fluorescence in circulating blood in the human retina. *Circulation*, 24(1):82–86.
- Olafsdottir, O. B., Saevarsdottir, H. S., Hardarson, S. H., Hannesdottir, K. H., Traustadottir, V. D., Karlsson, R. A., Einarsdottir, A. B., Jonsdottir, K. D., Stefánsson, E., and Snaedal, J. (2018). Retinal oxygen metabolism in patients with mild cognitive impairment. *Alzheimer's & Dementia: Diagnosis, Assessment & Disease Monitoring*, 10:340–345.
- Oliveira-Soto, L. and Efron, N. (2001). Morphology of corneal nerves using confocal microscopy. *Cornea*, 20(4):374–384.
- Osterberg, G. (1935). Topography of the layer of rods and cones in the human retina. *Acta Ophthalmologica*, Supplement 6:1–103.
- Parissi, M., Karanis, G., Randjelovic, S., Germundsson, J., Poletti, E., Ruggeri, A., Utheim, T. P., and Lagali, N. (2013). Standardized baseline human corneal subbasal nerve density for clinical investigations with laser-scanning in vivo confocal microscopy. *Investigative Ophthalmology & Visual Science*, 54(10):7091–7102.
- Pascolini, M., Minozzi, M., Carraro, F., Codogno, N., Pajaro, R., Tiso, C., Pajaro, S., and Tanassi, C. (2020). Non-contact laser confocal microscope for corneal imaging. *Investigative Ophthalmology & Visual Science*, 60(9):2123.



- Patel, D., Ku, J., Johnson, R., and McGhee, C. (2009). Laser scanning in vivo confocal microscopy and quantitative aesthesiometry reveal decreased corneal innervation and sensation in keratoconus. *Eye*, 23(3):586–592.
- Patel, D. V. and McGhee, C. N. (2005). Mapping of the normal human corneal sub-basal nerve plexus by in vivo laser scanning confocal microscopy. *Investigative Ophthalmology & Visual Science*, 46(12):4485–4488.
- Patel, D. V. and McGhee, C. N. J. (2009). In vivo confocal microscopy of human corneal nerves in health, in ocular and systemic disease, and following corneal surgery: a review. *British Journal of Ophthalmology*, 93(7):853–860.
- Paudel, H. P., Alt, C., Runnels, J., and Lin, C. P. (2018). Pupil plane differential detection microscopy. *Optics Letters*, 43(18):4410–4412.
- Petráň, M., Hadravský, M., Egger, M. D., and Galambos, R. (1968). Tandem-scanning reflected-light microscope. *Journal of the Optical Society of America*, 58(5):661–664.
- Poplin, R., Varadarajan, A. V., Blumer, K., Liu, Y., McConnell, M. V., Corrado, G. S., Peng, L., and Webster, D. R. (2018). Prediction of cardiovascular risk factors from retinal fundus photographs via deep learning. *Nature Biomedical Engineering*, 2(3):158–164.
- Pournaras, C. J., Rungger-Brändle, E., Riva, C. E., Hardarson, S. H., and Stefansson, E. (2008). Regulation of retinal blood flow in health and disease. *Progress in Retinal and Eye Research*, 27(3):284–330.
- Prahl, S. (1999). Optical absorption of hemoglobin. <https://omlc.org/spectra/hemoglobin/>. Accessed: 30 April 2018.
- Pritchard, N., Edwards, K., and Efron, N. (2014). Non-contact laser-scanning confocal microscopy of the human cornea in vivo. *Contact Lens and Anterior Eye*, 37(1):44–48.
- Pritchard, N., Edwards, K., Shahidi, A. M., Sampson, G. P., Russell, A. W., Malik, R. A., and Efron, N. (2011). Corneal markers of diabetic neuropathy. *The Ocular Surface*, 9(1):17 – 28.
- Reddy, S. B. and Chatterji, B. N. (1996). An FFT-based technique for translation, rotation, and scale-invariant image registration. *IEEE Transactions on Image Processing*, 5(8):1266–1271.
- Roberts, D. A. (1987). Analysis of vessel absorption profiles in retinal oximetry. *Medical Physics*, 14(1):124–130.

- Rolland, J. P., Meemon, P., Murali, S., Thompson, K. P., and Lee, K. (2010). Gabor-based fusion technique for optical coherence microscopy. *Optics Express*, 18(4):3632–3642.
- Roorda, A., Romero-Borja, F., Donnelly, III, W. J., Queener, H., Hebert, T. J., and Campbell, M. C. W. (2002). Adaptive optics scanning laser ophthalmoscopy. *Optics Express*, 10(9):405–412.
- Rossi, E. A., Granger, C. E., Sharma, R., Yang, Q., Saito, K., Schwarz, C., Walters, S., Nozato, K., Zhang, J., Kawakami, T., Fischer, W., Latchney, L. R., Hunter, J. J., Chung, M. M., and Williams, D. R. (2017). Imaging individual neurons in the retinal ganglion cell layer of the living eye. *Proceedings of the National Academy of Sciences*, 114(3):586–591.
- Saari, J. C. (1987). Metabolism and photochemistry in the retina. In Hart, W. M., editor, *Adler’s Physiology of the Eye: Clinical Application*, pages 356–373. Mosby, 8 edition.
- Salyer, D. A., Beaudry, N., Basavanthappa, S., Twietmeyer, K., Eskandari, M., Denninghoff, K. R., Chipman, R. A., and Park, R. I. (2006). Retinal oximetry using intravitreal illumination. *Current Eye Research*, 31(7-8):617–627.
- Scarcelli, G., Pineda, R., and Yun, S. H. (2012). Brillouin optical microscopy for corneal biomechanics. *Investigative Ophthalmology & Visual Science*, 53(1):185–190.
- Schneider, C. A., Rasband, W. S., and Eliceiri, K. W. (2012). NIH Image to ImageJ: 25 years of image analysis. *Nature Methods*, 9(7):671–675.
- Schweitzer, D., Hammer, M., Kraft, J., Thamm, E., Königsdörffer, E., and Strobel, J. (1999). In vivo measurement of the oxygen saturation of retinal vessels in healthy volunteers. *IEEE Transactions on Biomedical Engineering*, 46(12):1454–1465.
- Schwiegerling, J. (2004). *Field guide to visual and ophthalmic optics*. SPIE Publications.
- Scoles, D., Sulai, Y. N., Langlo, C. S., Fishman, G. A., Curcio, C. A., Carroll, J., and Dubra, A. (2014). In vivo imaging of human cone photoreceptor inner segments. *Investigative Ophthalmology & Visual Science*, 55(7):4244–4251.
- Sentenac, A. and Mertz, J. (2018). Unified description of three-dimensional optical diffraction microscopy: from transmission microscopy to optical coherence tomography: tutorial. *Journal of the Optical Society of America A*, 35(5):748–754.
- Sheppard, C. J. (2002). Three-dimensional phase imaging with the intensity transport equation. *Applied optics*, 41(28):5951–5955.

- Sheppard, C. J. (2004). Defocused transfer function for a partially coherent microscope and application to phase retrieval. *Journal of the Optical Society of America A*, 21(5):828–831.
- Shu, X., Beckmann, L. J., and Zhang, H. F. (2017). Visible-light optical coherence tomography: a review. *Journal of Biomedical Optics*, 22(12):121707.
- Smith, M. H., Denninghoff, K. R., Lompado, A., and Hillman, L. W. (2000). Effect of multiple light paths on retinal vessel oximetry. *Applied Optics*, 39(7):1183–1193.
- Smith, M. H., Denninghoff, K. R., Lompado, A., Woodruff, J. B., and Hillman, L. W. (2001). Minimizing the influence of fundus pigmentation on retinal vessel oximetry measurements. In Manns, F., Soederberg, P. G., and Ho, A., editors, *Ophthalmic Technologies XI*, volume 4245, pages 135 – 145. International Society for Optics and Photonics, SPIE.
- Snodderly, D. M., Brown, P. K., Delori, F. C., and Auran, J. D. (1984). The macular pigment. I. Absorbance spectra, localization, and discrimination from other yellow pigments in primate retinas. *Investigative Ophthalmology & Visual Science*, 25(6):660–673.
- Spaide, R. F., Koizumi, H., and Pozonni, M. C. (2008). Enhanced depth imaging spectral-domain optical coherence tomography. *American Journal of Ophthalmology*, 146(4):496–500.
- Stachs, O., Guthoff, R. F., and Aumann, S. (2019). In vivo confocal scanning laser microscopy. In Bille, J. F., editor, *High Resolution Imaging in Microscopy and Ophthalmology: New Frontiers in Biomedical Optics*, chapter 12, pages 263–284. Springer.
- Stachs, O., Sperlich, K., Bohn, S., Stolz, H., and Guthoff, R. (2017). Rostock Cornea Module 2.0 – a versatile extension for anterior segment imaging. *Acta Ophthalmologica*, 95:2381.
- Stave, J. and Guthoff, R. (1998). Erste untersuchungsergebnisse mit einem modifiziertem konfokalen laser-scanning-ophthalmoskop. *Der Ophthalmologe*, 95(4):104–109.
- Stave, J., Zinser, G., Grümmer, G., and Guthoff, R. (2002). Der modifizierte Heidelberg-Retina-Tomograph HRT erste ergebnisse einer in-vivo-darstellung von kornealen strukturen. *Der Ophthalmologe*, 99(4):276–280.
- Strangman, G., Boas, D. A., and Sutton, J. P. (2002). Non-invasive neuroimaging using near-infrared light. *Biological Psychiatry*, 52(7):679–693.

- Streibl, N. (1984). Fundamental restrictions for 3-D light distributions. *Optik*, 66(4):341–354.
- Streibl, N. (1985). Three-dimensional imaging by a microscope. *Journal of the Optical Society of America A*, 2(2):121–127.
- Szafflik, J. P. (2007). Comparison of in vivo confocal microscopy of human cornea by white light scanning slit and laser scanning systems. *Cornea*, 26(4):438–445.
- Tan, B., Hosseinaee, Z., Han, L., Kralj, O., Sorbara, L., and Bizheva, K. (2018). 250 kHz, 1.5  $\mu\text{m}$  resolution SD-OCT for in-vivo cellular imaging of the human cornea. *Biomedical Optics Express*, 9(12):6569–6583.
- Tankam, P., He, Z., Thuret, G., Hindman, H. B., Canavesi, C., Escudero, J. C., Lépine, T., Gain, P., and Rolland, J. P. (2019). Capabilities of Gabor-domain optical coherence microscopy for the assessment of corneal disease. *Journal of Biomedical Optics*, 24(4):046002.
- Tavakoli, M., Hossain, P., and Malik, R. A. (2008). Clinical applications of corneal confocal microscopy. *Clinical Ophthalmology*, 2(2):435.
- Teague, M. R. (1983). Deterministic phase retrieval: a Green’s function solution. *Journal of the Optical Society of America*, 73(11):1434–1441.
- Tessier-Lavigne, M. (2000). Visual processing by the retina. In Kandel, E. R., Schwartz, J. H., and Jessell, T. M., editors, *Principles of Neural Science*, pages 507–522. McGraw-Hill, 4 edition.
- Thevenaz, P., Ruttimann, U. E., and Unser, M. (1998). A pyramid approach to subpixel registration based on intensity. *IEEE transactions on image processing*, 7(1):27–41.
- Tian, L. and Waller, L. (2015). Quantitative differential phase contrast imaging in an LED array microscope. *Optics Express*, 23(9):11394–11403.
- Tian, L., Wang, J., and Waller, L. (2014). 3D differential phase-contrast microscopy with computational illumination using an led array. *Optics Letters*, 39(5):1326–1329.
- Ting, D. S. W., Pasquale, L. R., Peng, L., Campbell, J. P., Lee, A. Y., Raman, R., Tan, G. S. W., Schmetterer, L., Keane, P. A., and Wong, T. Y. (2019). Artificial intelligence and deep learning in ophthalmology. *British Journal of Ophthalmology*, 103(2):167–175.

- Toth, C. A., Narayan, D. G., Boppart, S. A., Hee, M. R., Fujimoto, J. G., Birngruber, R., Cain, C. P., DiCarlo, C. D., and Roach, W. P. (1997). A comparison of retinal morphology viewed by optical coherence tomography and by light microscopy. *Archives of Ophthalmology*, 115(11):1425–1428.
- Tuft, S. J. and Coster, D. J. (1990). The corneal endothelium. *Eye*, 4(3):389–424.
- Vaddavalli, P. K., Garg, P., Sharma, S., Sangwan, V. S., Rao, G. N., and Thomas, R. (2011). Role of confocal microscopy in the diagnosis of fungal and acanthamoeba keratitis. *Ophthalmology*, 118(1):29–35.
- van der Putten, M. A., MacKenzie, L. E., Davies, A. L., Fernandez-Ramos, J., Desai, R. A., Smith, K. J., and Harvey, A. R. (2017). A multispectral microscope for in vivo oximetry of rat dorsal spinal cord vasculature. *Physiological Measurement*, 38(2):205–218.
- Van Norren, D. and Tiemeijer, L. F. (1986). Spectral reflectance of the human eye. *Vision Research*, 26(2):313–320.
- Vien, L. (2014). Optical coherent tomography scans. [www.octscans.com](http://www.octscans.com). Accessed: May 2017.
- Villani, E., Galimberti, D., Viola, F., Mapelli, C., Del Papa, N., and Ratiglia, R. (2008). Corneal involvement in rheumatoid arthritis: an in vivo confocal study. *Investigative Ophthalmology & Visual Science*, 49(2):560–564.
- Vogt, A. (1920). Die sichtbarkeit des lebenden hornhautendothels: ein beitrag zur methodik der spaltlampenmikroskopie. *Albrecht von Graefes Archiv für Ophthalmologie*, 101(2):123–144.
- Wagner, S. K., Fu, D. J., Faes, L., Liu, X., Huemer, J., Khalid, H., Ferraz, D., Korot, E., Kelly, C., Balaskas, K., Denniston, A. K., and Keane, P. A. (2020). Insights into systemic disease through retinal imaging-based oculomics. *Translational Vision Science & Technology*, 9(2):6.
- Wang, L. V. and Wu, H. (2007). *Biomedical Optics: Principles and Imaging*. John Wiley & Sons.
- Webb, R. H. and Hughes, G. W. (1981). Scanning laser ophthalmoscope. *IEEE Transactions on Biomedical Engineering*, 28(7):488–492.
- Webb, R. H., Hughes, G. W., and Delori, F. C. (1987). Confocal scanning laser ophthalmoscope. *Applied Optics*, 26(8):1492–1499.
- Webb, R. H., Hughes, G. W., and Pomerantzeff, O. (1980). Flying spot TV ophthalmoscope. *Applied Optics*, 19(17):2991–2997.

- Weber, T. D. and Mertz, J. (2018a). Non-mydriatic chorioretinal imaging in a transmission geometry and application to retinal oximetry. *Biomedical Optics Express*, 9(8):3867–3882.
- Weber, T. D. and Mertz, J. (2018b). Retina and choroid imaging with transcranial back-illumination. In *Biophotonics Congress: Biomedical Optics Congress 2018 (Microscopy/Translational/Brain/OTS)*, page CF3B.8. Optical Society of America.
- Weber, T. D. and Mertz, J. (2019a). Transcranial transmission fundus imaging. *Investigative Ophthalmology & Visual Science*, 60(9):6095.
- Weber, T. D. and Mertz, J. (2019b). Transcranial versus transpupil illumination for fundus imaging. *Investigative Ophthalmology & Visual Science*, 60(11):PB029.
- Weber, T. D. and Mertz, J. (2020). In vivo corneal and lenticular microscopy with asymmetric fundus retroillumination. <https://www.biorxiv.org/content/10.1101/2020.03.10.985341v1>.
- Werkmeister, R. M., Sapeta, S., Schmidl, D., Garhöfer, G., Schmidinger, G., dos Santos, V. A., Aschinger, G. C., Baumgartner, I., Pircher, N., Schwarzlhans, F., Pantalon, A., Dua, H., and Schmetterer, L. (2017). Ultrahigh-resolution OCT imaging of the human cornea. *Biomedical Optics Express*, 8(2):1221–1239.
- Yao, X., Devarajan, K., Werkmeister, R. M., dos Santos, V. A., Ang, M., Kuo, A., Wong, D. W. K., Chua, J., Tan, B., Barathi, V. A., and Schmetterer, L. (2019). In vivo corneal endothelium imaging using ultrahigh resolution OCT. *Biomedical Optics Express*, 10(11):5675–5686.
- Yi, J., Wei, Q., Liu, W., Backman, V., and Zhang, H. F. (2013). Visible-light optical coherence tomography for retinal oximetry. *Optics Letters*, 38(11):1796–1798.

# CURRICULUM VITAE

